ISTANBUL TECHNICAL UNIVERSITY ★ GRADUATE SCHOOL OF SCIENCE ENGINEERING AND TECHNOLOGY

MORPHOTECTONIC ANALYSIS OF THE EAST ANATOLIAN FAULT ZONE (E. TURKEY) USING REMOTE SENSING TECHNIQUES

Ph.D. THESIS

Abdelrahman KHALIFA

Department of Geological Engineering

Geological Engineering Programme

MARCH 2018

ISTANBUL TECHNICAL UNIVERSITY ★ GRADUATE SCHOOL OF SCIENCE ENGINEERING AND TECHNOLOGY

MORPHOTECTONIC ANALYSIS OF THE EAST ANATOLIAN FAULT ZONE (E. TURKEY) USING REMOTE SENSING TECHNIQUES

Ph.D. THESIS

Abdelrahman KHALIFA
(505122305)

Department of Geological Engineering

Geological Engineering Programme

Thesis Advisor: Prof. Dr. Ziyadin ÇAKIR
Thesis Co-Advisor: Prof. Dr. Şinasi KAYA

MARCH 2018

İSTANBUL TEKNİK ÜNİVERSİTESİ ★ FEN BİLİMLERİ ENSTİTÜSÜ

UZAKTAN ALGILAMA TEKNİKLERİ KULLANARAK DOĞU ANADOLU FAY ZONU'NUN (TÜRKİYE'NİN DOĞUSU) MORFOTEKTONİK ANALİZİ

DOKTORA TEZİ

Abdelrahman KHALIFA
(505122305)

Jeoloji Mühendisliği Anabilim Dalı

Jeoloji Mühendisliği Programı

Tez Danışmanı: Prof. Dr. Ziyadin ÇAKIR
Eş Danışman: Doç. Dr. Şinasi KAYA

MART 2018

Abdelrahman KHALIFA, a Ph.D. student of İTU Graduate School of Science Engineering and Technology student ID 505122305, successfully defended the thesis/dissertation entitled "Morphotectonic Analysis of the East Anatolian Fault zone (E. Turkey) using Remote Sensing Techniques", which he/she prepared after fulfilling the requirements specified in the associated legislations, before the jury whose signatures are below.

Thesis Advisor :   **Prof. Dr. Ziyadin ÇAKIR**   ....
Istanbul Technical University

Co-advisor :   **Prof.Dr. Şinasi KAYA**   ....
Istanbul Technical University

Jury Members :   **Prof. Dr. Serdar AKYÜZ**   ....
Istanbul Technical University

Prof. Dr. Semih ERGINTAV   ....
Boğaziçi University

Prof. Dr. Cem GAZİOĞLU   ....
Istanbul University

Associate Prof. Gürsel SUNAL   ....
Istanbul Technical University

Assistant Prof. M. Korhan ERTURAÇ   ....
Sakarya University

Date of Submission : 13 February 2018
Date of Defense   : 13 March 2018

To my mother,

FOREWORD

First and foremost I would like to express my deepest appreciation to my advisors, Ziyadin Çakir and Şinasi Kaya, whose advice and mentorship have been tireless, fair and of top-notch standards. I am totally grateful to my advisor Ziyadin Çakir, who continually and convincingly conveyed a spirit of adventure in regard to research and sharing his great experience and knowledge on Active tectonics during my PhD period. Many thanks to Şinasi Kaya for his guidance and illuminating suggestions in remote sensing parts. Without them, guidance and persistent help this thesis would not have been possible.

Grateful thanks are expressed to hosting advisor, Lewis Owen, head of the Geology Department, University of Cincinnati, USA for his kind hosting in his department for one year and for valuable comments that improved the accepted papers from this thesis.

I am also grateful to my thesis committee, H. Serdar Akyüz, Cem Gazioğlu, and Semih Engintav, who constructive criticism significantly improved this work.

It is my pleasure to convey my sincere appreciation to Cengiz Yıldırım and Cengiz Zabcı for them suggestions and significant discussion to improve this study.

I would like to express my thanks for my colleagues and friends in Egypt, Turkey, and USA, especially Abdellah, Ahmed, Hassan, Esra, Selver, Gökhan, Evern, Alp, Mohammed, Ziya, Keven, Muga, Huff, Tom, Sarah, Elizabeth, Sourav and many more. I am very proud to have friends like you in my life.

My sincerest appreciation goes to my second country (Turkey) for providing me a PhD scholarship and for the fantastic attitude of the Turkish people to my family and me during the PhD period.

I would like to acknowledge Geology Department, Faculty of Science, Al-Azhar University for the continuous encouragement and support during my PhD period.

Last but not the least, my greatest gratitude goes to my great family; my father Khalifa, my brothers, and my sisters for them immense support all the time. My deepest love and appreciation are going to my small world; my wife and my kids for all the love, support, and care during the hardest situations and times.

March 2018   Abdelrahman KHALIFA

TABLE OF CONTENTS

LIST OF TABLES

LIST OF FIGURES

MORPHOTECTONIC ANALYSIS OF THE EAST ANATOLIAN FAULT ZONE (E. TURKEY) USING REMOTE SENSING TECHNIQUES

SUMMARY

The transform Arabian/Anatolian plate boundary is at the origin of active tectonic structure elements that initiate large and destructive earthquakes. The aim of this thesis is to improve our knowledge and understanding of the fault behavior and deformation remarks by analyzing surface deformation along the East Anatolian Fault (EAF) that is a morphologically very distinct and seismically active left-lateral strike-slip fault that extends for ~400 km forming the Arabian/Anatolian plate boundary in southeastern Turkey. Together with its conjugate the North Anatolian Fault (NAF), the EAF helps accommodate westward escape of the Anatolian plate from the Arabian/Eurasian collision zone. In this thesis, we study morphotectonics and tectonic activity of the EAF and its splay Adıyman Fault (AdF) using the most important tectonic geomorphology indexes and analyzing different satellite images within the Arabian/Anatolian plates deformation zone. The core parts of the thesis focus on the study of morphotectonic indexes along the EAF, examining the geological offsets along the Erkenek Segment of the EAF through analyzing ASTER satellite images, relative tectonic activity assessment of the AdF, and geological and tectonic mapping along the AdF using Landsat 8 satellite images.

The methods used in this thesis work are divided into two parts; the first part describes the importance of the tectonic geomorphology applications as a very useful tool to examine the interplay between tectonic and surface processes that shape the landscape in regions of active deformation and at time scales ranging from days to millions of years. It also presents a review of the most effective morphotectonic indexes (e.g., Mountain front Sinuosity; valley-floor with to valley floor-height; Hypsometric analysis) that are used to evaluate the tectonic activity along the study region. The second section gives a brief view about the application of remote sensing techniques in geology and tectonics and how the techniques have a great power to assess the different tectonic features and trace the structural elements along any active zone. Also, it presents the characteristics of the different satellite data (ASTER and Landsat 8 (OLI)) with the revision of the different method that we used in this study (e.g. Band Ratio Composite and Minimum Noise Fraction Analysis).

The morphotectonic features along the East Anatolian Fault (EAF) are examined for the first time to provide insights into the nature of landscape development and better understanding of variations in tectonic activity and fault evolution. Several geomorphic indices, namely mountain front sinuosity, valley-width to valley-height ratio, stream length-gradient index, basin asymmetry factor, drainage density, and hypsometric analysis are obtained from digital elevation models. We show that mountain front sinuosity varies from 1.01 to 1.46 on five segments. The mean ratio of valley-width to valley-height along the five segments ranges from 0.11 to 1.32, which is well correlated with the mountain front sinuosity values. The stream length-gradient index values are between from 50 and 350 along the studied segments.

Analysis of the basin asymmetry factor of 18 catchments gives values from 1.88 to 26.25 are examined along the study fault zone and we present the basin asymmetry factor with values from 1.88 to 26.25. The drainage density values of the studied catchments range from 3.5 to 5.6. Finally, the hypsometric analysis index of the 18 catchments records high, intermediate, and low relative tectonic activity. The results show that all geomorphic indices are remarkably uniform along the entire fault length, thus implying that its development was essentially coeval along its length, and supporting the view that the present-day Arabian/Anatolian plate boundary (delimited by the EAF) jumped eastwards from the Malatya-Ovacik Fault Zone at ~3 Ma. This is in a good agreement with the nearly uniform geological offsets and the present-day slip rate of ~10 mm/yr along the entire fault as determined by GPS measurements.

The Erkenek Segment is one of the most active and prominent splays of the East Anatolian Fault. To reveal any potential geological offset geology along the AdF is refined by remote sensing techniques. This is because, mapping the geology at high spatial resolution along this segment with conventional mapping techniques is highly challenging due to the complex tectonics and the abundant number of different lithological units of varying spatial extent. Therefore, in this study, we applied image spectral rationing techniques by using the Advanced Spaceborne Thermal Emission and Reflection Radiometer (ASTER) data along the Erkenek Segment. Images created with band ratios with 1/3-1/9-3/9, 7/3-1/7-3/5 and 9/5-5/3-3/1 are found to be remarkably useful for detailed lithological mapping and hence detecting the geological offsets along this section of the fault. Thus, these ASTER band-ratio images can be used for the lithological mapping along the whole EAF and on other regions in the world with similar lithological and geomorphological conditions.

Geomorphic indices that include mountain-front sinuosity, valley floor width-to-valley height ratio, catchment asymmetry factor, hypsometric integrals and curves, and drainage density are calculated to evaluate the relative tectonic activity along the Adıyaman fault. Each geomorphic index is classified into three classes and averaged to define an index for relative tectonic activity (RTA) to allow the Adıyaman Fault to be divided into categories of low, intermediate and high RTA. The results confirm that the Adıyaman Fault is an active fault with intermediate Quaternary tectonic activity, suggesting that it is of minor importance in accommodating plate boundary deformation, consistent with recent crustal motions determined by GPS studies. Nevertheless, it is worthwhile to note that the Adıyaman Fault still poses a significant seismic hazard for the region despite its relatively lower tectonic activity.

Independent Component Analysis (PCA and ICA) and Minimum Noise Fraction Analysis (MNFA) techniques of the Landsat 8 are applied to study the Adıyaman Fault. It is shown that the lithologic units, fault patterns, and morphological and structural features can be mapped highly accurately by using spectral-matching techniques in regions where rocks are well exposed. Inspection of all possible band combinations indicates that PCA 134 and 231, and ICA 132 band combinations give the best false-color composite images for identifying the rock units and contacts. Analysis of MNFA band combinations shows that MNFA 521 band combination also is robust for discriminating the rock units particularly Quaternary clastic units (colluvium/alluvium). MNFA band 1 alone provides the best image to trace the tectonic and structural elements in the study area. The new up-to-date lithologic map of the Adıyaman Fault that we produce upon to the interpretation of processed OLI images reveals several river channels offset and beheaded by the Adıyaman Fault,

verifying its Quaternary activity. This study demonstrates that, when used with the OLI data, the PCA, ICA, and MNFA are very powerful for lithological and structural mapping in actively deforming tectonic zones, and hence can be applied to other regions elsewhere in the world where the climate is arid to semi-arid, and the vegetation cover is scarce.

In generally this study presents the help of the tectonic geomorphology and remote sensing applications to evaluate the tectonic activities of a major plate boundary fault and a minor fault within the Arabian/Anatolian deformation zone. Improving our tectonic understanding of the active regions requires accurate tectonic measurements and data analysis. It so important to link the morphotectonic analysis with the different surface displacements, slip rates, and major seismic events in order to create a complete scenario about the deformation story of the active regions. Also, the new developed remote sensing methods with high-resolution images are required to go deep and gain the most benefits of applying these techniques for geology and tectonics purposes.

UZAKTAN ALGILAMA TEKNİKLERİ KULLANARAK DOĞU ANADOLU FAY ZONU'NUN (TÜRKİYE'NİN DOĞUSU) MORFOTEKTONİK ANALİZİ

ÖZET

Arap-Anadolu levha sınırı boyunca gerçekleşen dönüşüm hareketi, büyük ve yıkıcı birçok depremi başlatan aktif tektonik yapı unsurlarından kaynaklanmaktadır. Bu tez, Akdeniz Bölgesi'ndeki ilginç ve aktif bölgelerden birini temsil eden Doğu Anadolu Fay (DAF) Zonu boyunca yüzey deformasyonunu analiz ederek fay zonu davranışını, deformasyon derecelerini anlamayı ve konu hakkındaki bilgimizi geliştirmeyi amaçlamaktadır. DAF, Türkiye'nin güneydoğusundaki Arap / Anadolu levha sınırını oluşturan ~ 400 km kadar uzanan, morfolojik olarak ayrı ve sismik olarak aktif bir sol yanal doğrultu atımlı faydır. Kuzey Anadolu Fayı (KAF) konjugatıyla birlikte, DAF, Anadolu levhalarının Arap / Avrasya çarpışma bölgesinden batıya kaçışına yardımcı olur. Bu bağlamda, en önemli tektonik jeomorfoloji indekslerini inceleyerek ve Arap-Anadolu tabakalı deformasyon zonu içinde farklı uydu görüntülerini analiz ederek, ana Doğu Anadolu Fayı ve buna bağlı gelişen ikincil Adıyaman Fayı (AdF) boyunca farklı göreceli tektonik seviyeler ve jeolojik sapmalar gözlemlenmiştir.

Bu tez, Türkiye'deki tektonik jeomorfoloji ve uzaktan algılama uygulamalarının Türkiye'deki etkin doğrultu atımlı Fay Zonu bölgeleri boyunca katkısını vurgulamaktadır. Çalışmanın ana kısmı DAF boyunca morfotektonik indeksler üzerinde odaklanmıştır. ASTER uydu görüntüleri incelenerek gözlemlenen DAF'ının Erkenek Segment'i boyunca oluşan jeolojik atımlar incelenip AdF'nin göreceli tektonik etkinliği değerlendirilmiş ve AdF boyunca Landsat 8 ile jeolojik ve tektonik haritalama yapılmıştır.

Bu tezdeki yöntemler iki bölüme ayrılmıştır; Birinci kısımda, tektonik jeomorfolojik uygulamaların öneminden ve bu uygulamaların gün bazından milyonlarca yıl arasında değişen zaman ölçeklerde, araziyi şekillendiren tektonik ve yüzey süreçleri arasındaki etkileşimi incelemek için çok yararlı bir araç olduğundan bahsedilmektedir. Ayrıca, çalışma bölgesi boyunca tektonik aktiviteyi değerlendirmek için kullanılan en etkili morfotektonik indeksleri (örn. Dağ cephesi Sinuositesi; vadi taban yüksekliği ile vadi tabanı; Hipometrik analiz) incelemiştir. İkinci bölüm, jeoloji ve tektonikte uzaktan algılama tekniklerinin uygulanması ve tekniklerin farklı tektonik özellikleri değerlendirmek ve yapısal elemanları herhangi bir aktif bölge boyunca izlemek için nasıl büyük bir güce sahip olduğunu kısaca anlatmaktadır. Ayrıca, bu çalışmada kullandığımız revize edilmiş farklı yöntemler (örn. Bant Oranı Kompozit ve Minimum Gürültü Kesir Analizi) ile farklı uydu verilerinin (ASTER ve Landsat 8 (OLI)) karakteristik özelliklerini sunmaktadır.

Doğu Anadolu Fayı boyunca yer alan morfotektonik özellikler ilk kez incelenmiş olunup arazinin doğasının gelişimi, tektonik aktivite ve fay evrimi ile ilgili varyasyonların daha iyi anlaşılmasına yönelik öngörüler elde edilmiştir. Sayısal yükseklik modellerinden çeşitli jeomorfik indeksler, yani dağ ön sinüsleri, vadi-boy oranına vadi genişliği, akış uzunluğu-gradyan indeksi, havza asimetri faktörü, drenaj

yoğunluğu ve hipometrik analizler elde edilmiştir. Dağ ön sinüsünün beş segmentte 1.01 ile 1.46 arasında değiştiği gösterilmiştir. Beş bölüm boyunca vadi genişliğinin vadi boyuna ortalama oranı 0.11 ile 1.32 arasında değişmektedir, bu da dağın ön sinüs değerleri ile iyi korelasyon göstermektedir. Akış uzunluğu-degrade indeksi değerleri, incelenen bölümler boyunca 50 ile 350 arasındadır. 18 havzadaki havza asimetri katsayısının analizi, çalışma fayı bölgesi boyunca 1.88'den 26.25'e kadar olan değerler incelenmekte ve havza asimetri faktörü 1.88'den 26.25'e kadar olan değerler ile sunulmaktadır. İncelenen havzaların drenaj yoğunluğu değerleri 3.5 ila 5.6 arasındadır. Son olarak, 18 havzanın hipersometrik analiz indeksi yüksek, orta ve düşük göreceli tektonik aktiviteyi kaydeder. Sonuçlar, tüm jeomorfik indekslerin tüm fay uzunluğu boyunca dikkat çekici derecede muntazam olduğunu ve bu nedenle gelişiminin esas olarak boy uzunluğu boyunca uzandığını ve günümüz Arap / Anadolu levha sınırının (DAF tarafından sınırlandırılan) doğuya doğru fırladığı görüşünü desteklediğini göstermektedir. Malatya-Ovacık Fay Zonu'ndan ~ 3 Ma. Bu, neredeyse tekdüzen jeolojik ofsetleri ve GPS ölçümleri ile belirlenen tüm hata boyunca mevcut olan 10 mm / yıl'lık kayma oranı ile iyi bir anlaşma içerisindedir.

Erkenek Kesimi boyunca yer alan jeoloji, Doğu Anadolu Fayı'nın en aktif parçası olarak çalışılmıştır. Konvansiyonel haritalama teknikleriyle bu bölüm boyunca yüksek uzamsal çözünürlükte jeolojinin haritalanması, karmaşık tektoniklere ve değişken mekansal ölçüde farklı litolojik birimlere bağlı olarak oldukça zordur. Bu nedenle, bu çalışmada, aralık spektrumu boyunca Gelişmiş Spaceborne Termal Emisyon ve Yansıma Radyometresi (ASTER) verilerini kullanarak görüntü spektral rasyonlama teknikleri uygulanmıştır. 1 / 3-1 / 9-3 / 9, 7 / 3-1 / 7-3 / 5 ve 9 / 5-5 / 3-3 / 1 ile bant oranlarıyla oluşturulan görüntüler, ayrıntılı litolojik ve jeolojik haritalama için ve dolayısıyla fayın bu bölümü boyunca jeolojik ofsetlerin tespit edilmesi için oldukça faydalıdır. Böylece, bu ASTER bant-oranı görüntüleri, tüm EAF boyunca ve benzer litolojik ve jeomorfolojik koşullara sahip dünyadaki diğer bölgeler boyunca litolojik haritalama için kullanılabilir.

Dağ önü sinüs, vadi taban genişliği-vadi yükseklik oranı, yakalama asimetri faktörü, hipometrikometrik integraller ve eğriler ve drenaj yoğunluğu gibi jeomorfik indeksler Arap / Anadolu levhası sınırları içindeki Adıyaman fayı boyunca göreceli tektonik aktiviteyi değerlendirmek için çok dikkatli hesaplanmıştır. Her bir jeomorfik indeks, üç sınıf olarak sınıflandırılmış ve Adıyaman Fayı'nın düşük, orta ve yüksek RTA kategorilerine ayrılmasına izin veren bir tektonik aktivite (RTA) indeksi tanımlamak için ortalaması alınmıştır. Sonuçlar, Adıyaman Fayı'nın, aradaki Kuvaterner tektonik aktivitesi ile aktif bir fay olduğunu ve bu durumun, GPS çalışmalarıyla belirlenen son kabuk hareketleri ile tutarlı olarak, levha sınır deformasyonunun sağlanmasında az bir öneminin olduğunu düşündürmektedir. Yine de, Adıyaman Fayı'nın nispeten düşük tektonik aktivitesine rağmen bölgeye hala önemli bir deprem tehlikesi oluşturduğuna dikkat çekmek önemlidir.

Adıyaman Fayı'nı incelemek için Landsat 8'in Bağımsız Bileşen Analizi (PCA ve ICA) ve Minimum Gürültü Kesir Analizi (MNFA) teknikleri uygulanmıştır. Kayaçların iyi bir şekilde açığa çıkarıldığı bölgelerde, litolojik birimler, fay modelleri ve morfolojik ve yapısal özelliklerin spektral eşleştirme teknikleri kullanılarak yüksek doğrulukta haritalanabileceği belirtilmektedir. Tüm muhtemel bant kombinasyonlarının incelenmesi, PCA 134 ve 231 ve ICA 132 bant kombinasyonlarının, kaya birimleri ve kontaklarını tanımlamak için en iyi yanlış-renk kompozit görüntüleri verdiğini göstermektedir. MNFA bant kombinasyonlarının analizi, MNFA 521 bant kombinasyonunun, özellikle Kuvaterner klastik birimlerin

(kolüvyon / alüvyon) ayırdedilmesi için sağlam olduğunu göstermektedir. Tek başına MNFA bandı 1, çalışma alanındaki tektonik ve yapısal elementleri izlemek için en iyi görüntüyü sağlamaktadır. İşlenmiş OLI görüntülerinin yorumlanmasında üretilen Adıyaman Fayı'nın güncel litolojik haritası, birçok nehir kanalının Adıyaman Fayı tarafından kesilmiş olduğunu ve buna bağlı olarak Kuaterner aktivitesinin varlığını göstermektedir. Bu çalışma, OLI verileriyle kullanıldığında, PCA, ICA ve MNFA'nın, tektonik bölgeleri aktif olarak deforme eden litolojik ve yapısal haritalama için çok güçlü olduğunu ve bu nedenle, iklimin kurak-yarı kurak ve bitki örtüsünün az olduğu dünyanın başka bölgelerine de uygulanabileceğini göstermektedir.

Genel olarak, bu çalışma, tektonik jeomorfoloji ve uzaktan algılama uygulamalarının, Arap-Anadolu deformasyon zonu içindeki ana plaka sınır fayı (EAF) ve minör fayın (AdF) tektonik aktivitesinin değerlendirilmesine katkısını sunmaktadır. Aktif bölgelerdeki tektonik anlayışımızı geliştirmek, doğru tektonik ölçümler ve veri analizi gerektirmektedir. Aktif bölgeler hakkında tam bir senaryo oluşturmak için morfotektonik analizi farklı yüzey yer değiştirmeleri, kayma oranları ve büyük sismik olaylar ile ilişkilendirmek çok önemlidir. Ayrıca, yüksek çözünürlüklü görüntülere sahip yeni geliştirilmiş uzaktan algılama yöntemlerinin derinlere inmesi ve bu tekniklerin jeoloji ve tektonik amaçlarla kullanılmasının en büyük yararının elde edilmesi gerekmektedir.

1. INTRODUCTION

Turkey represents one of the most seismically active regions in the world. As a result, it has a long history of large destructive earthquakes, including the Kocaeli (*M = 7.4*) and Düzce (*M = 7.2*) events of 17 August and 12 November 1999, near Istanbul. It is located within the 'Mediterranean Earthquake Belt', whose complex deformation results from the continental collision between the African and Eurasian plates (Figure 1.1). Therefore, Turkey is an excellent natural laboratory to study post-collisional intracontinental convergence- and tectonic escape-related deformation and the consequent structures that include fold and thrust belts, suture zones, active strike-slip faulting, and active normal faulting and the associated basin formation (Bozkurt, 2001).

The neotectonics of Turkey is dominated by three major tectonic elements: (1) the Aegean-Cyprean Arcs, a convergent plate boundary where the African Plate to the south is subducting beneath the Anatolian Plate to the north; (2) the right-lateral North Anatolian Fault Zone; and (3) the left-lateral East Anatolian Fault Zone (Figure 1.1). The latter two are intracontinental strike-slip faults along which the Anatolian Plate, a wedge of amalgamated fragments of crust, moves westward away from the collision zone between the Arabian and the Eurasian plates (Şengör et al., 1981; Barka, 1992; Bozkurt, 2001). This activity is the result of interactions between northward-moving African and Arabian plates and the relatively stable Eurasian Plate. The two strike-slip faults meet and form a continental triple junction to the east of Karlıova in northeastern Turkey (Figure 1.1).

1.1 Major Tectonic Elements

1.1.1 Aegean-Cyprean Arcs

Along the Aegean and Cyprean arcs, African Plate is descending beneath the Anatolian Plate in a N-NE direction in Eastern Mediterranean region (Mart and

1

Woodside, 1994; McKenzie, 1978; Papazachos; 1997). However, the geometry and the nature of these arcs are still under debate (Bozkurt, 2001).
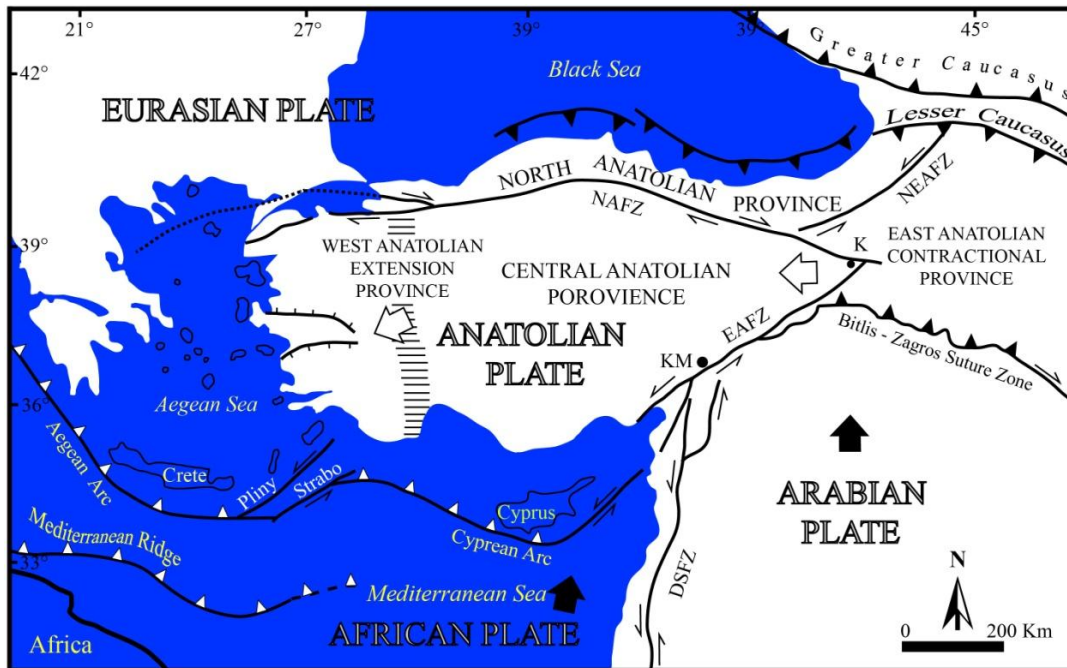
Figure 1.1 : Simplified tectonic map of Turkey showing major neotectonic structures and neotectonics provinces (from Şengor et al. (*1985*); Barka (1992); Bozkurt (2001)). *Abbreviations*: K, Karlıova; KM, Kahramanmaraş; DSFZ, Dead Sea Fault Zone; EAFZ, East Anatolian Fault Zone; NAFZ, North Anatolian Fault Zone; NAFZ, Northeast Anatolian Fault Zone. Heavy lines with arrows are strike-slip faults with arrows showing relative movement sense. Heavy lines with black triangles show major fold and thrust belt: small triangles indicate the direction of convergence. Heavy lines with white triangles indicate an active subduction zone. The heavy lines with hachures show normal faults. The hatched area shows the transition zone between the western Anatolian extensional province and the central Anatolian 'ova' province.

The Aegean arc system represents an important factor in the geodynamical evolution of the Aegean region. The western extension of the Aegean arc is characterized by Ionian trench while the eastern part of the arc acts rather as transform fault (Le Pichon et al., 1979). Several trenches (e.g., the Pliny, SE Cretan, and the Strabo trenches) have been distinguished along the eastern parts of the Aegean Arc (Jongsma, 1977). Le Pichon and Angelier (1979) suggested that the initiation of subduction along the Aegean Arc has taken places approximately 13 Ma ago. While, others claimed that the age of Aegean subduction zone is at least 26 Ma (e.g., Meulenkamp et al., 1988). Also, younger ages (5-10 Ma) were recorded by (Mercier, 1979; McKenize, 1992) for the Mediterranean subduction. The migration of the trench system to south-southwest (subduction roll-back processes) resulted in

extensional regime in the overriding Aegean plate (back-arc region) that subsequently led the formation of the present-day Aegean Sea (Le Pichon and Angelier,1981; Bozkurt, 2001).

The Cyprean Arc is considered the presently active plate boundary, which accommodates the convergence between the African plate to the south and the Anatolian Plate to the north in the eastern Mediterranean (McKenize, 1970; McKenize, 1972; Dewey et al., 1973; Smith, 1971; Nur and Ben-Avraham, 1978; Vidal et al., 2000) (Figure 1.1). West of Cyprus, northeastward subduction of the eastern Mediterranean oceanic crust has been examined based on seismic data and the continuation of the plate boundary from the Aegean arcs (Woodside, 1977; Dewey and Şengör, 1979; Oral et al., 1995; Vidal et al., 2000; Bozkurt, 2001). South of Cyprus, the northward subduction is affected collision of Eratosthenes Seamount (Robertson and Grasso, 1995; Glover and Robertson, 1998). In contrast to the previous information, McKenize (1972); Morelli (1978); Robertson and Grasso (1987) confirmed that there is no evidence of subduction to the east of Cyprus. The seismicity around the Cyprean region have been examined by many researchers (e.g. Ambraseys, 1965; Salamon, 1696) and they recorded strong earthquakes with *M=6.0* or higher during the instrumental period.

1.1.2 North Anatolian Fault (NAF)

The North Anatolian Fault (NAF) is one of the active transform strike-slip faults around the world. It is extremely well-developed surface importance for the tectonics of eastern Mediterranean region (Ketin, 1968; Şengör et al., 1985; Kiratzi, 1993). The dextral strike-slip NAF is 40 km wide and it starts around Karliova triple junction in eastern Turkey and it runs to Greece in the west for 1500 Km (Figure 1.1). This transform zone represents part of the Plate boundary between Eurasian Plate toward the north and Arabian Plate to the south. Around east of the Sea of Marmara, the NAF separates into northern and southern major strands (Figure 1.1). The northern segment runs in part of the Sea of Marmara and represents the most active section of the NAF zone, while the southern strand bounds the southern margin of Sea of Marmara, then runs in SW direction into the Aegean Sea.

The age and cause of NAF motion have many different views: (1) Mckenzie, (1970) and Şengör, (1979) stated that the dextral motion initiated by Middle Miocene and it

was caused by the westward Anatolian motion away from the eastern Turkey collision zone when Arabian and Eurasian plates collided. (2) Other view claimed that the NAF initiation time was between latest Miocene and Early Pliocene (Koçyiğit, 1989; Bozkurt and Koçyiğit, 1996; Yiltırak, 1996). Also, different view suggests that the initiation of the NAF occurred in the eastern Anatolian during the Late Miocene and propagated westwards to the Sea of Marmara during the Pliocene (*Şengör, 1979; Yiltırak et al., 2000*). However, Barka and Kadinsky-Cade (1988) introduce a lot of evidence to date the NAF as the earliest Pliocene (~5 Ma).

The Geological offsets along the NAF were examined by many workers (e.g. Tatar 1978; Şengör, 1979; Şengör et al., 1985; Şaroğlu, 1988; Koçyigit, 1990; Barka, 1992; Armijo, 1999) that recorded it to be range between 20-25 Km to 85 ± 5 km. Depending on the geological data analysis the rate of motion on the NAF is ~ 5-10 mm/y (Barka, 1992), or ~ 17 ± 2 mm/y (Westaway, 1994), while the seismological data indicated rates of 30-40 mm/y (Taymaz, 1991). On the other hand, recent GPS data suggest present-day rates of ~ 15-25 mm/y (Reilinger, 1997; McClusky, 2000).

Recently, NAF has produced many earthquakes with different magnitudes, these include 1939 December, 26 Erzincan (*M=7.9-8.0*), 1942 December, 20 Erbaa-Niksar (*M =7.1*), 1943 November, 26 Tosya (*M=7.6*), 1944 February, 1 Bolu- Gerede (*M = 7.3*), 1957 May, 26 Abant (*M=7.0*), 22 July 1967 Mudurnu valley (*M=7.1*), 1992 March, 13 Erzincan (*M = 6.8*), 1999 August, 17 Kocaeli (*M = 7.4*), and 1999 November, 12 Düzce earthquakes (Ketin, 1968; Ambraseys, 1970; McKenzie, 1970; Koçyigit, 1990; Barka, 1993; Toksöz, 1999).

Since the Erzincan and Kocaeli earthquakes that were happened in 1999, NAF in the Marmara region became the area of intense research for many workers (e.g. Okay et al., 1999; Selim et al., 2013; Şengör et al., 2014). Many Different models have been suggested for the origin of Sea of Marmara to examine the deformation and dynamics of the strands of the NAF and to reveal the origin and evolution of Sea of Marmara (e.g. Crampin and Evans, 1986;Barka et al., 1987; Barka, 1992; Westaway, 1994; Wong et al., 1995; Görür et al., 1997; Hubert et al., 2000; Yaltırak, 2000). However, the nature and length of faults in the Sea of Marmara are still under debate.

The land section of the NAF is well known and mapped because of the well-developed surface expression and geological features, while our knowledge about the geometry of the NAF in the Sea of Marmara is limited (Şengör et al., 2005; Bozkurt, 2001). Recently, seismic reflection studies in the sea of Marmara region give new light on the geology and structure of the region (Le Pi chon et al., 1999; Okay et al., 1999 and 2000). The Sea of Marmara region includes several deep marine strike-slip catchments (e.g., Central Marmara, Tekirdağ catchments), separated by NE-trending submarine ridges that rise several hundreds of meters above the seafloor. There are two distinct, steep, continuous bathymetric features (submarine escarpments) that bound the Sea of Marmara, both in the north and in the south, and mark the location of major active faults (Tüysüz et al., 1998; Bozkurt, 2001).

The Sea of Marmara region also represents a transition zone between the area of pure strike-slip deformation, where the Anatolian Plate is displaced westward in the north and the western Anatolian extensional province with diffuse N-S extension (Figure 1.1*; Şengör et al., 1985). The GPS measurements around the Sea of Marmara show that the Anatolian Plate is moving westward at a rate of about 20 mm/y (Straub and Kahle, 1995; Reilinger et al., 1997; Straub et al., 1997).

This thesis mainly aims to investigate and discuss the tectonic behaviors along the East Anatolian Fault zone. Therefore, we try to review the East Anatolian Fault in details through the next section.

1.1.3 East Anatolian Fault (EAF)

The Seismically Active Left-lateral strike-slip East Anatolian Fault (EAF) is one of the major transform faults in the Eastern Mediterranean Region (Figure 1.1). It extends for ~400 Km, tracing a plate boundary between Anatolian and Arabian plates in eastern Turkey. EAF with the Right-lateral strike-slip North Anatolian Fault (NAF) accommodate the westward extrusion movement of the Anatolian microplate (AN) (McKenzie 1972, 1976; Şengör, 1979, 1980; Jackson and McKenzie 1984; Şengör et al. 1985; Dewey et al. 1986; Duman and Emre, 2013). The EAF was first described by Allen (1969) and its transform nature was first defined and mapped by Arpat and Şaroğlu (1972). Many researchers (e.g., Arpat 1971; McKenzie 1972; Arpat and Şaroğlu 1975; McKenzie 1976, 1978; Jackson and McKenzie 1984; Dewey et al. 1986; Ambraseys 1988; Taymaz et al. 1991; Westaway and Arger 1996;

Westaway 2003, 2004; Bulut, et al. 2012; Duman and Emre, 2013; Aktuğ,2016; Khalifa, et al., 2018) investigated EAF importance for the regional seismicity and active tectonics during the Quaternary-Holocene period or near the latest Pliocene-Pleistocene boundary (Herece, 2008).

The EAF merges with the NAF at the Karlıova triple junction. Some researches (*e.g.* McKenzie 1976; Gülen et al. 1987; Karig and Kozlu 1990; Perinçek and Çemen 1990; Westaway & Arger 1996; Westaway 2003, Khalifa et al., 2018) suggested that the EAF connects the Dead Sea Fault (DSF) in Maraş triple junction and then passes westwards to cut the Amanos Mountains while, others argued that the Amanos Fault represents part of the EAF thus extends between Karlıova and Amik Triple junctions (Arpat and Şaroğlu, 1972, 1975; Şaroğlu et al., 1992a, b; Herece 2008; Karabacak et al., 2010).

The EAF historical and instrumental seismicity records reveal great differences between historical and recent seismicity, respectively (Bulut et al., 2012). Ambraseys and Jackson (1998) recorded the largest famous earthquakes along the EAF that include November 29, 1114 (*M > 7.8*), March 28, 1513 (*M > 7.4*) and March 2, 1893 (*M > 7.1*). Importantly, during the last century, the EAF zone has produced only one large earthquake (December 4, 1905; *M = 6.8*) (Nalbant et al., 2002) while the NAF comprises many large earthquakes (*M>7*) that occurred almost along the entire NAF (e.g. Toksöz et al., 1979; Bulut, 2012). Also, the apparent seismic quietness along the EAF was interpreted by Çetin et al. (2003) that confirmed that the EAF is now locked.

According to Bozkurt (2001) the age of the East Anatolian Fault is under a great range of debate, it is categorized into four views: (1) Arpat and Şaroğlu (1972), Şengör et al. (1985), Dewey et al. 1986, Hempton (1987), Perinçek and Çemen (1990), and Lybéris et al (1992) proposed that the EAF was placed in the Late Miocene-Early Pliocene; (2) Şaroğlu et al. (1987, 1992a) suggested that the EAF was initiated during the Late Pliocene; (3) the third view were suggested by Yürür and Chorowicz (1998), and they confirmed that the EAF started to form from 1.8 Ma; Finally, (4) Westaway and Arger (1998) concluded that the EAF fault zone began to be active around 3 Ma when the activity of Malatya-Ovacık fault zone was ceased. The idea of Yürür and Chorowicz (1998) was based on the suggestion that the Volcanism that is located in the south of kahramanmarş and Karasu Valley is the

same unit, belonging to the Quaternary, and initiated at 1.8 Ma. They assumed that the studied volcanism is extension-related, and required the presence of geometry of strike-slip faulting. In contrast, Arger et al., (2000) dated the same volcanism to be Miocene (19-15Ma) and argued that this volcanism did undergo any effect from either extension or strike-slip movement.

The accumulated overall offsets along the EAF vary between an upper range of 27–33 km that is recorded by geological features and the length of the Golbaşi strike-slip basin (Westaway and Arger, 1996; Bulut et al., 2012), and 15–22 km that is defined by drainage channels offsets on individual fault segments (Hempton, 1987; Bulut et al., 2012). Studies based on the geologic and geomorphic data along the EAF provide slip rates of between 6 and 11 mm/yr (Arpat and Şaroğlu, 1975; Wastaway, 1994; Kiratzi, 1993; Yürür and Chorowicz, 1998; Çetin et al., 2003; Aksoy et al., 2007; Herece, 2008; Duman and Emre, 2013, Yönlü et al., 2013), whereas the GPS studies provide a constant slip rate ~10 mm/yr along the whole EAF (Reilinger et al., 2006; Mahmoud et al., 2013; Aktuğ et al., 2016).

The EAF zone comprises some strike-slip basins and secondary pure strike-slip faults that are parallel to the plate motion and act as transform faults, and others where the faulting is oblique to the plate motion (Bozkurt, 2001). Adıyaman Fault is one of the secondary strike-slip faults that are parallel to the main East Anatolian Fault. It is extending ~ 75km in ~ 65° NE direction. The seismicity along the Adıyaman Fault is characterized by low to moderate earthquakes (*M_w 3.0–5.5*) (Figure 1.2).

The Malatya and Ovacık faults located to the north of the EAF are secondary structures with a left lateral sense of slip within the study region. Koçyiğit and Beyhan (1998) and Kaymakci et al. (2006) considered the different segments of Malatya and Ovacık fault zones to be part of the Malatya-Ovacık Fault Zone (MOFZ) (Figure 1) whose present-day activity is debated by Jackson and Mckenzie (1984), Westaway and Arger (1996, 2001), Koçyiğit and Beyhan (1998), and Kaymakci et al. (2006). Westaway and Arger (2001) interpreted the SW- and SSW-trending segments of the MOFZ as transform faults and argued for ~240 km left-lateral along the MOFZ making it one of the major fault zones in eastern Turkey. Based on the geometry of the former Erzincan triple junction, which differs from the modern Karlıova triple junction, Westaway and Arger (2001) suggest that the MOFZ is no longer active. While some researchers, e.g., Jackson and Mckenzie (1984) and

Westaway and Arger (1996, 2001), state that the EAF zone was initiated and at the same time the significant movement of the MOFZ ceased at the end of the Early Pliocene (~3 Ma). In contrast, Koçyiğit and Beyhan (1998) and Kaymakci et al. (2006) claim that the MOFZ is still active.
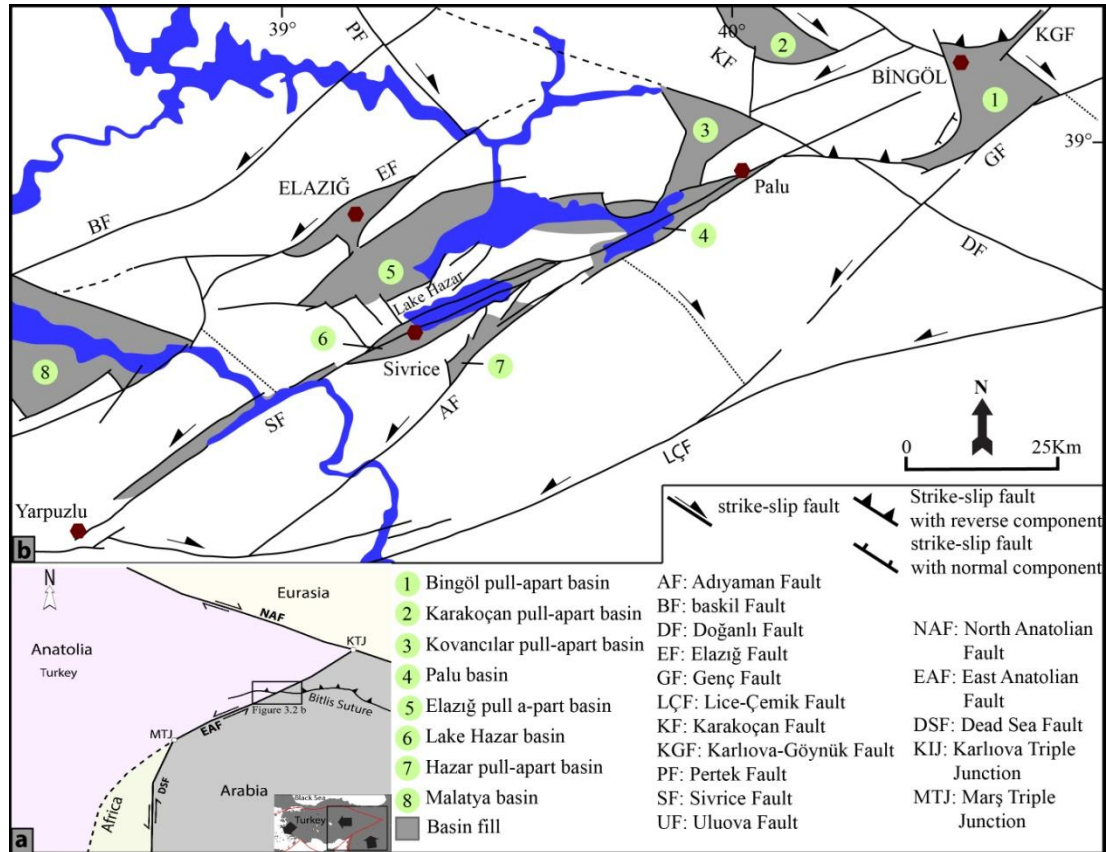
Figure 1.2 : (a) Simplified map showing major plates and their boundary faults in the eastern Turkey region and location of the Lake Hazar basin; (b) simplified neotectonic map showing some major faults and strike-slip basins comprising the East Anatolian Fault (EAF) in the Lake Hazar and Bingöl region (After Aksoy et al. 2007).

The evolution of the Euphrates River, offset by the EAF, can be summarized as follows. After activity along the MOFZ ceased, lacustrine sedimentation smoothed out the surface relief leaving a subdued topographic low along the line of the MOFZ. Then drainage started to develop along the length of the MOFZ to form the modern Euphrates gorge that crosses the EAF, which now provides the outlet from the Malatya basin (Westaway and Arger, 2001). The Euphrates River was then offset ~13 km by the EAF. However, the total slip on this strand is debated, with estimates up to ~30 km (Westaway, 1994; Westaway and Arger, 2001). Westaway and Arger (2001) argue that the modern Euphrates River began to form at ~1.3–3 Ma, with the

assumption that the majority of the gorge development occurred in the last 1 Ma. Thus, a long-term slip-rate for the EAF of ~8.3 mm/yr is based on the offset of the Euphrates River for the past 3 Ma (Herece and Akay, 1992).

The EAF was segmented by many researchers into several distinct numbers of strands (e.g. Arpat and Şaroğlu 1972; Arpat and Şaroğlu 1975; Hempton et al. 1981; Muehlberger and Gordon 1987; Barka and Kadinsky-Cade, 1988; Herece and Akay 1992; Şaroğlu et al. 1992a; Westaway 1994; Herece 2008; Duman and Emre, 2013, Khalifa et al., 2018). According to fault geometry and variations in trends of the segments, the EAF divided into five segments (Hempton et al., 1981). Barka and Kadinsky-Cade (1988) and *Duman and Emre* (*2013*) also segmented the EAF into distinct fourteen and thirteen segments, respectively between Karlıova and Türkoğlu based on the seismicity behaviors of the fault zone, the extent of the surface rupture, and the location of the geometric discontinuous. Şaroğlu et al. (1992a) defined 6 different segments between Karlıova and Antakya based on stepovers and changes in segments strikes. Herece (2008) recognized eleven geometric segments for the same EAF distance.

1.1.4 Dead Sea Fault (DSF)

Dead Sea Fault (DSF) is a left-lateral strike-slip transform fault that extends approximately for ~1000Km from the Red Sea in the south to the East Anatolian Fault to the north. From the plate tectonics point of view, the DSF represents plate boundary of transform type, differentiating the African Plate to the west and Arabian Plate to the east (Şengör et al., 1981; Rotstein and Kafka 1982; Dewey et al., 1986; Gülenet al., 1987). The Arabian Plate is moving northward faster than the African Plate (Oral et al., 1995; Barka and Reilinger, 1997; Reilinger et al., 1997). This differential movement between the plates is taken up by DSF (*Bozkurt, 2001*).

The age of the DSF is examined and argued into four major ages: (1) Middle Miocene (Garfunkel et al., 1981). (2) Late Miocene, (Lybéris, 1988; Steckler et al., 1988). (3) Later than at 20 Ma (Eyal et al., 1981; Steinz and Bartov, 1991). (4) at around 18 Ma (Early Miocene: (Hempton, 1987; Garfunkel, 1996). The offsets along the DSF were suggested to be 110km for the southern section (Freund et al., 1970; Bandel and Khouri, 1981) and 70–80 km for the northern section (Dubertet, 1966).

2. METHODOLOGY

2.1 Tectonic Geomorphology

2.1.1 Introduction

Tectonic geomorphology analysis is marked as quantitative measurement of landscape shape. At the simplest view, landforms can be characterized in terms of their size, elevation, and slope. Quantitative measurements allow researchers objectively to compare different landforms and to calculate less straightforward parameters (geomorphic indexes) that may be useful for identifying a particular characteristic of a region (its level of tectonic activity).

Some geomorphic indices have been developed as basic reconnaissance tools to identify areas experiencing rapid tectonic deformation. This information is used for planning research to obtain detailed information about active tectonics. Other indices were developed to quantify description of the landscape. Geomorphic indices are particularly very important in tectonic studies because they can be used for rapid evaluation of large regions and the necessary data often can be obtained easily from topographic maps and aerial photographs. Some of the geomorphic indices are most useful in studies of active tectonics such as Hypsometric integral by Strahler (1952), Asymmetry Factor by Cox (1994), Stream length-gradient index developed by Hack (1973), Mountain front sinuosity developed by Bull and Mc Fadden (1977), Ratio of valley floor width to valley height etc. (Keller and Pinter 2002). Mountain front, valley, sinuosity of the channels are surface features that construct the arid to semi-arid landscape and exists at large or small scales. To understand the way landforms evolve, it is essential to study the underlying geology. In general, landform development implies deep structures of the earth; therefore there is always a strong relationship between landscape and the geologic environment (Keller and Pinter 2002). Morphotectonics has been considered as a tool to determine the intensity of tectonic activity in the tectonically active regions (Wells, Bullard et al. 1988; Merritts and Vincent 1989).

2.1.2 Geomorphic indices

2.1.2.1 Mountain front sinuosity (S_{mf})

S_{mf} helps define the relationship between the total length of the mountain front and the straight-line distance along the mountain front (Bull, 1977; Azor et al., 2002; Keller and Printer, 2002). This index helps explore links between tectonics and erosion and is defined as:

$$Smf = Lmf / Ls \tag{2.1}$$

where L_{mf} is the length of the mountain front and L_s is its straight-line length (Figure 2.1).
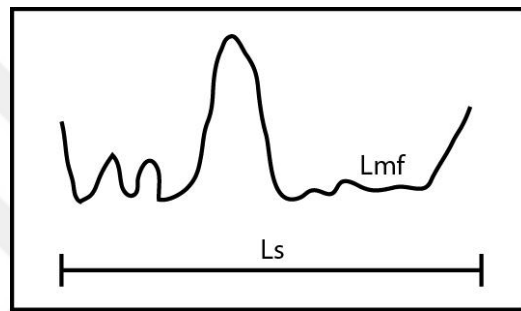
Figure 2.1 : Diagram showing total length of mountain front (L_{mf}) and straight-line length (L_s) of the mountain front.

2.1.2.2 Valley width to valley height ratio (V_f)

V_f defines the differences in valley shape and may reflect the degree of active uplift, and/or base level fall, and is defined as:

$$V_f = 2V_{fw} / [(E_{ld} - E_{sc}) + (E_{rd} - E_{sc})] \tag{2.2}$$

Where V_{fw} is the width of the valley floor, E_{rd} and E_{ld} are the elevations of the right and left valley divides respectively, and E_{sc} is the average elevation of the valley floor (Keller and Printer, 2002; Figure 2.2).

Azor et al. (2002) suggest that high values of V_f usually indicate low tectonic activity, whereas low values of V_f indicate areas of high tectonic activity with relatively rapid uplift and valley incision. V_f Index has been calculated at a prescribed distance (1 up to 3 Km) from the mountain front based on the size of the drainage regions (Silva et al., 2003).
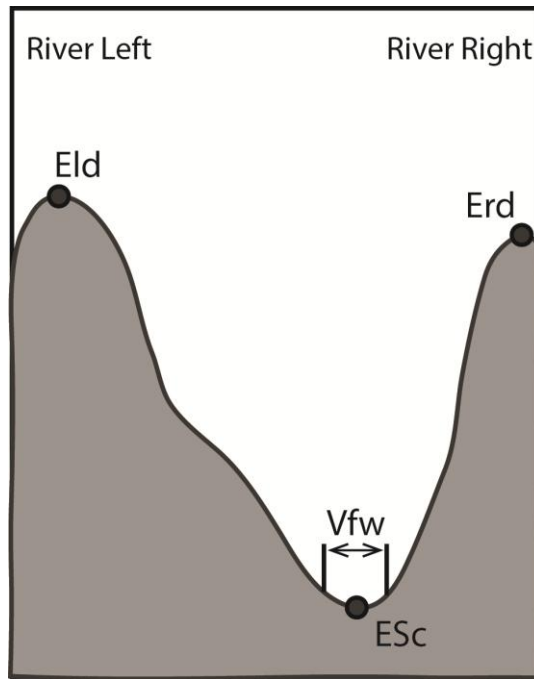
Figure 2.2 : Calculating valley floor width to height ratio (Keller and Pinter, 2002).

2.1.2.3 Stream length-gradient index (S_L)

The S_L index is sensitive to channel slope, which, in turn, can be used as a proxy for tectonic activity, stream power, or rock resistance. The erosional resistance of rocks and relative intensity of active tectonics can be evaluated using the S_L by calculating changes of stream gradients along drainage catchments (Hack, 1973; Keller and Printer, 2002). The index is defined as:

$$S_L = (\Delta H / \Delta L) \times L \qquad\qquad (2.3)$$

where $\Delta H/\Delta L$ is the channel gradient for a stretch of the stream (ΔH is the elevation change for a particular channel reach with respect to ΔL, i.e., the length of the reach) and the total channel length L from the midpoint of the reach where the index is calculated upstream to the drainage divide (Figure 2.3). The S_L index is generally calculated for a large number of reaches along major streams within a study area (Azor et al., 2002).
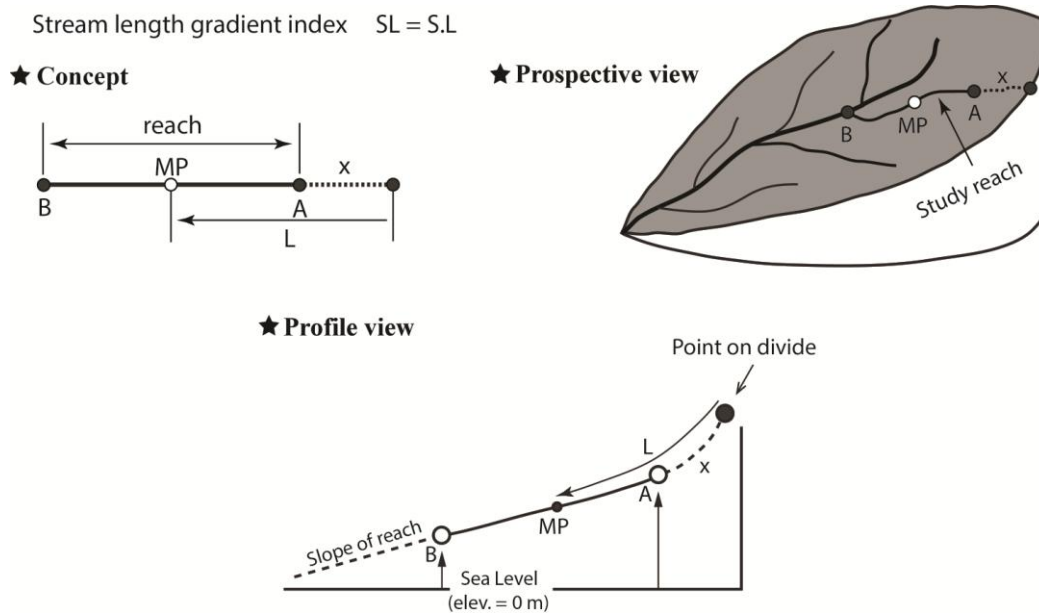
Figure 2.3 : Diagram shows the process of calculating the Stream Length-Gradient Index (SL) for a given creek (Keller and Pinter, 2002).

2.1.2.4 Basin asymmetry factor (A_F)

The A_F may be utilized to help detect tectonic tilting from drainages that transverse a structure and is defined as:

$$A_F = 100 \ (Ar \ / \ At) \tag{2.4}$$

where Ar is the area of the drainage basin to the right of the main stream and At is the total area of the basin (Figure 2.4). The A_F is sensitive to tilting perpendicular to the trend of the main stream. An A_F of 50 represents a tectonically stable setting, while values smaller or greater than 50 suggest tilting and indicate that a basin is tectonically active (Keller and Pinter, 2002). Values of AF include the AF-50 that is the difference amount between the neutral value of 50 and the observed value (El Hamdouni, 2008). In order to evaluate the relative tectonic activity, an absolute difference is necessary. Following to El Hamdouni (2008)'s method, we categorize the absolute values of AF into class 1 ($\lvert$AF-50$\rvert$ > 15), class 2 ($\lvert$AF-50$\rvert$: 7-15), and class 3 ($\lvert$AF-50$\rvert$ < 7). El Hamdouni (2008) classified the average of the different classes into four activity levels, where level 1 is very high relative tectonic activity (1 - 1.5); level 2 that indicates highly relative tectonic activity (> 1.5 to ≤ 2); level 3 is moderately relative active tectonics (> 2 to ≤ 2.5); and level 4 that is the lowest level of relative tectonics (> 2.5).
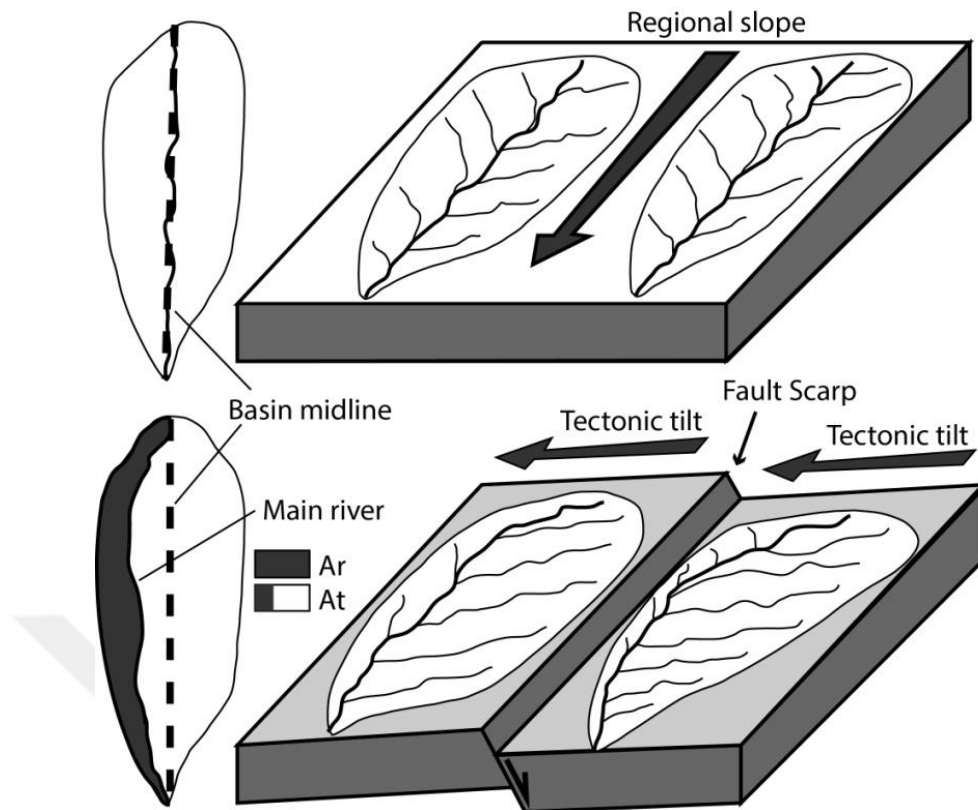
Figure 2.4 : Water system diagram shows uplift along a normal fault by moving laterally in a down-tilt direction, Ar is the area of the basin to the right of the trunk stream and At is the total area of the basin (modified after Mahmoud and Gloaguen, 2012).

2.1.2.5 Drainage density (Dd)

Azor et al., (2002) and Keller and Pinter, (2002) introduce Dd as the ratio of total channel length versus catchment area. Greater values of Dd suggest more extensively developed on older landforms for a relatively long time, while regions experiencing the most recent tectonic activity have lower Dd values (*Keller and Pinter, 2002*).

Drainage density is defined as:

$$Dd = L / A \qquad\qquad (2.5)$$

where L is the length of the channel and A is the catchment area.

2.1.2.6 Hypsometry

The hypsometric integral (Hi) is a quantitative measure of the distribution of elevation within a catchment (Langbein, 1947; Strahler, 1952). This index serves to compare catchments and is an expression of the volume of the catchment that has not

been eroded. Simply expressed, the Hi-index (Pike and Wilson, 1971; Mayer, 1990) is defined as:

$$Hi = (Emean – Emin) / (Emax – Emin) \qquad (2.6)$$

where Emean is the mean elevation, Emax is the maximum elevation, and Emin is the minimum elevation.

The hypsometric curve of a catchment is a cumulative area versus elevation plot, which likely reflects the dominant geomorphic processes operating in the catchment. A convex curve indicates uplift with dominant hillslope processes, such as sliding and soil creep, while a concave curve indicates channelized/linear/fluvial/alluvial processes. In essence, young catchments (tectonically active) have Hi values (≥ 0.45) and convex hypsometric curves, whereas low Hi values (≤ 0.3) and concave hypsometric curves indicate old catchments (tectonically quiescent).
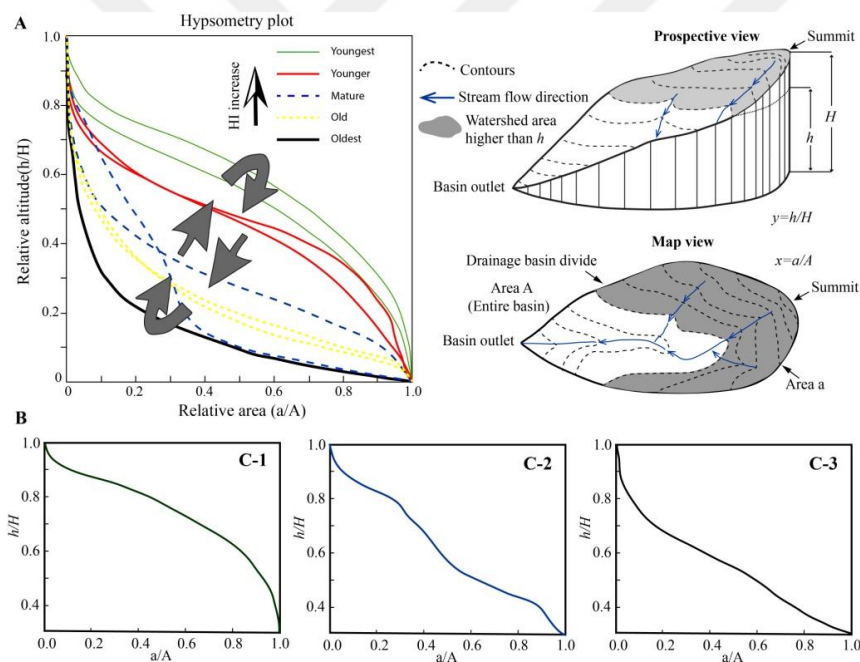
Figure 2.5 : Different types of hypsometric curves after (Strahler, 1952) and geomorphic cycle development (Perez-Pena et al., 2009; Mahmood and Gloaguen, 2012) show changes in hypsometric curves (A), convex (C-1) describes youthful stages, S-shaped curves and concave curves together (C-2) and (C-3) is typical for mature and old stages (B).

2.2. Remote Sensing

2.2.1 ASTER

ASTER is the Advanced Spaceborne Thermal Emission and Reflection Radiometer, a multi-spectral sensor onboard one of NASA's Earth Observing System satellites, Terra, which was launched in 1999. ASTER sensors measure reflected and emitted electromagnetic radiation from Earth's surface and atmosphere in 14 channels (or bands) (*Table 2.1*). There are three groups of channels: three recording visible and near-infrared radiation (VNIR), at a spatial resolution of 15m; six recording portions of shortwave infrared radiation (SWIR) at a spatial resolution of 30m; and five recording thermal infrared radiation (TIR) at a resolution of 90m. The higher spectral resolution of ASTER (compared to Landsat, for example - *Figure1*), especially in the shortwave infrared region of the electromagnetic spectrum, makes it possible to identify minerals and mineral groups such as clays, carbonates, silica, iron-oxides and other silicates. An additional backward-looking band in the VNIR makes it possible to construct digital elevation models from bands 3 and 3b. ASTER swath width is 60km (each scene is 60 x 60km) which makes it useful for regional mapping.
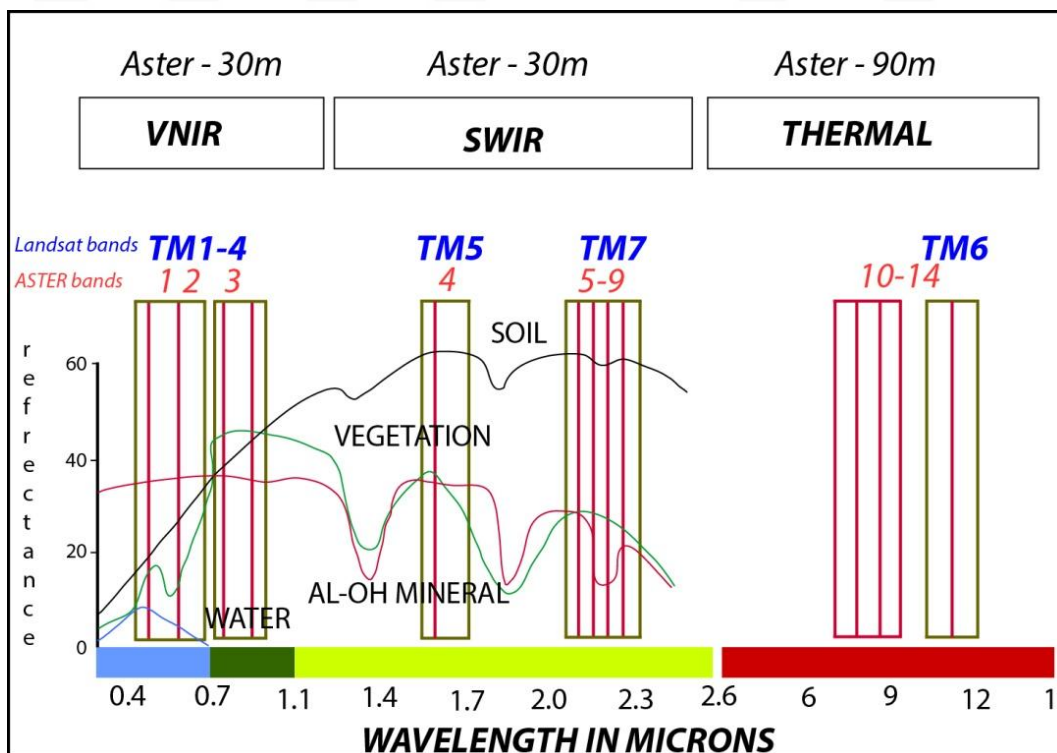
Figure 2.6 : Distribution of ASTER and Landsat channels with respect to the electromagnetic spectrum.

There are a few things to note when using ASTER imagery for regional mineralogical mapping. Firstly, cloud cover, vegetation, and atmospheric effects can severely mask or alter surface signals. Secondly, bands and band ratios do not indicate the occurrence of a mineral with absolute certainty or with any idea of quantity, so ground truthing and setting appropriate thresholds is essential. Thirdly, every terrain is different, so ratios which work in some areas for a particular mineral or assemblage may not show the same thing elsewhere. As a result of these factors, it is important not to look at ASTER images in isolation from other data. If possible, datasets such as geology and structural maps, geochemistry, PIMA analyses (ground truthing), radiometric, and any other available data should be used in conjunction with ASTER for best results.

Table 2.1 : Performance parameters for the ASTER radiometer (modified after Rowan and Mars, 2003).

ASTER baseline performance requirements					
Subsystem	Bands	Spectral range (μm)	Radiometric resolution	Absolute accuracy (σ)	Spatial resolution
VNIR	1	0.52– 0.60	NEΔρ ≤ 0.5%	≤ ± 4%	15 m
	2	0.63– 0.69			
	3N	0.78– 0.86			
	3B	0.78– 0.86			
SWIR	4	1.600–1.700	NEΔρ ≤ 0.5%	≤ ± 4%	30 m
	5	2.145– 2.185	NEΔρ ≤ 1.3%		
	6	2.185– 2.225	NEΔρ ≤ 1.3%		
	7	2.235– 2.285	NEΔρ ≤ 1.3%		
	8	2.295– 2.365	NEΔρ ≤ 1.0%		
	9	2.360– 2.430	NEΔρ ≤ 1.3%		
TIR	10	8.125– 8.475	NEΔT ≤ 0.3 K	≤ 3 K (200– 240 K)	90 m
	11	8.475– 8.825		≤ 3 K (240– 270 K)	
	12	8.925– 9.275		≤ 3 K (270– 340 K)	
	13	10.25– 10.95		≤ 3 K (340– 370 K)	
	14	10.95– 11.65			
Stereo base-to-height ratio			0.6 (along-track)		
Swath width			60 km		
Total coverage in cross-track direction by pointing			232 km		
Mission life			5 years		
Peak data rate			89.2 Mbps		
Mass			406 kg		
Peak power			726 W		

Band number 3N refers to the nadir pointing view, whereas 3B designates the backward pointing view.

2.2.2 Lansat 8

The Operational Land Imager (OLI) and Thermal Infrared Sensor (TIRS) are instruments onboard the Landsat 8 satellite, which was launched in February of 2013. The satellite collects images of the Earth with a 16-day repeat cycle, referenced to the Worldwide Reference System-2. The satellite's acquisitions are in an 8-day offset to Landsat 7. The approximate scene size is 170 km north-south by 185 km east-west (Table 2.2).

The spectral bands of the OLI sensor, while similar to Landsat 7's ETM+ sensor, provide enhancement from prior Landsat instruments, with the addition of two new spectral bands: a deep blue visible channel (band 1) specifically designed for water resources and coastal zone investigation, and a new infrared channel (band 9) for the detection of cirrus clouds. Two thermal bands (TIRS) capture data with a minimum of 100-meter resolution, but are registered to and delivered with the 30-meter OLI data product. Landsat 8 file sizes are larger than Landsat 7 data, due to additional bands and improved 16-bit data product.

Table 2.2 : Performance parameters for the Landsat 8 radiometer.

OLI baseline performance requirements				
Subsystem	Bands	Spectral range (мm)	Characteristics	Spatial resolution
OLI Multispectral bands	1	0.433–0.453	Ultra Blue (coastal/aerosol)	30 m
	2	0.450–0.515	Blue	
	3	0.525–0.600	Green	
	4	0.630–0.680	Red	
	5	0.845–0.885	Near Infrared (NIR)	
	6	1.560–1.660	Shortwave Infrared (SWIR) 1	
	7	2.100–2.300	Shortwave Infrared (SWIR) 2	
	9	1.360–1.390	Panchromatic Cirrus	
OLI panchromatic band	8	0.500–0.680	Panchromatic	15 m
TIRS Thermal bands	10	10.6–11.2	Thermal Infrared (TIRS) 1	100 m
	11	11.5–12.5	Thermal Infrared (TIRS) 2	
Swath Width			185 km	
Mission life			5 years	
Peak data rate			384: 260.92 Mbps	
Mass			2.071 kg (without instruments)	
Peak power			726 W	

TIRS bands are acquired at 100-meter resolution but are resampled to 30 meters in delivered data product.

2.2.3 Methods and processing

2.2.3.1 Band Ratios

Band rationing techniques are widely used for lithological mapping to enhance the spectral differences between different bands and reduce the shadow effects caused by topography (Gad and kusky, 2007). Therefore, in satellite images, band-ratio combinations and band math are effective in emphasizing spectral characteristics of certain rocks and minerals and hence are more effective in lithological mapping compared to the RGB band combination images (Abdeen et al., 2001; Velosky et al., 2003; Rowan and Mars, 2003; Rowan et al., 2003).

The optimal band selection for ratio images depends on the following parameters:

(1) Spectral properties of the surface material of interest and its abundance relative to other surface cover types (Sabine, 1999).

(2) Optimum index factor, OIF; a statistical approach used to determine the highest ranking of combinations of three channels out of the spectral bands (Chavez et al., 1982).

(3) Selection of the greatest variance bands with the least correlation (Jensen, 1996).

2.2.3.2 Principle and Independent Components

Principal component analysis (PCA) and independent component analysis (ICA) are two multivariate statistical methods that convert a set of observed input correlated variables into independent or uncorrelated components that are combinations of the observed variables

2.2.3.2.1 Principle Component (PC)

Principle component analysis (PCA) method is a technique to reduce the correlation between variables data and commonly produces images with clear boundaries between the different geological units. In addition to the previous definition, PCA is a classic multivariate analysis method that transforms observed multivariate variables into several uncorrelated components ranked according to their variances. Principle component analysis technique takes advantage of the underlying minimum dimensionality of the data sets and offers an opportunity to display a great proportion of the original variance in a single image. In Landsat data, around 80-90% percent of the scene information can be accounted by the first PC band. Any principle

component images could be combined to create a color image by assigning the data the make up each image to separate primary colors.

The aim of PCA is to find a set of linearly uncorrelated components (principal components) which could serve as projections from the original data. The first principal component has the largest possible variance, and each succeeding component, in turn, has the next highest variance possible under the constraint that it must be orthogonal to the preceding components

2.2.3.2. 2 Independent Component (IC)

ICA is a relatively new method that was originally introduced by Jutten and Herault (1986) and elaborated explicitly by Common (1994). ICA transforms observed multivariate variables into several components with maximum independence (or nongaussianity). ICA has been applied in various fields for pattern recognition and anomaly detection, such as image classification (Chen and Zhang, 1999; Lee and Lewicki, 2002), hyperspectral data processing (Nascimento and Dias, 2005), and seismic signal processing (Acernese and Ciaramella, 2003). ICA is a special case of blind source separation (BSS). BSS aims to separate source signals from mixture signals without or with little prior information about the source signals or the mixing process (Cardoso, 1998).

In conclusion, ICA and PCA are two unsupervised methods (Ghahramani, 2004) that can project data on new axes according to data's inherent structure. ICA searches for independent components with nongaussian distributions whereas PCA seeks for uncorrelated components with a ranking of variances. ICA and PCA provide exploratory tools to view the data from another perspective. These types of techniques can provide useful information if used by experienced geologists with a good knowledge of the actual geological problems (Yang and Cheng, 2015).

2.2.3.3 Minimum Noise Fraction (MNF)

The Minimum noise fraction (MNF) is a well-known technique for hyperspectral imagery denoising. It is used to The MNF transformation is used to determine the inherent dimensionality of the data, to segregate noise in the data, and to reduce the computational requirements for subsequent processing. The MNF transformation can be used to partition the data space into two parts: the one associated with large eigenvalues and coherent eigenimages, and the second with near-unity eigenvalues

and noise-dominated images. The noise in the resulting data set has a Gaussian distribution and unit variance. Eigenvalues resulting from the MNF transform describe the intrinsic dimensionality of the data set, i.e., the number of spectral endmembers that account for the majority of the spectral variability in the scene. By using only the coherent portions of the MNF (the highest signal portions) in subsequent processing, most of the noise is separated from the data, thus minimizing the influence of noise on data processing and analysis. (Boardman and Kruse, 1994).

3. TECTONIC GEOMORPHOLOGY OF THE EAST ANATOLIAN FAULT, EASTERN TURKEY

3.1 Introduction

Analysis of drainage systems and landforms along active faults provide important insights into fault evolution and present-day tectonic activity. Numerous field and laboratory studies have been conducted to examine how drainage systems evolve along strike-slip faults, uplifting blocks, and evolving thrusts and folds (Azor et al., 2002; El Hamdouni et al., 2008; Castelltort et al., 2012; Özkaymak and Sözbilir, 2012; Ul-Hadi et al., 2013; Yıldırım, 2014; Tari and Tüysüz, 2015; Topal et al., 2016; Khalifa et al., 2017; Tepe and Sözbilir, 2017).

The distinction between active and inactive faults can be inferred through detailed studies of geomorphic indices, including mountain front sinuosity (S_{mf}), valley floor width to height ratios (V_f), stream length-gradient index (S_L), drainage density (D_d), and hypsometric integral (H_i) (Owen et al., 1999; Keller and DeVecchio, 2013). Studies on tectonic geomorphology, mountain uplift, and drainage development along continental-scale strike-slip faults are scarce (e.g. Michael and Frank, 2013).

The East Anatolian Fault (EAF), a morphologically distinct and seismically active left-lateral strike-slip fault that extends for ~400 km, forming a plate boundary between Arabian and Anatolian in southeast Turkey provides an excellent natural laboratory for the study of continental-scale strike-slip fault systems (Figure 3.1). We examine the tectonic geomorphology along the entire EAF using a number of geomorphic indices to gain insights into the recent evolution of this plate boundary and to expand our understanding of the tectonic geomorphology of continental-scale strike-slip faults. We aim to determine, for example, if there is a direction in fault propagation similar to the NAF (which is from east to west according to Şengör et al., 2014), and to reveal (if present) along strike variation in the fault activity. We analyze the results and discuss their implications for the tectonic evolution of the region.
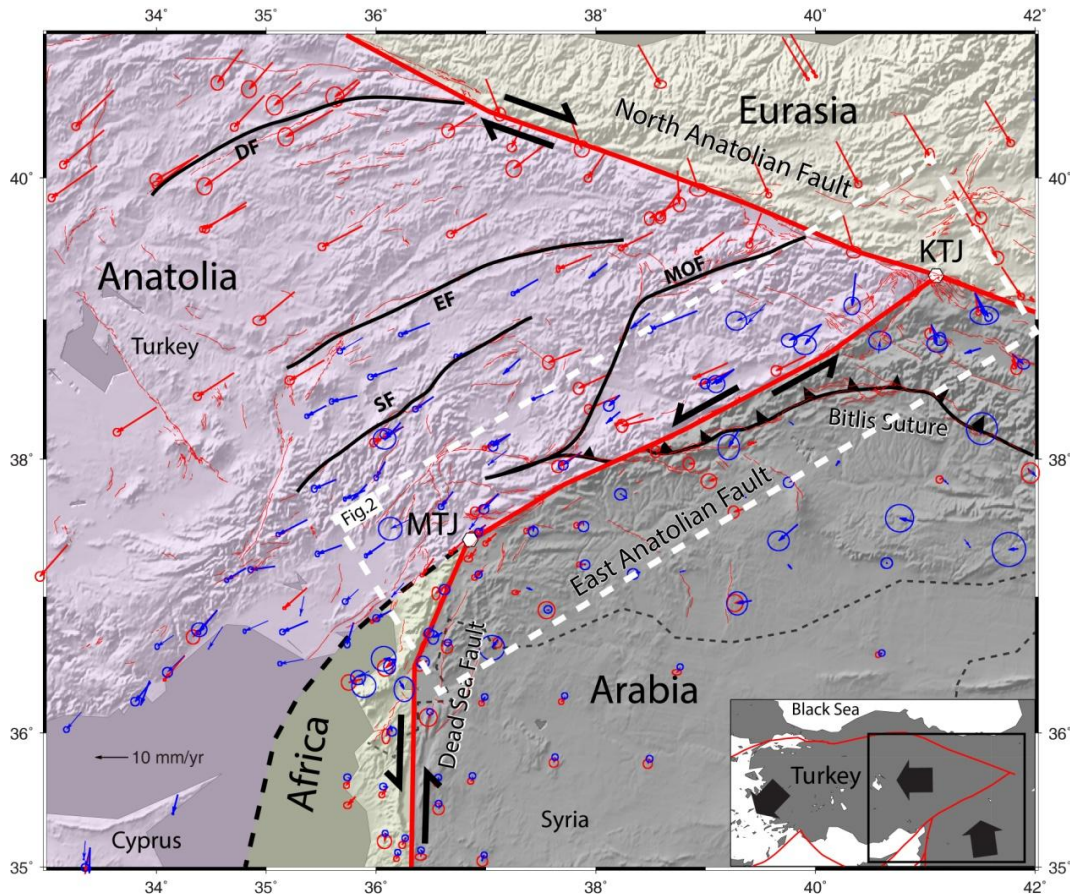
Figure 3.1 : Shaded relief image (data from SRTM-30; Farr et al., 2007) of eastern Turkey showing the African, Arabian, Anatolian and Eurasian plates and major active faults (thick black and red lines). Red and blue arrows indicate GPS velocities with respect to a fixed Arabian plate, with blue and red circles indicate GPS measurements errors, according to Reilinger et al., (2006) and Aktuğ et al., (2016), respectively. *Abbreviations*: MTJ, Maraş triple junction; KTJ, Karliova triple junction; DF, Deliler fault; EF, Ecemiş fault; SF, Savrun fault; MOF, Malatya-Ovacık fault. The inset map and box with white dashed lines show the location of the study area and Figure 3.2, respectively.

3.2 Seismotectonic Setting

The left-lateral strike-slip EAF extends between the Karlıova and Maraş triple junctions and connects the North Anatolian Fault (NAF) and the Dead Sea Fault in southeast Turkey to form the boundary between the Anatolian and Arabian lithospheric plates (Şengör, 1979; Reilinger et al., 2006), (Figure 1). Together with the right-lateral conjugate NAF, the EAF accommodates westward escape of the Anatolian plate from the collisional Arabian / Eurasian plate boundary (McKenzie, 1972; Şengör, 1979). The EAF transform behavior was first recognized and described by Allen (1969) and mapped by Arpat and Şaroğlu (1972). The EAF major significant of the regional active tectonics and seismicity during Quaternary –

Holocene period has been examined by many researchers (Arpat and Şaroğlu, 1975; McKenzie, 1976, 1978; Jackson and McKenzie, 1984; Dewey et al., 1986; Muehlblrger and Gordon, 1987; Westaway, 1994; Westaway and Arger, 1996; Reilinger et al., 2006; Duman and Emre, 2013; Aktuğ et al., 2016; Yönlü et al., 2017). Fault-controlled catchments along the EAF contain Pliocene lignite. The age of the lignite brackets the onset of fault activity to between the late Miocene and earliest Pliocene time, and the exact age of the EAF activity is thus defined by the lignite to be latest Miocene to earliest Pliocene (Hempton, 1985; Şengör et al., 1985; Arpat and Şaroğlu, 1972; Dewey et al., 1986).

Movement of the EAF produces large earthquakes, which seem to occur along the fault every few hundred years in various places, within relatively short paroxysmal periods of large events (Ambraseys, 1988). Recently, the most significant and destructive earthquake occurred on May 22, 1971, near Bingöl with a Mw= 6.6 and focal depth of ~ 10 km (Taymaz et al., 1991).

Recent seismicity has been studied by Bulut et al. (2012) who observed normal and thrust faulting in all segments of EAF and stated that the orientations of the nodal planes of these faults indicate off fault subsidiary fault segments that fit the overall EAF kinematics. They suggested that the corresponding mechanisms of the EAF are compatible with thrust and normal faulting, depending on the trend of the respective earthquakes hypocentres.

3.3 East Anatolian Fault Segmentation

The segmentation of the EAF has been examined so far by many researchers. For example, Hempton et al., (1981) classified the EAF into 5 segments according to the variations in trend and geometry of the fault. Barka and Kadinsky-Code (1988) suggested 14 segments between Karlıova and Türkoğlu according to the geometric discontinuous, the surface rupture and the fault zone seismicity. Şaroğlu et al., (1992a) recorded 6 segments due to the fault changes in the strike. Herece (2008) recognized 11 segments of the EAF zone. Duman and Emre (2013) defined the EAF main strand into 13 segments based on fault jogs and abrupt changes in the general fault strike. According to Duman and Emre (2013), the EAF can be divided into five segments between Karlıova and Türkoğlu, which from east to west are named Karlıova (Karlıova–Bingöl), Palu (Palu–Sivrice), Pütürge (Sivrice–Çelikhan),

Erkenek (Çelikhan – Gölbaşı), and Pazarcık (Gölbaşı–Türkoğlu) , which we number in order from segments 1 through 5 (Figures 3.2 and 3.3).
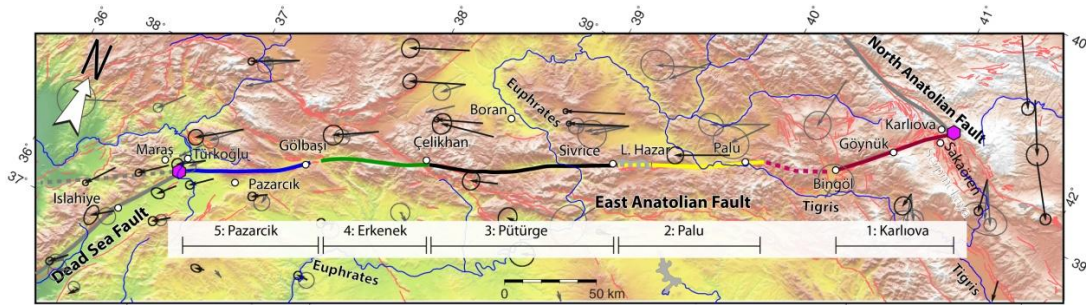
Figure 3.2 : Segmentation of the East Anatolian Fault following Duman and Emre (2013) and the active faults are from Emre et al. (2013). Pink hexagons indicate the location of the Karliova and Maraş triple junctions. Blue lines show the main rivers and streams (e.g., Euphrates River).

Left-lateral faulting features, such as displaced streams, are common along segment 1 (Karlıova). In two areas, north of Sakaören and south of Serpmekaya (Figure 3a), the fault traverses alluvial plains and alluvial fans, and fresh fault scarps are evident along its length (Duman and Emre, 2013). In this segment, streams are left-laterally offsets by several to a few hundred meters (Herece, 2008). This includes a 3.5-m horizontal left-lateral offset at the fault trace recorded by Ambraseys and Jackson (1998) some 1 km southeast of Boncukgöze (Figure 3a). This is probably a surface rupture of the Mw= 7.1, 1866 earthquake. The Karlıova segment contains the Gökdere bend, which is a large right step within the EAF zone that has produced a push-up hill. The eastern and western parts of the step have NE-SW and E-W trending folds, thrusts and strike-slip faults (Duman and Emre, 2013). A series of thrust faults occur in the southern part of the push-up structure (Duman and Emre, 2013).

Segment 2 (Palu) stretches for 77 km. The last historical earthquake on this segment occurred on 3 May 1874 with a Mw= 7.1 (Ambraseyes, 1988; Ambraseyes and Jackson, 1998) (Figure 3b). The human damage was greatest between Lake Hazar and Palu (Ambraseyes, 1988). East of the Lake Hazar, Herece, (2008) reports a 2.6-m lateral offset along the rupture zone, and Duman and Emre (2013) suggest the average displacement of the 1874 earthquake to be 3.5 ± 0.5 m in the central part of the Palu segment. The Lake Hazar basin sits astride the active trace of the EAF, and

the basin is bounded by normal faults to the north and south (Garcia Moreno et al., 2010).
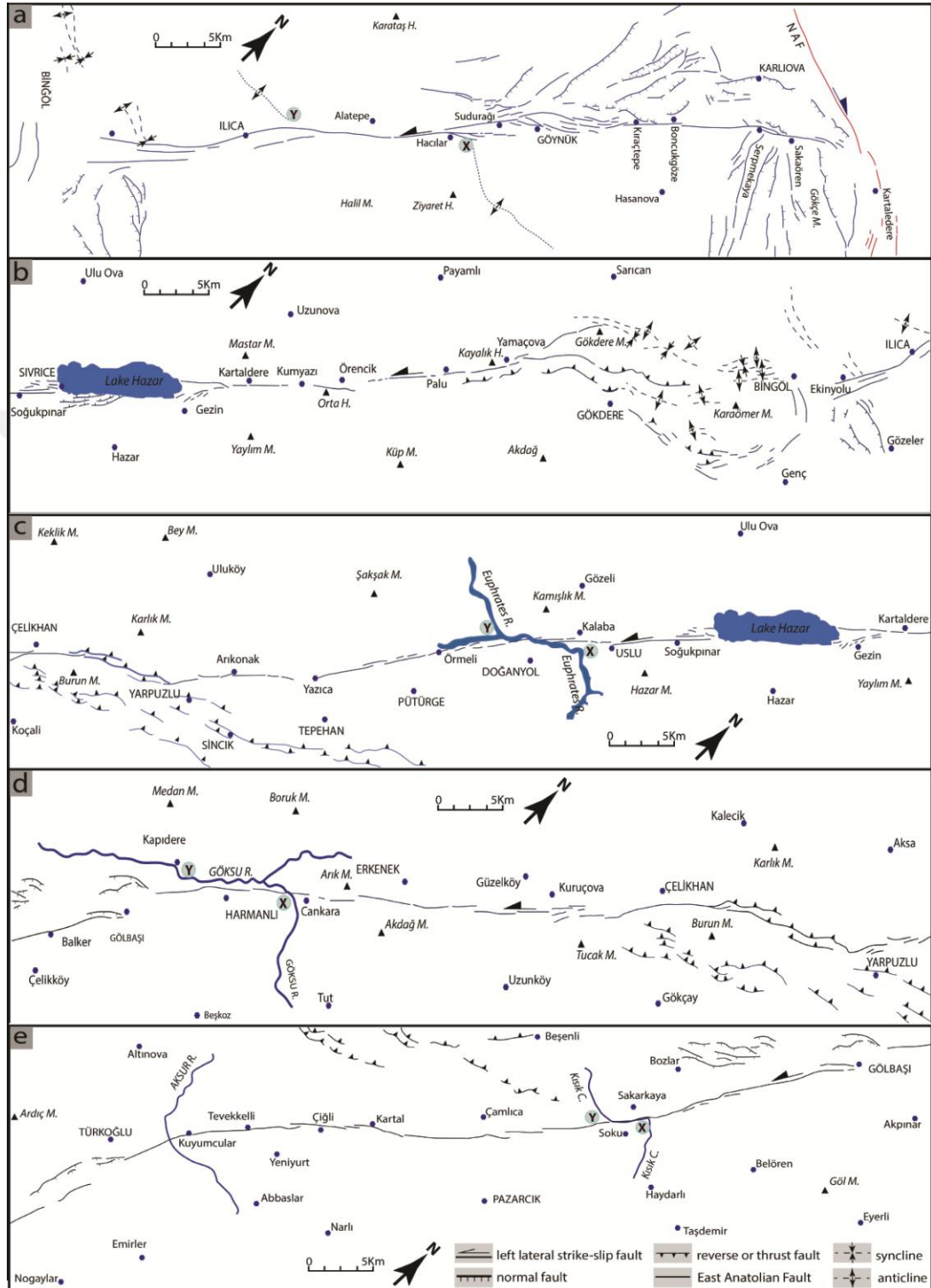
Figure 3.3 : Details of segments 1 through 5 along the EAF. (a) 1. Karlıova, (b) 2. Palu, (c) 3. Pütürge, (d) 4. Erkenek, and (e) 5. Pazarcık segments of the East Anatolian Fault modified after Duman and Emre (2013). Abbreviations: NAF, North Anatolian Fault; M, mountain; H, hill; C, creek; 'x' and 'y' denote piercing points.

The EAF traverses mountains terrain and follows linear valleys along segment 3 (Pütürge; Figure 3c) where it cuts Paleozoic-Mesozoic metamorphic rocks and a Mesozoic ophiolite mélange, as well as volcano-sedimentary rocks (Hempton, 1985; Herece and Akay, 1992; Herece, 2008). Ambraseys (1988) suggests that the 1875 (Mw= 6.8) and 1905 (Mw= 6.9) earthquakes are generated along this segment.

Segment 4 (Erkenek) extends northwards from Lake Gölbaşı. This segment is characterized by late Pleistocene and Holocene left-lateral displaced streams with offsets ranging from several meters to 500 m (Duman and Emre, 2013). One particular stream, the Göksu River, is offset by ~13 km (Şaroğlu et al., 1992a, 1992b) (Figure 3d), which yields a Quaternary slip rate of ~6.5–8.3 mm/yr (Duman and Emre, 2013; Herece, 2008). The northern margin of the Gölbaşı basin is bounded by normal fault sets (3–10 km in length). These normal faults are relatively short, discontinuous, slightly curved and dip to the south trending N72°E within a 3-km-wide zone (Duman and Emre, 2013). Varying geological offsets have been recorded that range from 19 to 26 km in length. Along the Segment 4 of the EAF several fault related basins (e.g. Hazar and Gölbaşı basins) are present, the Gölbaşı basin representing the largest basin along the EAF zone (Yönlü et al., 2013). Yönlü et al. (2013) examine the geology and geomorphology around Gölbaşı basin and argue that there was a wide river valley in which the Aksu River flowed which was later blocked by a landslide about 31.600±500 years ago. They conclude that as a result of this obstacle, the Asku River changed its course and left laterally offsets by the EAF ~16.5±0.5 km, which shows the largest recorded morphological offset along the EAF.

Along segment 5 (Pazarcık) (Yalçın, 1979; Westaway et al., 2006; Hrerce, 2008) (Figure 3e) a Holocene slip rate of 9 mm/yr has been determined using tectonics and GPS measurements (Meghraoui et al., 2006; Karabacak et al., 2011). Based on the paleoseismological data Yönlü et al., (2012) suggest 5±0.5 mm/yr slip rate for Pazarcık segment. Duman and Emre (2013) suggest that the surface ruptures on segment 5 are due to the AD 1114 and 1513 earthquakes. This segment includes the Gölbaşı basin that formed in a releasing step-over and is marked by a 15° change in the dominant strike direction of the EAF.

3.4 Materials and Methods

ArcGIS software and a 30-m resolution digital elevation modal (DEM) extracted from a Shuttle Radar Topography Mission (SRTM) are used for topographic analysis along the entire length of the EAF (Farr et al., 2007). The morphotectonic indexes are applied along the EAF within ~30 km zone on both sides of the Fault trace. The hill-shade option in ArcGIS is used to analyze the mountain front sinuosity. Hydrology and raster calculation tools are used to construct and classify catchments that are greater than fourth-order using the stream order scheme of Strahler's (1952). The catchments, watershed delineation, catchments sizes, and river drainage pattern are extracted from the digital elevation data using algorithms available in hydrology tools within ArcGIS, hydrology toolbox. The catchments are numbered from 1 to 18 from east to west (Figure 4a). The resolution of the DEM limits the degree of uncertainty associated with the geomorphic indices and as in other studies (e.g., El Hamdouni et al., 2008; Tari and Tüysüz, 2015) we do not assign an uncertainty to our geomorphic indices.

3.4.1 Geomorphic indexes

The aim of this chapter is to evaluate the morphotectonic indexes of the fault depending on the rocks strength along the mountain front of the fault deformation zone and recognize the rock resistance based on geological maps, field observations and similar papers (e.g., El Hamdouni et al., 2008; Alipoor et al., 2011; Selçuk, 2016). We consider rock hardness as Selby (1980) did, with strength related to the constituent material and cement assisting in the resistance to weathering and erosion processing. Rock strength is classified from very low (silt, sand, marl, alluvium, limestone), low (conglomerate, sandstone, shale with interbedded limestone), medium (sandy limestone), high (basalt), and very high (gneiss, schist, gabbro, marble, quartzite). Mountain front sinuosity (Smf) values were calculated for 18 mountain fronts along the 5 segments of the EAF from SRTM 30-m pixel-resolution DEM. Smf values approaching 1 suggest a more active tectonic setting. Valley width to height ratio (Vf) values were determined for 77 streams aligned along the mountain fronts of the EAF. Stream length-gradient index (S_L) values were calculated every 100 m along the length of the main stream channels of the EAF.

Basin asymmetry factor (A_F), drainage density (D_d), and the hypsometric analysis were examined for the 18 catchments along the EAF(see chapter 2 for more details).

3.5 Results

3.5.1 Rock strength

The mountain front along the Fault zone consists of large varieties of geological rock types. Presence of basalt, volcanic rocks, gabbro-diabase, carbonate rocks, marble, gneiss and schist, neritic limestone, and undifferentiated quaternary rocks (Figures 3.5a and 3.5b) along the fault implies the presence of all levels of rock strengths. Thus, areal coverage of the catchments is kept quite large (Figure 3.5b) so that they encompass a variety of rock types with different resistance to erosion. This in turn, minimizes the effect of lithology on morphometric indices calculated. Very high and low strength rocks mostly are exposed along segment 3. Segments 1 and 4 cover high and moderate rock strengths. The mountain fronts along segments1, 2 and 5 are made up of moderate, low and very low strength of rocks. In the central part of the EAF, segments 3 and 4 comprise rocks with high rock strengths.

3.5.2 Mountain front sinuosity (S_{mf})

In this chapter, 18 mountain fronts are examined (Figure 3.4; Table 3.1). The five segments from east to west record S_{mf} Values range from 1.07 to 1.17, 1.05 to 1.46, 1.06 to 1.09, 1.01 to 1.09, and 1.07 to 1.28, respectively. The lowest S_{mf} values are associated with segments 3 and 4, while the highest values are calculated for segment 2. The S_{mf} values show that each segment reflects topographic signals of active uplift and there is no inactive fault segment along the study fault. Depending on the S_{mf} values, there is no obvious activity trend along the EAF

3.5.3 Valley width to valley height ratio (Vf)

The V_f index is calculated for the main valleys and streams that cross and run parallel to the mountain fronts of the studied zone (Figure 3.4). Actually, values of V_f index vary depending on rock type, stream discharge, and catchments sizes. So, V_f values should be compared for the similar geological condition. Mean V_f values range from 0.47 to 0.75, 0.61 to 1.32, 0.24 to 0.61, 0.11 to 0.37, and 0.54 to 0.80 for the five segments from east to west, respectively (Figure 3.4; Table 3.1). The lowest mean values are calculated from segments 4, while the highest values come from segment 2. The results suggest a general similarity between S_{mf} and mean V_f values of the five

segments. The V_f values consistency with the S_{mf} might give a good signal to evaluate the tectonic activity of the segments.
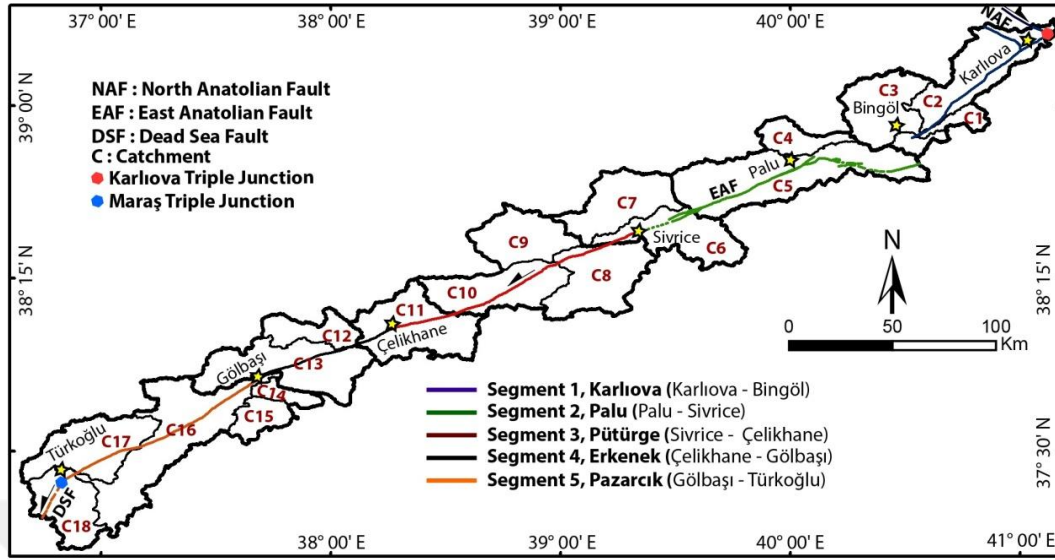
Figure 3.4 : (a) Studied catchments along the EAF. Karlıova, Palu, Pütürge, Erkenek, and Pazarcık segments.

Table 3.1 : Values of the mountain front sinuosity and valley floor width to height ratio of measurements (see locations in Figure 3.5).

Mountain Front	S_{mf}	V_f (mean)
S1a	1.08	0.74
S1b	1.17	0.75
S1c	1.07	0.47
S1d	1.13	0.65
S2a	1.39	0.61
S2b	1.44	1.32
S2c	1.46	0.64
S2d	1.05	0.64
S3a	1.08	0.30
S3b	1.09	0.61
S3c	1.06	0.24
S4a	1.09	0.11
S4b	1.01	0.21
S4c	1.03	0.14
S5a	1.28	0.80
S5b	1.15	0.54
S5c	1.07	0.75
S5d	1.08	0.67
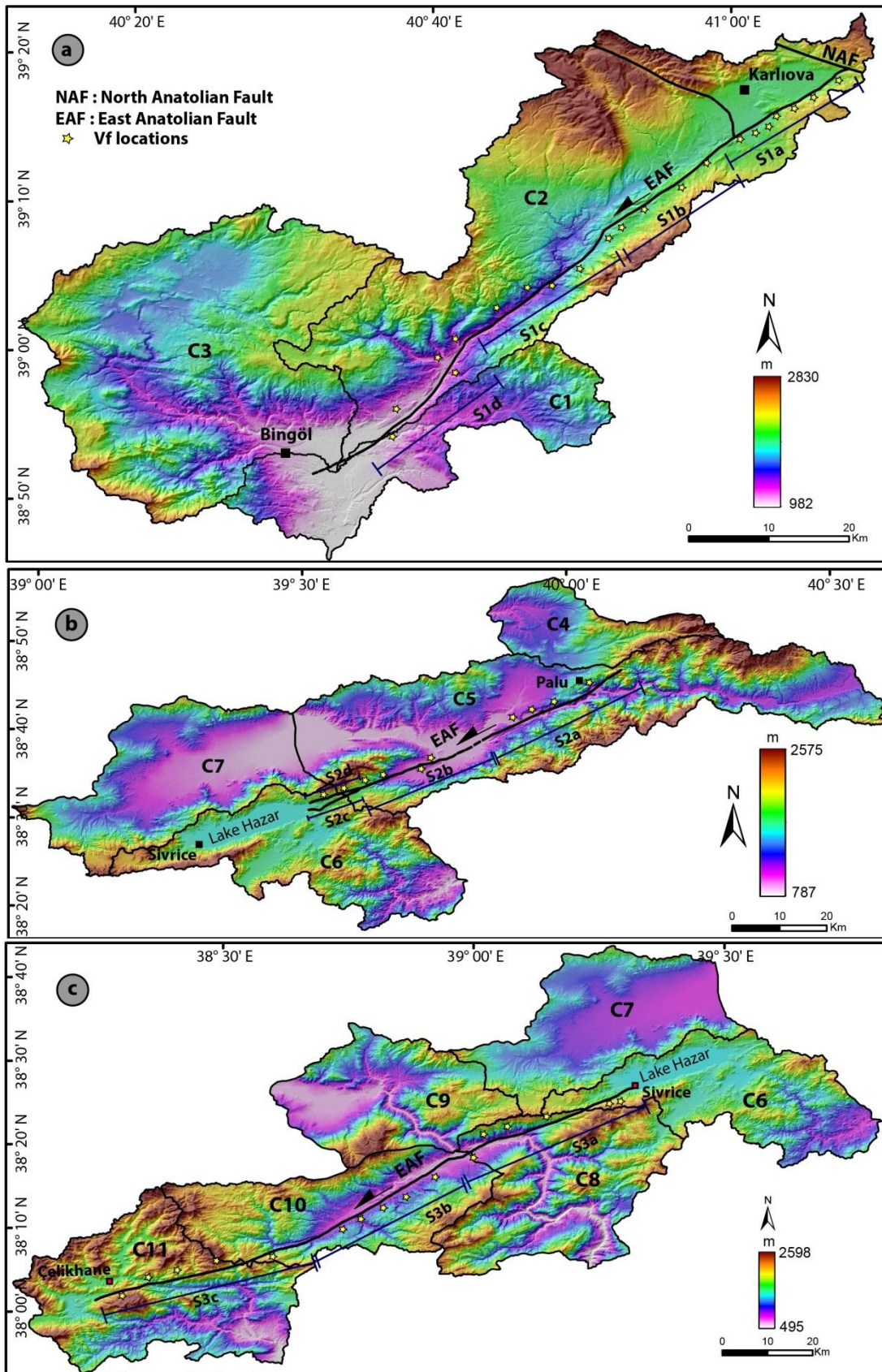
Figure 3.5 : Karlıova (a), Palu (b), Pütürge (c) segments on top of colored shaded elevation image.
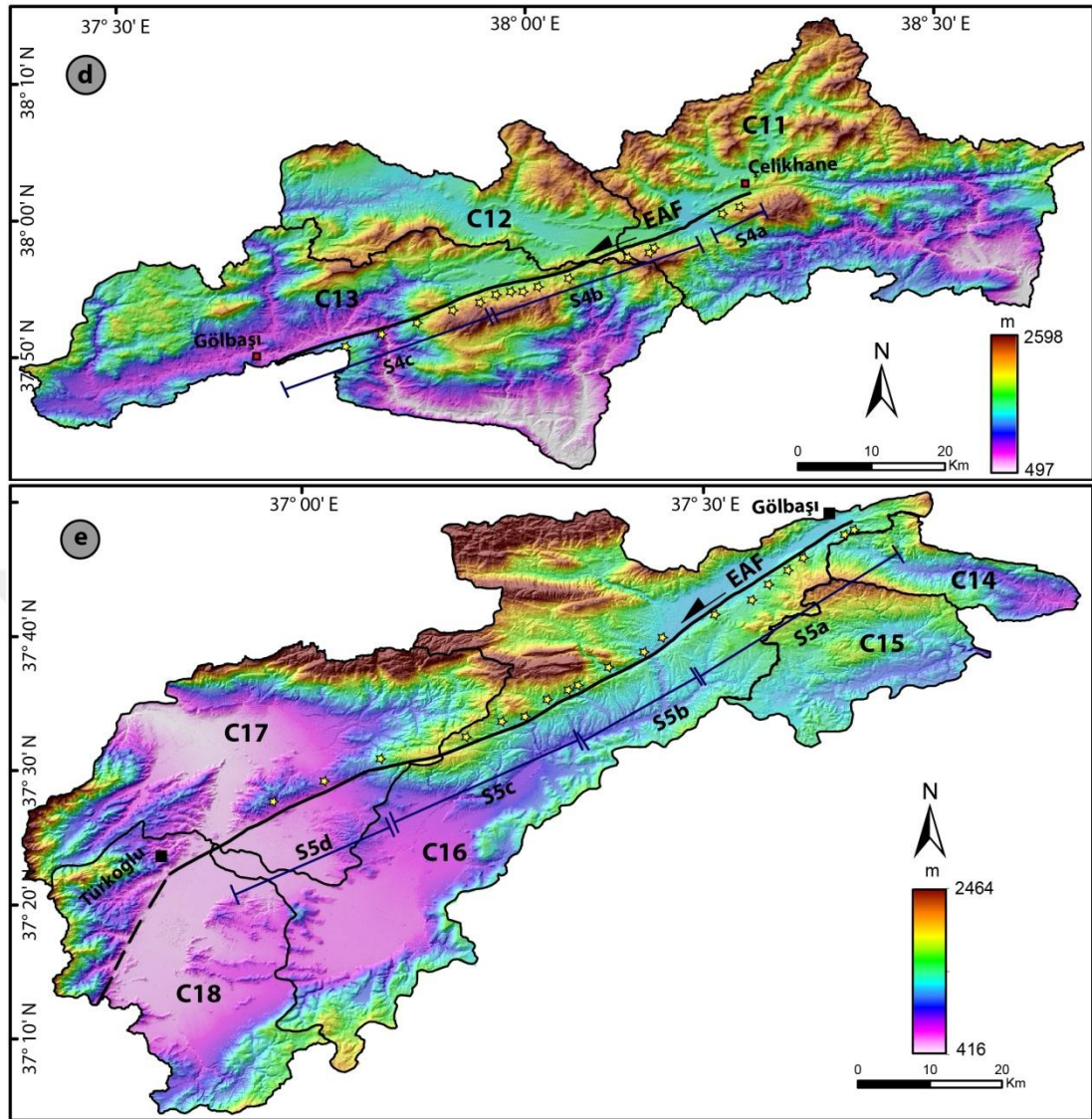
Figure 3.5 : (Continued) Erkenek (d) and Pazarcık (e) segments on top of colored shaded elevation image.

According to According to the S_L index linked to rock resistance, climate and final SL map, the S_L index values over the study area range from 50 to 350 along the stream channels of the fault zone (Figure 3.5b). The lowest index values are found along the upstream reaches of the drainage catchments while the heights values are located across the mountain fronts. The S_L values show some low values when flowing parallel to the valleys that produced by the fault. The S_L map shows that values are increasing toward the mountain fronts (Figure 3.5b). The heights values of the index are recorded also in most catchments that are not associated with particularly resistant rocks. The anomalous values of the S_L index are noticed along the five segments.

3.5.4 Basin asymmetry factor (A_F)

The A_F-50 values shown in Table 2 and range from 1.88 to 26.25, which indicate the differences between the observed value of the 50 and neutral value. The results show that catchments 7, 4 and 17 have values close to 50 and the catchments that have the highest values away from 50 are 2 and 15 (Table 3.2). Within the study area, the relative tectonic activity of class 1 is recorded for catchments 2, 8, 9, 11, 13, 15, and 16 as examined by A_F index classes; catchments 3, 6, 10, 12, 14 and 18 show class 2 of relative tectonic activity; and relative tectonic activity class 3 is measured for catchments 1, 4, 5, 7, and 17 (Table 3.2).

3.5.5 Drainage density (D_d)

Drainage densities vary from 3.5 to 5.6 km/km² (Table 3.2). The highest drainage density is for catchment 4 while the lowest values are recorded for catchments 11 and 13. The catchments, in general, have a remarkably low drainage density, and most drainages reflect youthfulness of the catchment dissection. The average drainage density of the catchments is low in segments 3 and 4.

3.5.6 Hypsometry (H_i)

Over the study region, H_i values range from 0.25 to 0.58 (Table 3.2). High values of the H_i-index are recorded for catchments 8 and 7, which generally indicate that not as much of the uplands have been eroded, and suggest younger catchments and landscape, most probably created under active tectonics conditions. Catchment 2 records the lowest value of Hi that is due to relatively older landscape with more erosion and less subjected by recent active uplifting. In our study area, the results of the hypsometric index tend to suggest that the middle part of the EAF is slightly more active than the rest of the fault and has the youngest catchments, albeit only slightly younger. Similarly, H_i curves recorded (1) convex curves in catchments 11, 12, 13, and 16, (2) concave-convex or slight curves in catchments 1, 2, 3, 5, 6, 7, 9, 10, 14, 15, 17, and 18, and (3) concave curves for catchments 2 and 5 (Figure 7a, 7b, and 7c).

Table 3.2 : Asymmetry Factor (AF), Drainage Density (Dd), Hypsometric Integral (Hi) of the different catchments of the study area.

Catchments	A_F	A_F-50	A_F (Class)	D_d	H_i
C1	44.76	-05.24	3	4.1	0.45
C2	76.25	26.25	1	4.5	0.48
C3	59.93	09.93	2	4.7	0.47
C4	47.73	-02.27	3	5.6	0.27
C5	54.29	04.29	3	4.9	0.33
C6	57.82	07.82	2	4.8	0.36
C7	48.12	-01.88	3	4.6	0.25
C8	66.83	16.83	1	4.2	0.54
C9	67.88	17.88	1	3.9	0.45
C10	58.67	08.67	2	4.1	0.48
C11	66.39	16.39	1	3.5	0.56
C12	44.14	-05.86	2	4.3	0.51
C13	28.04	-21.96	1	3.8	0.58
C14	59.90	09.90	2	5.0	0.41
C15	70.00	20.00	1	4.9	0.45
C16	32.28	-17.72	1	4.3	0.53
C17	53.80	03.80	3	4.1	0.40
C18	37.85	-12.15	2	4.0	0.46

3.5.7 Average of the geomorphic indices

The mean S_{mf}, V_f, and D_d values recorded the lowest values in segment 4, 3, 1, 5, and 2 respectively (Table 3.3). Mean A_F levels analysis shows level 1 of relative tectonic activity for segment 3 and 4, level 2 of relative tectonic activity for segments 1 and 5, and relative tectonic activity level 4 for segment 2 (Table 3). H_i values are examined to record the highest value in segment 4, 3, 5, 1, and 2 respectively (Table 3.3).

Table 3.3 : Mean morphometric parameters of the studied segments and catchments.

Segments	S_{mf}	V_f	Catchments	Mean A_F (Class)	A_F Activity degree	Mean D_d	Mean H_i
Segment 1	1.11	0.67	C1, C2, and C3	2.00	2	4.43	0.46
Segment 2	1.34	0.75	C4, C5, C6, and C7	2.75	4	4.97	0.31
Segment 3	1.07	0.38	C6, C8, C9, C10 and C11	1.40	1	4.12	0.48
Segment 4	1.04	0.21	C11, C12, and C13	1.30	1	3.86	0.55
Segment 5	1.15	0.74	C14, C15, C16, C17, and C18	1.80	2	4.47	0.45
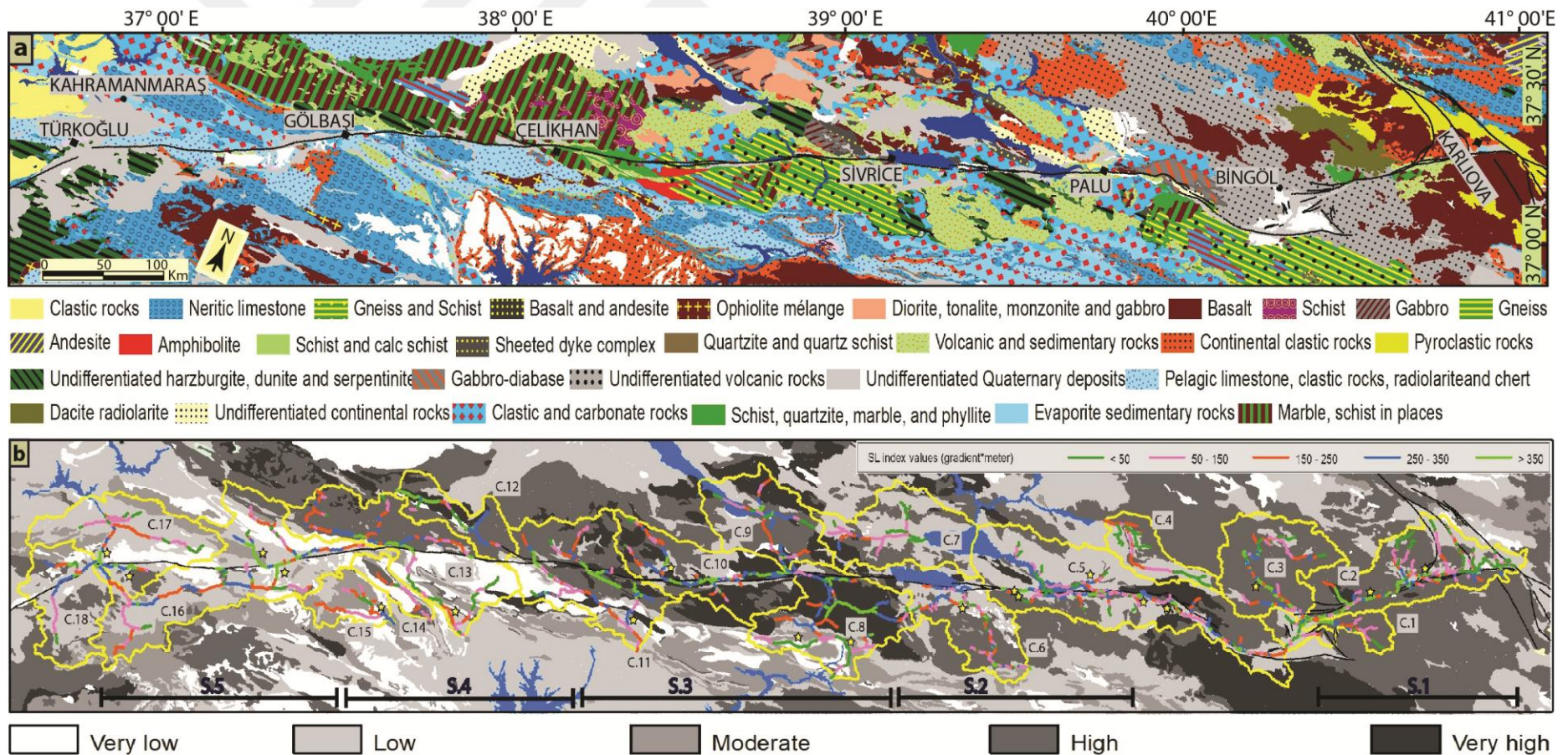
Figure 3.6 : Geological map of the EAF (extracted from geological maps catalogue of the General Directorate of Mineral Research and Exploration of Turkey), (b) SL index along the channels and rock strength level (according to El Hamdouni, 2008) of the studied fault. Yellow stars indicate the distribution of the SL index anomalies.
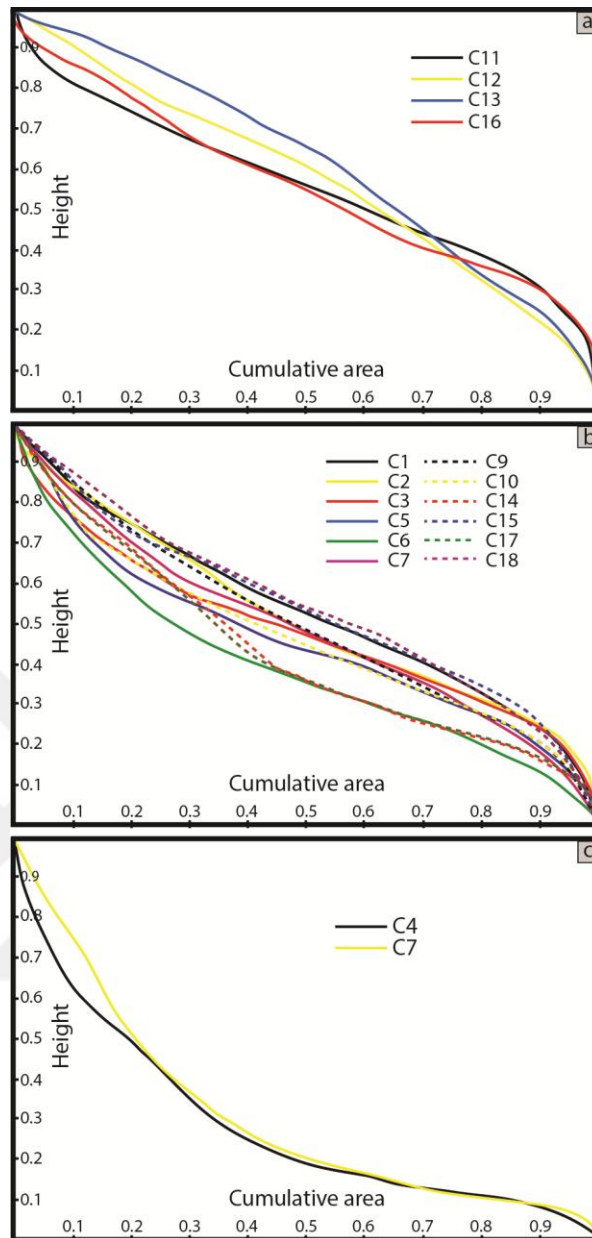
Figure 3.7 : Hypsometry curves of 18 catchments along EAF shown in Figure 3.4. (a) Convex hypsometric catchments (weakly eroded catchments), (b) Convex - Concave hypsometric catchments (moderately eroded catchments), and (c) Concave hypsometric catchments highly eroded catchments).

3.6 Discussion

3.6.1 Relative tectonic activity based on geomorphic indexes

Many studies have been used the combination of indices Smf and Vf to present a preliminary overview of the relative tectonic activity of the fault mountain fronts (Bull and McFadden, 1977; Silva et al., 2003; Yıldırım, 2014). In our study, there is a general uniformity between Smf values and Vf mean values of the five fault

segments along the EAF. Our Smf values suggest that all fault segments are young and active along the fault and that each segment is likely undergoing tectonic uplift. The highest value of Smf (low tectonic activity) is associated with segment 2, while the lowest values are for segments 4 and 3 (high tectonic activity), which indicate a straighter mountain front than the others. The highest degree of tectonic uplift occurs in segment 4 and is consistent with the view of Yönlü et al. (2013) that discuss the presence of the largest morphological offset of the EAF along the same segment.

Along the study fault, Vf values suggest continued and comparatively high uplift rates. Lower values, in the central valleys, suggest a higher uplift and incision rate than in the southern and northern parts of the EAF. Keller and Pinter (2002) suggest that Smf values of 1.0–1.6 are indicative of active range-bounding fault zones. Some studies (e.g. Bull and McFadden (1977); Rockwell et al. (1984)) suggest that a diagram for the Vf and Smf values can be plotted to illustrate the distribution of these values along streams and mountain fronts, and to classify relative tectonic activity into 3 classes. Smf versus Vf plots show that all segments are indicative of the highest tectonic activity, i.e., Class I, (Figure 3.6). Class 1 is commonly associated with uplift rates between 0.05 and 0.5 mm/yr (e.g., Rockwell et al., 1984; Yıldırım, 2014).

Although all the EAF segments are plotted as a higher activity class, they record differences in relative tectonic activity values. They are arranged from high to low as segment 4, 3, 1, 5, and 2. The results show slight differences and nearly uniform values of S_{mf} along the entire fault, implying that tectonic activity along the whole EAF zone is nearly similar. This is also consistent with the published uniform slip rate (~10 mm/yr) along the whole EAF based on the GPS measurements (Reilinger et al., 2006; Mahmoud et al., 2013; Aktuğ et al., 2016).

The SL values over the study zone, calculated from digital elevation modal and Geographic Information System (GIS) software are shown in Figure 5a and 5b, which illustrate the relationship between SL values and the underlying geology. Over most of the studied rivers, the SL values increase abruptly in the same rock strength (Figure 3.5b) except rivers over catchment 5 that is located along segments 2. Over this catchment the rocks strength changes alternately from the very low to moderate where SL values of catchment streams increase.
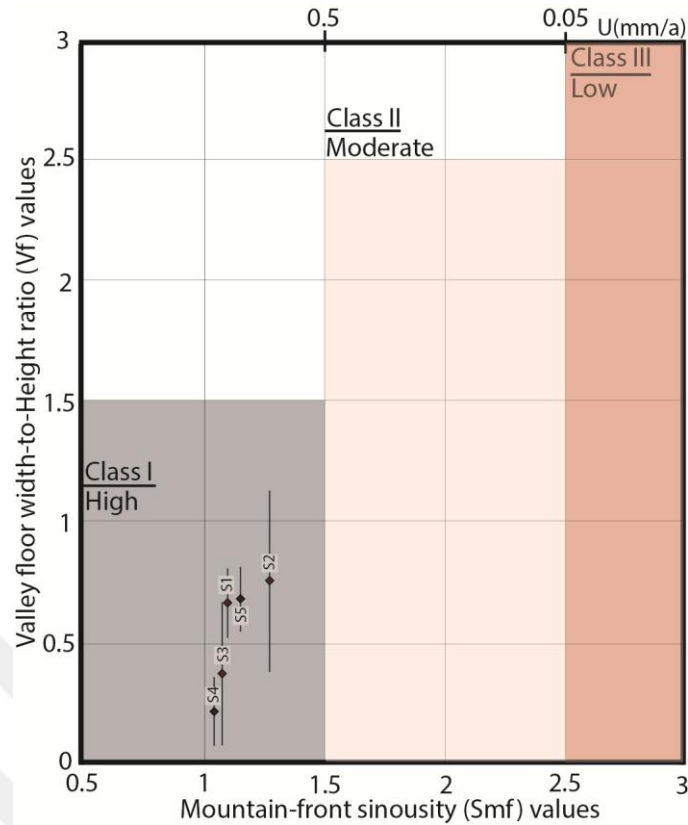
Figure 3.8 : Plot of S_{mf} versus V_f for the mountain fronts of each segment and inferred activity classes. Vertical bars show the standard deviation for V_f values. Numbers at the top indicate inferred uplift rates U (mm/year) from Rockwell et al. (1984).

In such a case, Yıldırım (2014) argues that the effect of the rock strength is small on the increase of values of S_L in the same rock strength along the rivers. El Homdouni et al., (2008), Alipoor et al., (2011), and Azañón et al., (2012) present anomalous values of the S_L index for the high S_L values that are not associated with resistance rocks and they are interpreted these anomalous as tectonic signals. Within our study zone, anomalous measurements are recorded along nearly all segments which reflect high uplifting activities. The S_L results are also greater on both sides of the fault, indicating recent and continued uplift of the EAF. Regarding to the impact of the geology, we recorded an abrupt increasing of S_L values in the same rock strength and many anomalies locations along all segments that reflect tectonic signals rather than the effect of geology. In addition to the previous remarks, we found that nearly all catchments have the same verities of rock strength types. Depending on these conditions, we assume that the impact of the geology is a negligible and tectonic impact is prevailing. Also, because of (1) S_L index are generally affected by both rock strength and climate, (2) drainage development and local geomorphology are

affected by the tectonic uplifting and region deformation, in addition to rock resistance that are the prevailing factors in southeastern Turkey, (3) uniformity of the climate along the fault zone, and (4) climate index contribute the erosion in areas where sedimentary rocks particularly comprise local bedrock, we claim that the climate does not have high significant impact on the studied deformation zone.

The A_F index mostly applied over a relatively large area (Hare and Grander, 1985; Keller and Printer, 2002). This factor is sensitive to change in inclination perpendicular to the channel direction (El Hamdouni et al., 2008). Structural control of the bedding orientation may play a great role in the development of basin asymmetry (Alipoor et al., 2011). Except the catchments 1, 4, 5, 7 and 17 (tectonically more stable), the A_F values for all catchments indicate tilting and relative active tilting/uplifting. Note that the catchments 2, 5, and 12 are among the deformation studied zone but they are away from the EAF trace. According to El Hamdouni (2008), the mean values of A_F recognize the segment 3 and 4 as the same zone of relative tectonic uplifting that reflects the highest tectonic activity, segments 1 and 5 as the second level of uplifting, and the lowest level that records for only segment 2.

Values of D_d based on the degree of which drainage development has dissected structural landform (Melosh and Keller, 2013). Topal et al., (2016) assume that the low drainage density characterizes the drainage that appears nearly straight and steep channels that offer catchments with recent movement activity. The highest D_d values are recorded to catchments 4, 5, 14, and 15 which are located close to the fault trace and give less tectonic uplifting than the others. Overall, segments 4 has the lowest D_d value that reflects relatively higher uplifting activities than in segments 2 that shows the highest D_d value. The hypsometric integral index does not relate directly to relative active tectonics (El Hamdouni et al., 2008). This factor values are affected by the rock strength as S_L index (El Hamdouni et al., 2008). H_i-index records highest tectonic uplifting rate with convex curves of the catchments along segments 3 and 4, and shows low rate of tectonic uplifting (concave curves) just in catchments 4 and 7 which are located away from the fault trace (Figure 3.7; Table 3.2).

Average values of Hi show that high to low values are recording in segments 4, 3, 1, 5, and 2 respectively (Table 3.3). The results are suggesting that all the catchments

along segments 4 and 3 are young and relatively reflecting high rate of uplifting in compare to the other segments.

In conclusion, all the geomorphic indices of the studied fault zone suggest that all the segments along EAF are highly active (Class 1) and have nearly similar significant uplift rate. The catchments that are away from the EAF show intermediate to low degree of tectonic activity and that reflects the rate of uplifting, and tectonic is increasing toward the fault trace.

3.6.2 Implications of long-term deformation patterns

The EAF accommodates most of the relative movement of the Arabian and Anatolian plates (Duman and Emre, 2013). Variations of the S_{mf}, V_f, (Figures 3.6 and 3.8c), and values of the S_L, (A_F, D_d, and H_i (Table 3.3)) provide a means to help examine the variation of tectonic uplifting activity along the fault (Yıldırım, 2014). All segments along the EAF have slightly different trends (Duman and Emre, 2013).

Values for all geomorphic indices along the fault are different but they are in the same activity zone (Figures 3.8c, 3.8d, and 3.8e), implying that all the segments have comparable tectonic activity and have undergone similar amounts of erosion over time. The uniform variation in geomorphic indices might also indicate that either all the fault segments initiated at the same time and underwent similar morphological evolution or some fault segments formed later, but experienced higher erosional rates. The former possibility appears to be more likely when one considers the relatively uniform total offset of about 13–30 km and the uniform and constant slip rate of ~10 mm/yr (Reilinger et al., 2006; Mahmoud et al., 2013; Aktuğ et al., 2016) along the entire fault. In contrast, the cumulative offsets along the NAF become smaller and the width of the shear zone gets wider from east to west (Şengör et al., 2014). This is because the NAF becomes younger westward as it has propagated from east to west at a rate of ~ 11 cm/yr (Şengör et al., 2004).

Dewey et al. (1986) suggest that the EAF is a root of the distributed deformation and is oblique to their assumed Anatolian/Arabian plate motion, so this interpretation indicates that the EAF is not a true transform fault.

On the On the other hand, Westaway (1994a) concludes that the Anatolian/Arabian plate boundary is a real transform fault system since it initiated at ~5 Ma.
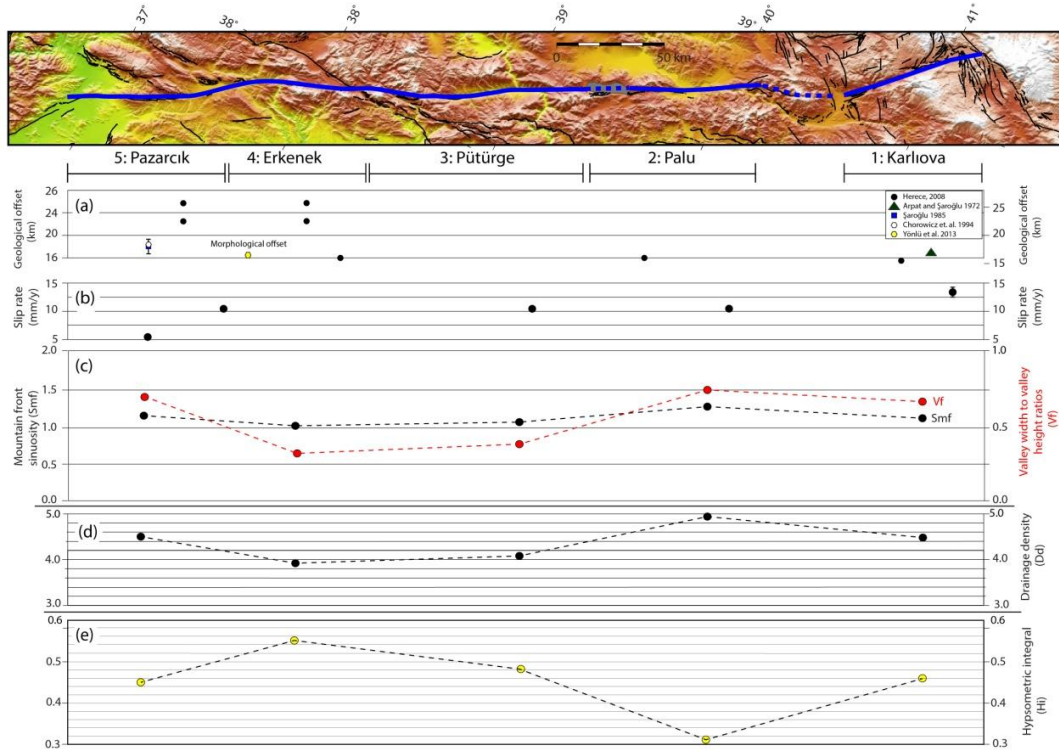
Figure 3.9 : Geological offsets (a), slip rates (b), and Morphometric indices (c–e) along the East Anatolian Fault. S_{mf}, Mountain front sinuosity; V_f, valley width to valley height ratios; (D_d) drainage density; H_i, hypsometric integral.

He argues that since ~5 Ma the Malatya-Ovacık Fault zone, which is subparallel to the EAF zone, has taken up part of the Anatolian/Arabian plate movement. Arger et al. (1996) and Westaway and Arger (1996) recorded evidence that the Malatya-Ovacık Fault is inactive at present, and proposed instead a scheme where the Anatolian/Arabian plate boundary formed by Malatya-Ovacık Fault from ~5 to 3 Ma, and the EAF zone has created this boundary since ~3 Ma (Figure 9). Westaway, (1994) argues that the Malatya-Ovacık Fault and EAF are tectonically equivalent, and both have taken up the ~70 km of estimated Anatolian/Arabian since ~5 Ma. In opposite of this, Westaway and Arger, (1996) argue that the Malatya-Ovacık Fault zone create the African/Anatolian plate boundary since 3-5 Ma and no significant slip recorded since this time. Westaway and Arger, (2001) explain the reasoning of this idea as following; (1) based on the lack of recorded seismicity Jackson and Mckenzie (1984) claim that the Malatya-Ovacık Fault is not active anymore, (2) the field work of Westaway and Arger (1996) does not show any geomorphological estimate for recent slip, and (3) if the western and eastern of Erzincan and the Malatya-Ovacık Fault zone are active at the same time, very intense deformation would be recorded around their intersection region. Because of the previous reasons,

Westaway and Arger (1996) conclude that the Malatya-Ovacık Fault zone was the Anatolian/Arabian pale boundary at ~5 Ma and later, this boundary moved southeast to occupy its modern location. They dated this second story to ~3 Ma. On the other side, some researchers (e.g. Koçyiğit and Beyhan (1998) and Kaymakcı, et al., (2006)) suggested a different hypothesis about the Malatya - Ovacık Fault zone activity. They argued that the Malatya-Ovacık Fault is tectonically active at present and its a part of the present motion between the Anatolian/Arabian plates. Westaway and Arger (2001) criticise the Koçyiğit and Beyhan (1998)'s idea because they did not offer any quantitative examinations of the kinematics of the Malatya-Ovacık Fault in order to support their different scenarios. As discussed above, our morphometric suggests a coeval development along the different segments of the EAF supports the view of an eastward jump of the proto-EAF (~110 km) from what is now the Malatya-Ovacık Fault zone to its present-day EAF at ~3 Ma (Figure 9; (Arger et al., 1996; Huber-Ferrari et al, 2009)). Westaway (1994a) calculates a 14±2 mm/ an of convergence rate for the Anatolian/Arabian plate, which since initiation of slip on the EAF zone accommodated ~30 km of convergence, with all the 14±2 mm/a slip occurring on the Malatya-Ovacık Fault zone. Before this time, the NAF zone ended at Erzincan and its present eastern part did not exist (Figure 3.9).
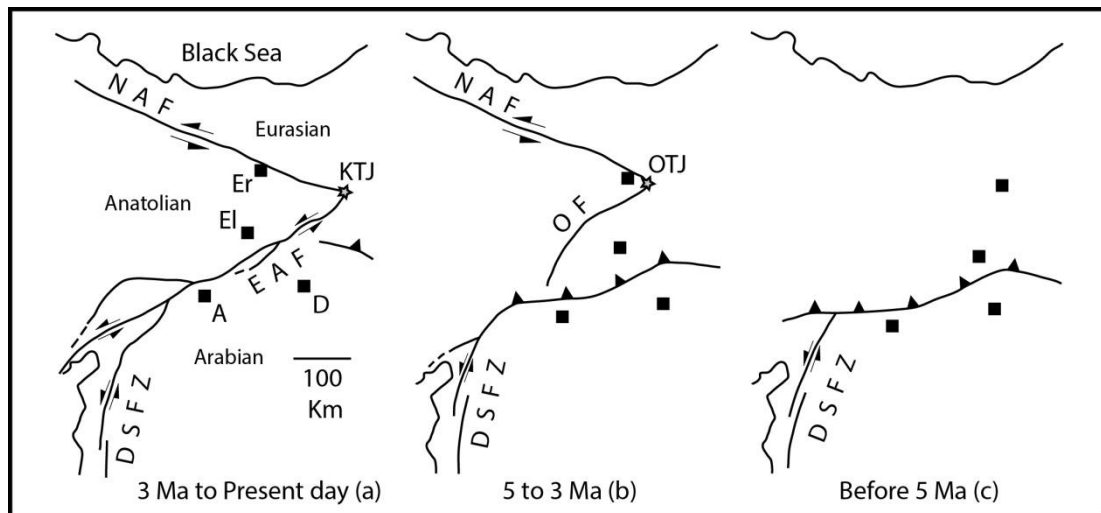
Figure 3.10 : Summary of the evolution of the triple junction between the Arabian, Eurasian and Anatolian plates (from Arger et al., 1996; Westaway and Arger, 1996, 2001; Huber-Ferrari et al., 2009). OTJ, Ovacik triple junction; KTJ, Karlıova triple junction; OF, Ovacık Fault; Er, Erzincan; El, Elazığ; D, Diyarbakır; A, Adıyaman. (a) Present day. (b) Immediately before the modern fault geometry developed between 3 and 5 Ma. (c) Immediately before to change in plate geometry at 5 Ma.

3.7 Conclusions

In this chapter, geomorphic indices including S_{mf}, V_f, S_L, A_F, D_d, and H_i are used for the first time along the EAF to gain deeper insights into morphotectonic evolution and activity of the EAF. S_{mf} versus V_f relationship shows symmetry in values that indicate there is a positive correlation between them, and a high degree of tectonic and geomorphic activity, supported by the results from a stream gradient analysis and hypsometric analysis. This implies that each segment along the fault is presently very active.

The nearly uniform range of geomorphic indices along the entire length of the fault suggests that development of the EAF was essentially coeval along its length, supporting the view that the present day Anatolian/Arabian plate boundary, i.e., the EAF, jumped eastward from the Malatya-Ovacık Fault zone from the proto-EAF to its present day location at ~3 Ma. This is in good agreement with the nearly uniform geological offsets and the present day slip rate of ~10 mm/yr along the entire fault that appears to be constant since ~3 Ma.

This study illustrates that morphometric analysis along the entire length of a major strike-slip fault provides important insights into a fault's tectonic evolution. Calculations of all catchments geomorphic indices and indexes that are related to the trace of the faults can provide us with valuable data on the tectonic behaviors and landscape evolution. Thus, this can be applied to other major faults elsewhere, especially to those whose tectonic activity, cumulative offset and slip rates are not well defined.

4. ASTER SPECTRAL BAND RATIOS FOR LITHOLOGICAL MAPPING: A CASE STUDY FOR MEASURING GEOLOGICAL OFFSET ALONG THE ERKENEK SEGMENT OF THE EAST ANATOLIAN FAULT ZONE, TURKEY

4.1 Introduction

The sinistral East Anatolian Fault (EAF) extends for about 400 km between Karlıova Triple Junction in the northeast and Maraş Triple Junction in the southwest, characterizing the boundary between the Anatolian and Arabian plates in eastern Turkey (Mckenzie, 1970; Şengör et al., 1985) (Figure 4.1). The age of the EAF is suggested to be the latest Miocene–earliest Pliocene (Hempton, 1985; Şengör et al., 1985; Dewey et al., 1986). Depending on the detailed geological mapping along the EAF, the offsets on the pre-Miocene rocks are measured between 14 and 26 km (Herece, 2008; Hubert-Ferrari et al., 2009; Duman and Emre, 2013). In terms of the recent activity of this fault zone, the GPS-based geodetic models and paleoseismological studies yield a slip rate of about 10 mm/yr (Meghraoui et al., 2006; Reilinger et al., 2006; Aktuğ et al., 2016).

The EAF is divided by Duman and Emre (2003) into five segments, which from east to west are called Karlıova, Palu, Pütürge, Erkenek, and Pazarcık, respectively (Figure 4.2). The Erkenek Segment is a 62-km long geometric fragment of the EAF, which is delimited from the Pütürge Segment with a restraining double bend at Çelikhan and from the Pazarcık Segment with a releasing step-over at Gölbaşı (Duman and Emre, 2013) (Figure 4.2). The rugged topography and the complex geology of this segment suggest this zone as an ideal deformed region to apply multi-spectral remote sensing analyses for examining its total deformation. In this study, we aim to combine ASTER-based remote sensing analyses with available field data and statistically detected low levels of spectral information (High optimum index factor – OIF) in order to refine the geological map of the region and to measure the cumulative offset along this segment of the EAF. In addition to this, our results

provide valuable information on the evolution not only for this particular segment but also for the whole EAF as well.
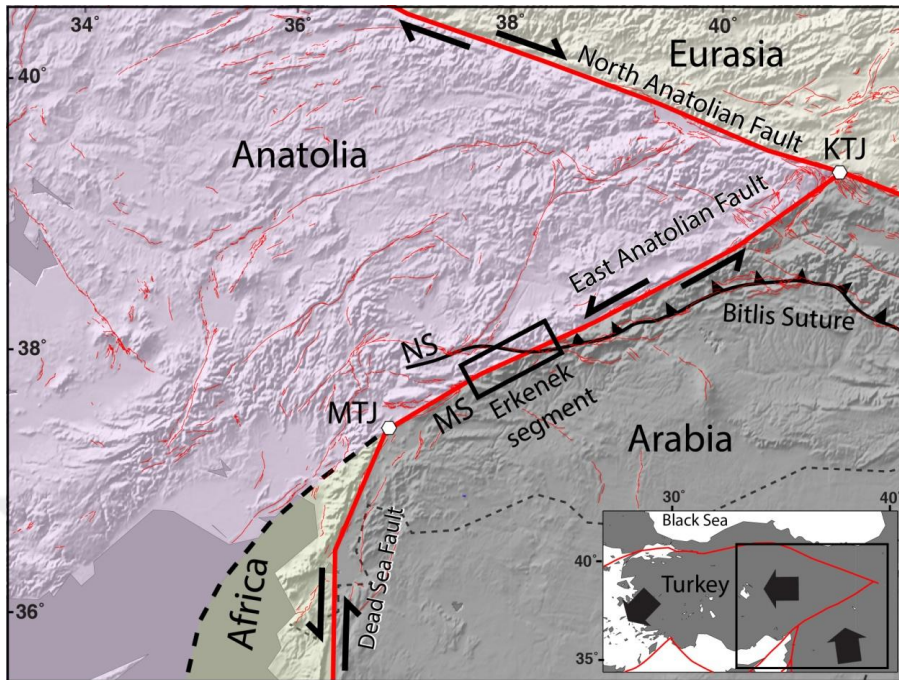
Figure 4.1 : Shaded relief image (data from SRTM-30; Farr et al., 2007) of eastern Turkey showing the African, Arabian, Anatolian and Eurasian lithospheric plates and major active Faults (thick red lines). Abbreviations: MTJ, Maraş triple junction; KTJ, Karliova triple junction; MS, main strand, and NS, a northern strand of the East Anatolian Fault. The black box shows location of the study fault segment.
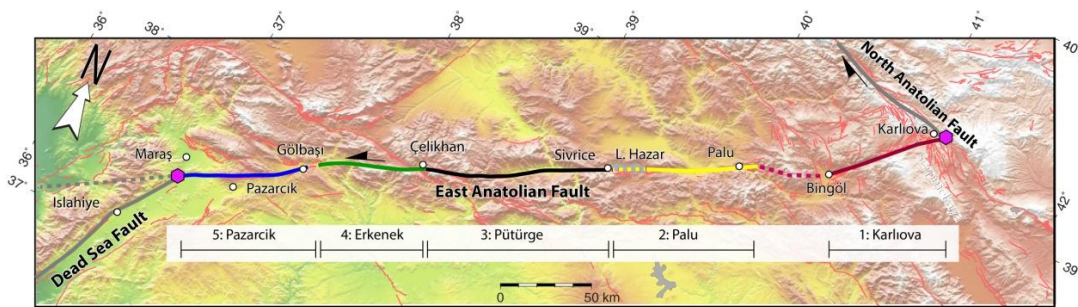
Figure 4.2 : Segmentation of the East Anatolian Fault following Duman and Emre (2013). Pink hexagons indicate the locations of the Karliova and Maraş triple junctions.

4.2 Geological Setting

Along the Along the Erkenek Segment, the age of lithological units ranges from Pre-Cambrian to Holocene time. According to the geological map of Herece (2008) (Figure 4.3), the Pre-Cambrian Pütürge metamorphics is mostly exposed at the

eastern parts of the segmented zone. The lower Permian crystallized limestone covers a region in the north part of the fault and two small elongated parts in the western part of the Erkenek Segment. The Devonian-Carboniferous Yoncayolu Formation that includes schist, recrystallized limestone, and quartzite located in the western part of the study region. Calc-schist and schist with marble of the lower Triassic are found inside the crystallized limestone unit in the northern part of the study zone.

The Middle-Upper Triassic–Cretaceous Kayaköy Formation crop out on both sides of the fault in the eastern and western parts of the study region. The Kayaköy Formation is very important in terms of measuring the lateral fault offset. This unit is composed of dolomite and rarely crystallized limestone (Herece, 2008) (Figure 4.3). The Upper Triassic–Cretaceous units are covering most of the southern parts of the study zone. The Upper Cretaceous is recognized by Ula Formation that generally distributed in the central and western parts of the study region. Ula and Kayaköy formations together in the same unit show one of the geological offsets in the northern part of the Erkenek Segment. The Upper Cretaceous meta-conglomerates that characterized the unit of Ula and Kayaköy formations, is a very good marker for measuring the lateral segment offsets. The other Upper Cretaceous units that include Berit meta-ophiolite, Hatay ophiolite, Gulman ophiolite and granitoids, are distributed almost along the fault zone (Herece, 2008) (Figure 4.3).
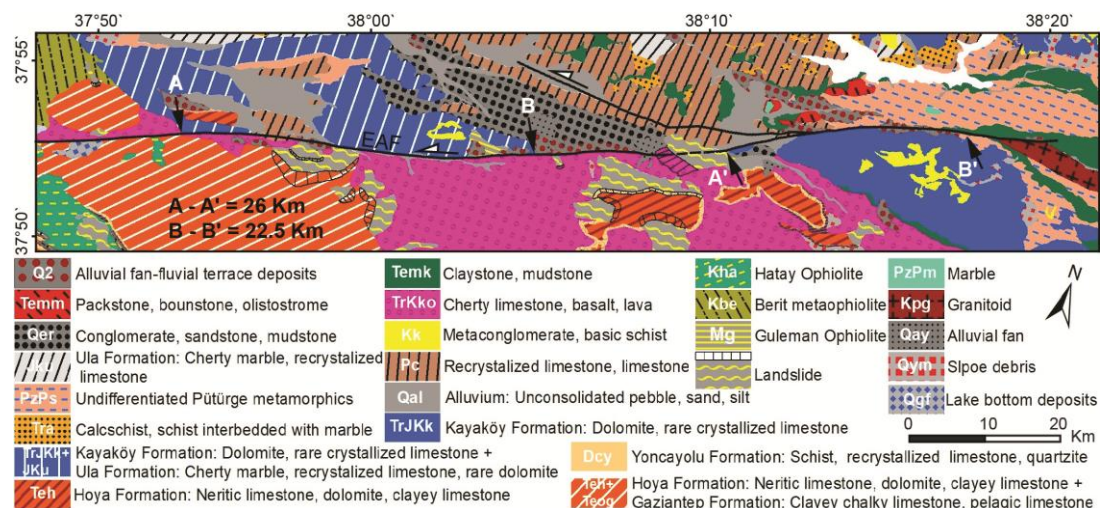
Figure 4.3 : Geological map of the Erkenek Segment (Modified after Herece, 2008).

The Lower-Middle Eocene rocks are represented by thin elongated bodies of claystone and mudstone in the eastern and upper-middle parts of the study region.

Hoya Formation that took place during Lower-Middle Eocene time is composed of neritic and clayey limestone and located in the lower-middle part of the study zone. Middle-Upper Eocene is represented by Melefan Formation that includes packstone and olistostrome. The Melefan Formation is recorded in two small parts above the linkage point between the southern and the northern fault strand (Herece, 2008) (Figure 4.3). Gaziantep Formation belongs to Eocene-Oligocene and consists of chalky and pelagic limestone.

Gaziantep and Hoya Formations occupy most of the western study region. Conglomerate, sandstone, and mudstone of the Lower Pleistocene are recorded in the middle northern part of the fault segment. Upper Pleistocene-Holocene lithology crops out along the fault trace line. The Holocene deposits were mapped in the study zone as alluvial sediments mostly located in the central section of the fault segment. Slope debris units are recorded in small regions in the northeastern and northwestern sections. Lake bottom deposits are mapped in the western part section. Alluvial deposits were recorded in the eastern, middle and western sections of the study fault segment zone (Herece, 2008) (Figure 3).

The geological offsets along the Erkenek Segment were measured between Kayaköy Formation in the southern part of the fault segment and the Kayaköy and Hoya formations as one unit, in the northern part of the fault segment. The offsets are 22.5 km and 26 km respectively in both measured locations. (*Herece, 2008*) (Figure 4.3).

4.3 Materials and Methods

The ASTER satellite images are recorded in 14 spectral bands with different wavelength ranges; three bands in visible and near-infrared (VNIR) with 15 m spatial resolution, six bands in short-wave infrared (SWIR) with 30 m spatial resolution, and five bands in thermal infrared (TIR) with 90 m spatial resolution. The great advantage of the ASTER dataset is its unique combination of wide spectral coverage and high spatial resolution visible near-infrared band (Gad and Kusky, 2007). Therefore, the ASTER data enhance the efficiency to discriminate the boundaries between the different lithological units. ASTER data is well known to have been used in analyses in many geological and tectonic applications (e.g., Bedell, 2001; Rowan et al., 2003; Ninomiya et al., 2005; Gad and Kusky, 2007; Gürsoy et al., 2017).

Relatively multi-numbered bands of ASTER satellite images and their wide wavelength ranges are ideal for making a distinguishment between broad ranges of lithological compositions (Gad and Kusky, 2007). In comparison to other datasets such as Landsat TM and ETM+ images, ASTER data provide a great innovation regarding to their higher spatial resolution and improved spectral characteristics (e.g., Okada and Ishii, 1993; Bedell, 2001; Rowan and Mars, 2003; Velosky et al., 2003; Gad and Kusky, 2007; Rajendran et al., 2013; Gürsoy et al., 2017). Hence, in the same track of Landsat TM and ETM+, ASTER band ratio combinations and band math are successful in emphasizing spectral features of certain rocks and mineral and therefore are more effective in lithological mapping compared to the RGB band combinations images (Okada and Ishii, 1993; Abdeen et al., 2001; Bedell, 2001; Hewson et al., 2001; Rowan and Mars, 2003; Rowan et al., 2003; Velosky et al., 2003; Gad and Kusky, 2007). The VNIR bands are successfully used in vegetation and iron-oxide minerals mapping (Bedell, 2001), whereas the SWIR bands are useful for soil and lithological mapping (Yamaguchi and Naito, 2003). The TIR bands are applied specifically to discriminate and map the silicate rocks (Yamaguchi et al., 1998).

4.4 ASTER-data Analysis and Interpretation

Following Gad and Kusky (2006), we first analyzed the 7-3-1 band combination that displays the clear distribution of some units such as Kayaköy Formation in the northeastern part of the study region (Figure 4.4). In the southeastern part of the study region, the polygon coverage area of Hoya and Gaziantep formations is discriminated by this band combination as well (Figure 4.4). Within this combination, the alluvial deposits are also well represented that occupy the most northern parts of the study region (Figure 4.4).
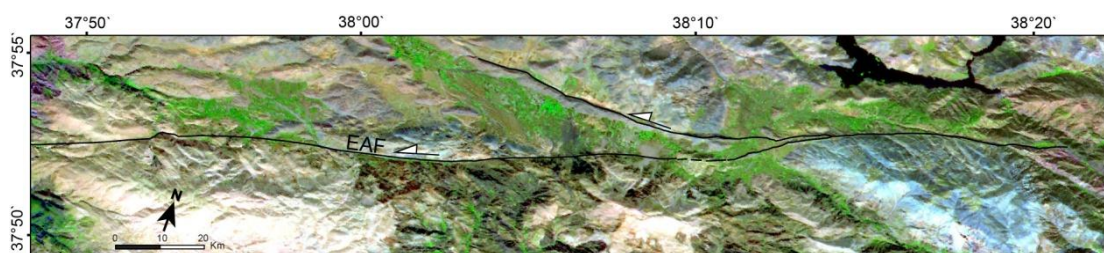
Figure 4.4 : ASTER 7-3-1 image for Erkenek fault segment region.

On the other hand, other band combinations for this image or other images do not offer many details for different lithological units along the Erkenek Segment. Therefore, we explore the rationing technique that is widely applied for lithological mapping because of their proven ability to enhance rock compositional differences (Mustard and Sunshine, 1998).

We selected the optimal bands for band ratio images according to (1) Optimum Index Factor, OIF; that is a statistical approach for detecting the maximum ranking of combinations of three channels out of the spectral bands (Chavez et al., 1982) and (2) the spectral properties of the surface material of interest and its abundance in comparison with to other surface cover types (Sabine, 1999; Gad and Kusky, 2007), and is depending on the selection of bands that carry the greatest variance with the least correlation (Jensen, 1996; Gad and Kusky, 2007).

This is the first remote sensing study for the Erkenek Segment, which uses the ASTER images' band-ratios 1/3-1/9-3/9 (Figure 4.5), 7/3-1/7-3/5 and 9/5-5/3-3/1 (Figures 4.6 and 4.7, respectively). ASTER image with band ratios 1/3-1/9-3/9 represents the highest optimum index factor (OIF) and indicative spectral characters. Interpretation of this ASTER band ratio image clearly shows that this combination provides the best resolution in the identification of different lithological units and their contacts when it is compared to the standard ASTER band combinations.

1: TrJKk; 2: TrJKk+JKu; 3: Teh; 4: Teh+Teog; 5: TrKko; 6: Qer; 7: Pc; 8: PzPs; 9: Qal; 10: Kbe; 11: Kha; 12: Jku; 13: Kpg; 14: Temk; 15: Temm; 16: Kk; 17: Tra; 18: Qay; 19: Qgf; 20: Dcy
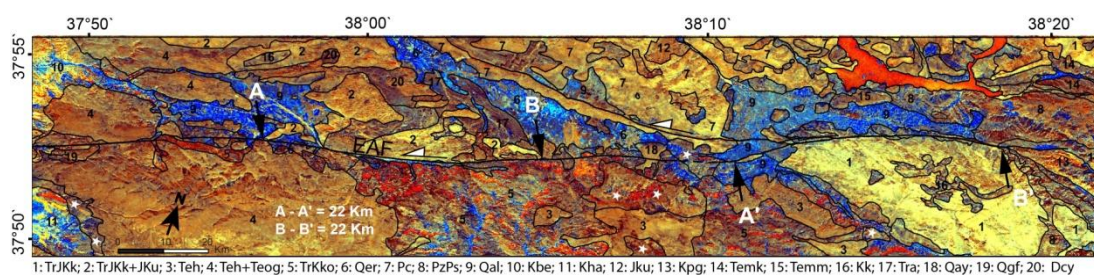
Figure 4.5 : ASTER band ratio image (1/3-1/9-3/9) in RGB. White stars indicate the landslide.

In this chapter, the main lithological units of the study region are successfully differentiated and identified as follows: (1) The Kayaköy Formation (Polygon no. 1), that is located in the northeastern part of the study region and is represented with light yellow colour, (2) The part made of both Kayaköy and Ula formations (Polygon no. 2) is accepted as a single unit and this unit is well differentiated from the adjacent rocks in the northwestern parts with its yellow colour, (3) Hoya Formation (Polygon no. 3) is characterized with its brown colour to the south of the fault, (4) Hoya and

50

Gaziantep formations (Polygon no. 4) together form the biggest unit of the study region, mostly distributed to its western parts, and is distinguished by reddish brown colour, (5) Cherty limestone and basalts (Polygon no. 5) cover relatively a big area in the southern-central part of the fault segment and is well separated from the adjacent rocks with its yellowish red colour, (6) Conglomerate and sandstone (Polygon no. 6) is represented and located as an elongated body with yellowish blue colour in the northern-central part, (7) Recrystalized limestone (Polygon no. 7) is discriminated by yellowish brown colour and located in the middle northern part of the study segment, (8) Pütürge metamorphics (Polygon no. 8) is distinguished with a dark blue colour at both eastern and western parts of the study region, (9) The alluvium (Polygon no. 9), and (10) Berit metaophiolite and Hatay ophiolite (Polygons no. 10 and 11) that occupy relatively small areas at the most northeastern and southeastern corners of the study segment, respectively (Figure 4.5).
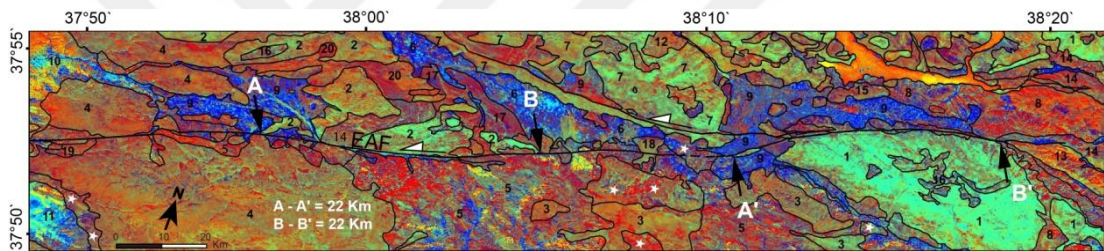
Figure 4.6 : ASTER band ratio image (9/5-5/3-3/1) in RGB.
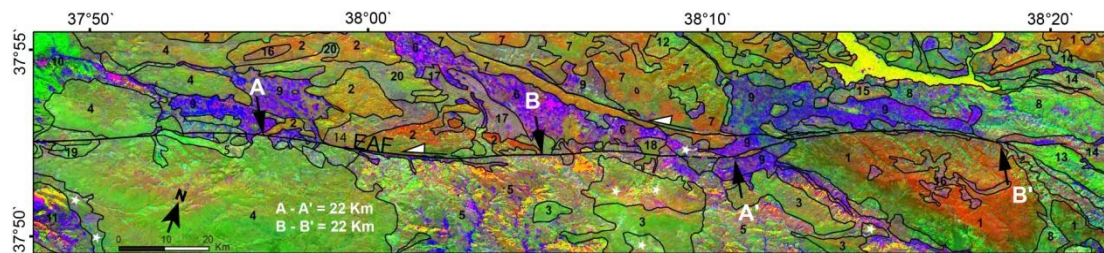
Figure 4.7 : ASTER band ratio image (7/3-1/7-3/5) in RGB.

The ASTER images made of this band ratios display the geological offsets along the Erkenek Segment at two points, including the one within the Kayaköy Formation in the southern part of the fault and another one within the Kayaköy and Ula formations in the northern part. We measured a total of 22 km sinistral displacement between piercing points A-A' and B-B' at both of these localities (Figure 4.8). It is clear that the ASTER band ratio images of 1/3-1/9-3/9, 7/3-1/7-3/5 and 9/5-5/3-3/1 are

51

powerful in discriminating the subtle contacts between the different lithological units along the Erkenek Segment.

Correlation between the previously published geological maps (e.g. Herece, 2008) and our ASTER-based results supports the conclusion about the utility of the newly adopted ASTER images. Calcschist, schist and marble units are clearly discriminated from the surrounding rocks in our analysis (Figure 4.8), whereas these lithological units are mapped as the conglomerate, sandstone, and mudstone units in the Herece (2008)'s map (as Qer in Figure 4.3). Also, the claystone with mudstone (Figure 4.8) is neatly separated from the unit of Kayaköy and Ula Formations (Polygon no. 2) in the Herece (2008)'s map. Geological offsets between A – A' and B – B' are found both to be 22 km, while they are suggested to be 22.5 km and 26 km respectively in Herece (2008)'s geological map (Figures 4.2 and 4.8).
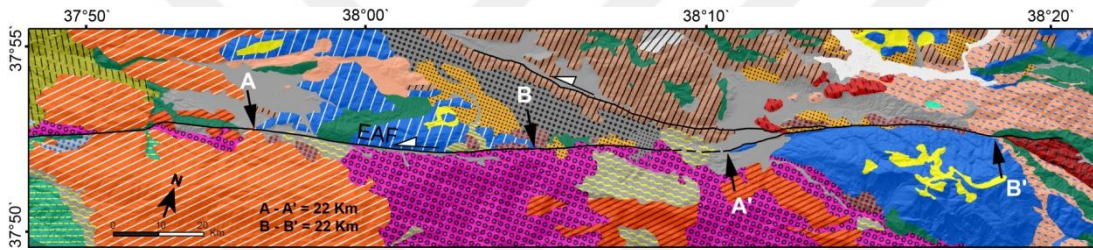
Figure 4.8 : Refined lithological map obtained in this study.

4.5 Conclusion

The results obtained from ASTER image interpretations are consistent with the published Herece (2008)'s geological map on a large scale. This indicates that combining a high-resolution ASTER data with other field information is positive and appropriate for detailed lithological mapping. The evaluation of the newly developed ASTER band ratio technique proved to be a strong tool for lithological mapping and checking the recorded geological offsets along the Erkenek Segment of the EAF. The ASTER band ratios measure the geological offsets as 22 km at the both examined locations along the Erkenek Segment. The new band ratio images are adjusted to discriminate between various rock units and formations of pre-Miocene age. Therefore, it is recommended for detailed lithological mapping and offsets along other regions. We suggest ASTER image enhancement techniques as time- and cost-effective methods for detailed lithological mapping along the active regions.

5. EVALUATION OF THE RELATIVE TECTONIC ACTIVITY OF THE ADIYAMAN FAULT WITHIN THE ARABIAN-ANATOLIAN PLATE BOUNDARY (EASTERN TURKEY)

5.1 Introduction

Deformation within tectonically active areas is mostly examined and determined using geomorphic, geodetic and geologic data (Molin et al., 2004; Dumont et al., 2005; Necea et al., 2005). Recent tectonic activity along faults that are associated with continental deformation gives rise to varied tectonic landforms and landscapes (Gordon, 1998; Giamboni et al., 2005). Geomorphic indices, provide a means to help assess the tectonic activity/deformation along active faults, allowing sections of the fault to be dividing into stretches of relative tectonic activity (Bull and McFadden, 1977; Rockwell et al., 1985). Geomorphic analysis has previously been successfully applied to many tectonically active areas, including Central America (Wells et al., 1988), California (Lifton and Chase, 1992), Southern Italy (Molin et al., 2004), Southern Spain (Pérez-Peña et al., 2010), Eastern North America (Frank et al., 2011), Western Pakistan (Ul-Hadi et al., 2013), Northern Turkey (Selim et al., 2013), Central Anatolia, Turkey (Yıldırım, 2014), and Eastern Turkey (Selçuk, 2016). We examine the Adıyaman Fault in Eastern Turkey building on these studies to gain further insights into the geomorphic development along active faults and the neotectonics of Anatolia. The Adıyaman Fault is a left-lateral strike-slip fault and is locating in a zone of the continental-scale left-lateral strike-slip East Anatolian Fault. The Adıyaman Fault was mapped by Aksoy et al. (2007), but few studies have been undertaken along the Adıyaman Fault despite it being an ideal area to examine the relative tectonic activity/uplift within a continental transform setting. We apply quantitative geomorphometric methods to assess its tectonic activity and how deformation varies along its length. Ultimately, our research will aid in the evaluation of the Adıyaman Fault for seismic hazard mitigation and as a guide for future active tectonic studies.

5.2 Regional Setting of the Study Area

Eastern Anatolia is a province characterized by a N-S compressional tectonic regime (Figure 5.1). Conjugate dextral and sinistral strike-slip faults that are sub/parallel the North and East Anatolian fault zones are the most significant structural features in the region (Bozkurt, 2001). Many of the faults in the Eastern Anatolian region are seismically active and they have been the source for numerous destructive earthquakes, e.g., the September 13, 1924 Pesinler (*Ms=6.8*), the October 30, 1983 Horasan-Norman (Ms= 6.8), the June 6, 1986 Doğanşehir (*Ms=5.6*) and the March 2, 2017, Adıyaman-Samsat (*Mw 5.5*) (Canıtez and Üçer, 1967; McKenzie, 1972; Barka et al, 1983; Ambraseys, 1988; Taymaz et al., 1991; Toksöz et al., 1983; Eyidoğan et al., 1999) earthquakes.
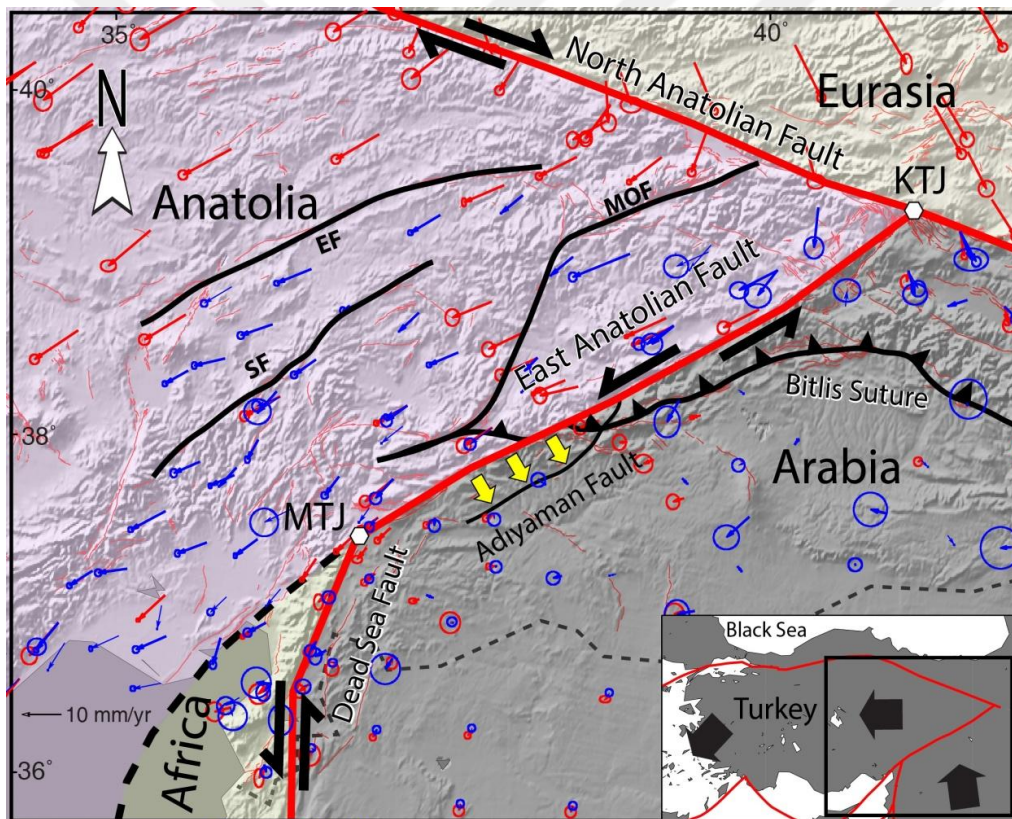
Figure 5.1 : Shaded relief image (data from SRTM-30m resolution; Farr et al., 2007) of eastern Turkey showing the African, Arabian, Anatolian and Eurasian plates and major active faults (thick black and red lines). The yellow arrows show the Adıyaman Fault. Red and blue arrows indicate GPS velocities with respect to a fixed Arabian lithospheric plate, with blue and red circles indicate GPS measurements errors, according to Reilinger et al. (2006) and Aktuğ et al. (2016), respectively. Abbreviations: MTJ, Maraş triple junction; KTJ, Karliova triple junction; EF, Ecemiş Fault; SF, Savrun Fault; OF, Ovacık Fault.

The East Anatolian Fault was first described by Allen (1969) who showed that it forms part of the transform boundary between the Anatolian and Eurasian plates, and the African and Arabian plates. A series of faults are present trending sub/parallel or oblique to the main trend of the East Anatolian Fault zone (Şengör et al., 1985; Hempton, 1987; Taymaz et al., 1991; Şaroğlu et al., 1992a; Westaway, 1994). Views on the timing of initiation of the East Anatolian Fault range from Late Miocene to Early Pliocene (Arpat and Şaroğlu, 1972; Şengör et al., 1985; Dewey et al., 1986; Hempton, 1987; Perinçek and Çemen, 1990). Extending ~ 75km in ~ 65° NE direction, the Adıyaman Fault is one of the faults that are parallel to the main East Anatolian Fault (Figures 5.1and 5.2).
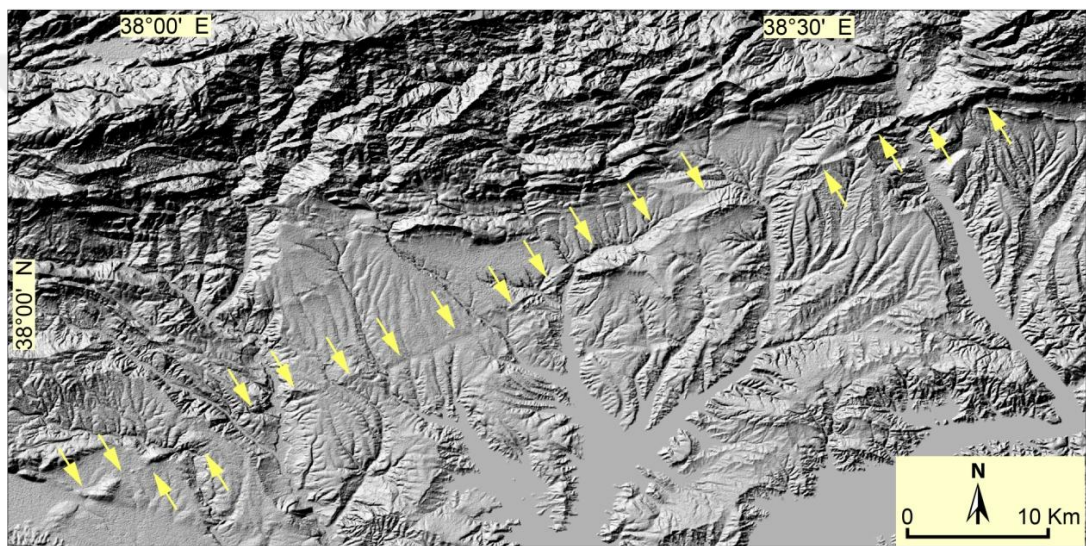
Figure 5.2 : Shaded relief image showing the trace of the Adıyaman Fault, indicated by yellow arrows (data from SRTM-30m resolution; Farr et al., 2007).

The seismic record associated with the Adıyaman Fault is characterized by low to moderate frequency of relatively small to moderate magnitude (M_w 3.0–5.5) earthquakes. The Adıyaman-Samsat earthquake was the largest recorded on the fault and occurred at 14:07 (local time) on March 2, 2017, with a M_w of 5.5 (Figure 5.3). Major rock types along the Adıyaman Fault zone include Plio-Quaternary undifferentiated continental clastic and carbonate rocks, Middle-Upper Miocene continental clastic rocks, and Upper Cretaceous ophiolitic mélange rocks (Figure 5.4). The age of the Adıyaman Fault has yet to be determined, but Şengör et al. (1985) and Dewey et al. (1986) suggests it could have been initiated during the Late Miocene to early Pliocene at the same time as the East Anatolian Fault. The total displacement of the Adıyaman Faults has as yet to be determined.
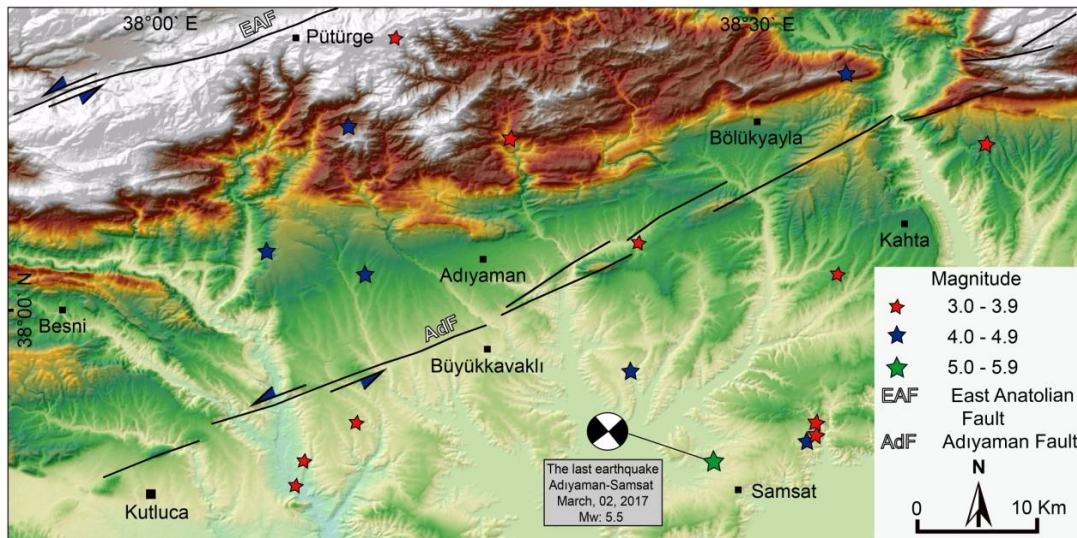
Figure 5.3 : Seismotectonic of the study area. AdF, Adıyaman Fault, EAF, East Anatolian Fault. Digital elevation model was generated from 30m SRTM (Shuttle Radar Topography Mission).
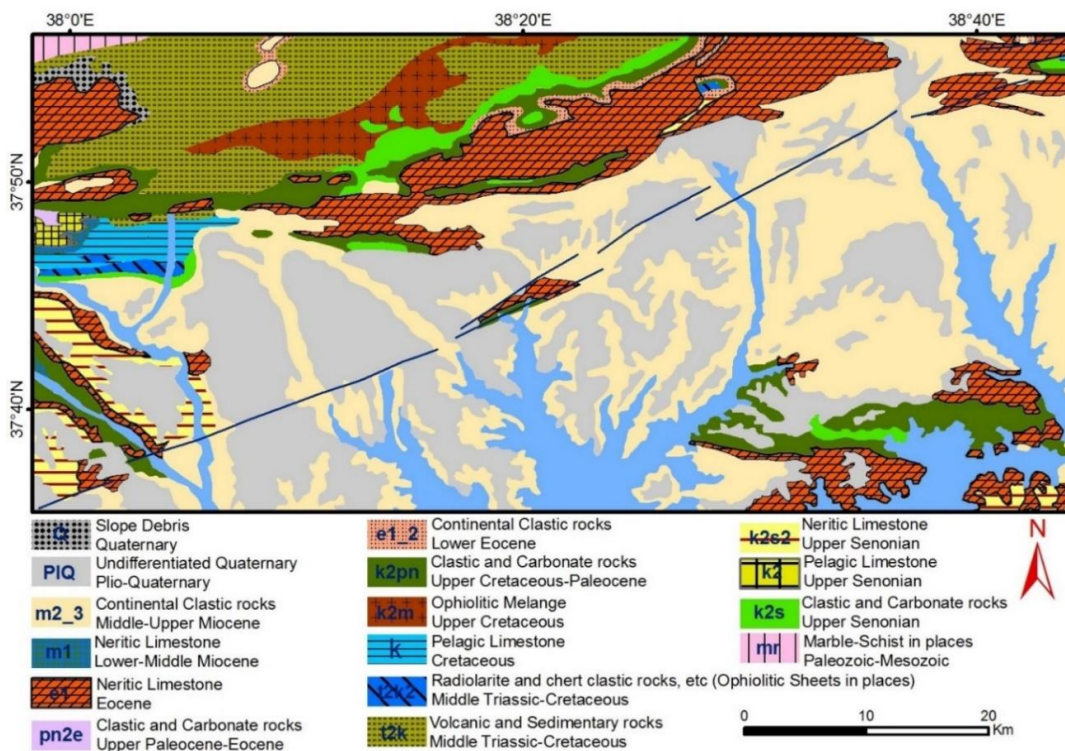
Figure 5.4 : Geology along and adjacent to the Adıyaman Fault, EAF, East Anatolian Fault (from Herece, 2008).

5.3 Methods

In this chapter, the Adıyaman Fault is divided into seven segments on the basis of changes in the trend of the fault trace (Fig. 5.3). Mountain front sinuosity (S_{mf}) and valley floor width to height ratio (V_f) indices were calculated for each of the seven

segments along the Adıyaman fault. Geomorphic indices including catchment asymmetry factor (Af), basin hypsometric integral (Hi) and hypsometric curves, and drainage density (D_d) were calculated for 42 catchments that cover the entire fault. All the catchments and streams were extracted from the Shuttle Radar Topography Mission (SRTM) digital elevation model (DEM) that had a 30-m resolution (Farr et al. 2007), and from Google Earth [TM] satellite images.

5.3.1 Relative tectonic activity index (RTA)

Using the methods of El Hamdouni et al. (2008), we classified every geomorphic index into three classes (numbered 1 through 3) and calculate an average class value that we call G_{av} (Table 5). Using the G_{av} we define three RTA classes such that class 1 is 0.5< G_{av} <2 (high tectonic activity), class 2 is $2 \le G_{av} > 2.5$ (moderate tectonic activity), and class 3 is $G_{av} \ge 2.5$ (low tectonic activity).

5.4 Results

5.4.1 Mountain front sinuosity (S_{mf})

There is a clear decrease in S_{mf} index values from 1.27 to 1.00 from segment 1 to 7 along the fault, albeit not by much (Figure 5.5; Table 5.1).
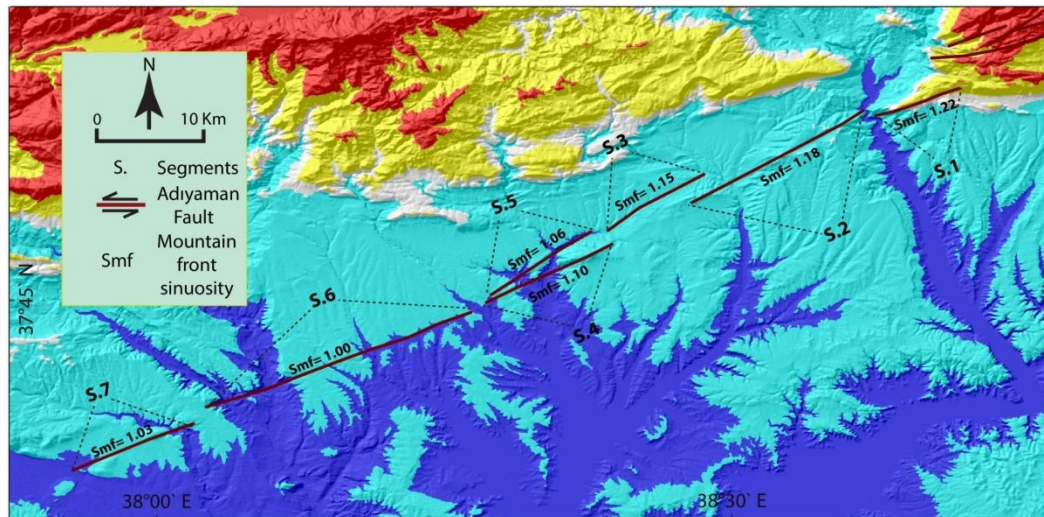
Figure 5.5 : Segments of the Adıyaman Fault. Digital elevation model was generated from 30 m SRTM data.

5.4.2 Valley floor width-to-valley height ratio (V_f)

The mean V_f index values range from 0.35 to 1.72 along all segments of the mountain front, indicating that most of the valleys are V-shaped (Figure 5.6; Table

5.2). The values of S_{mf} and V_f signify that there is a clear general conformability between them along the whole segments except segment 7 (Figure 6.7; Table 5.2). The mean V_f values gradually decrease from segment 1 to 7.
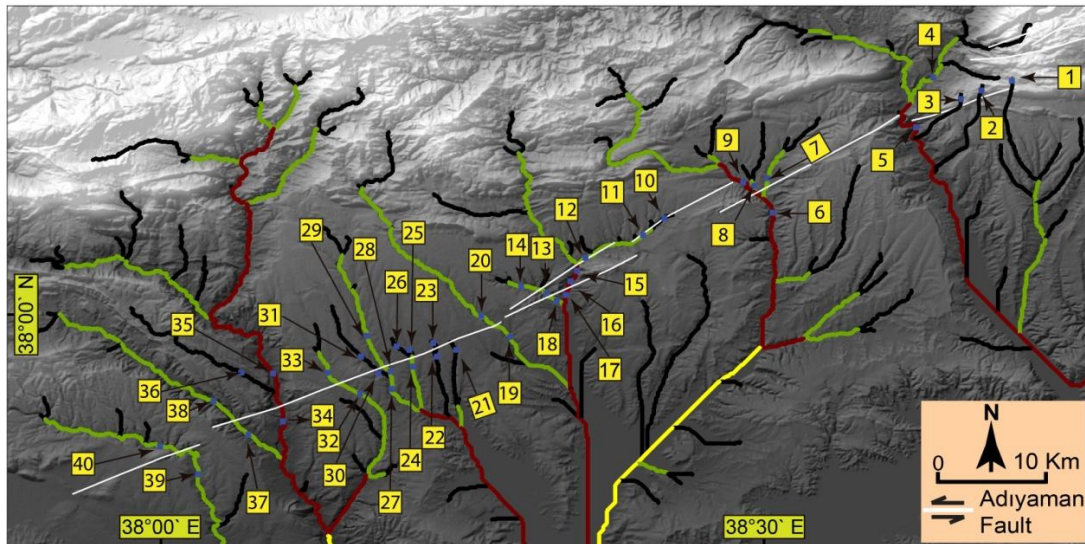
Figure 5.6 : The distributed values of valley floor width-to-height ratio (V_f) along all Segments of the Adıyaman Fault.

Table 5.1 : Mountain front sinuosity (S_{mf}) and mean valley floor width-to-height ratio (V_f) values for each fault segment.

Segments	S_{mf}	S_{mf} Class	Mean V_f
S.1	1.22	1	0.98
S.2	1.18	1	0.92
S.3	1.15	1	0.90
S.4	1.1	1	0.80
S.5	1.06	1	0.75
S.6	1.0	1	0.64
S.7	1.03	1	0.45

5.4.3 Catchment asymmetry factor (A_F)

A_F values range from 21 to 83 (*Figure 5.8; Table 5.3*). Catchments 6, 7, and 8 in the eastern part of the fault are symmetric, while catchments 26, 28, 33, 34, 41, and 42 in the central and western stretches of the fault are slightly asymmetric. Segments 4 and 5 in the central stretch of the fault have the highest asymmetry values (classes 1 and 2, moderately and strong asymmetry), while the eastern stretch of the fault contains catchments with third and last classes of symmetry.

Table 5.2 : Valley floor width-to-height ratios (V_f) for the streams along the study fault.

Streams No.	V_f	Streams No.	V_f
1	0.85	21	0.76
2	0.99	22	0.66
3	1.35	23	0.68
4	1.08	24	0.45
5	0.61	25	1.72
6	1.10	26	1.10
7	1.46	27	0.59
8	0.80	28	0.35
9	0.30	29	0.53
10	0.51	30	0.59
11	1.30	31	0.55
12	0.97	32	0.57
13	0.76	33	1.28
14	0.71	34	0.72
15	0.52	35	0.57
16	0.95	36	0.52
17	0.80	37	0.59
18	1.22	38	0.71
19	0.52	39	0.30
20	0.57	40	0.61
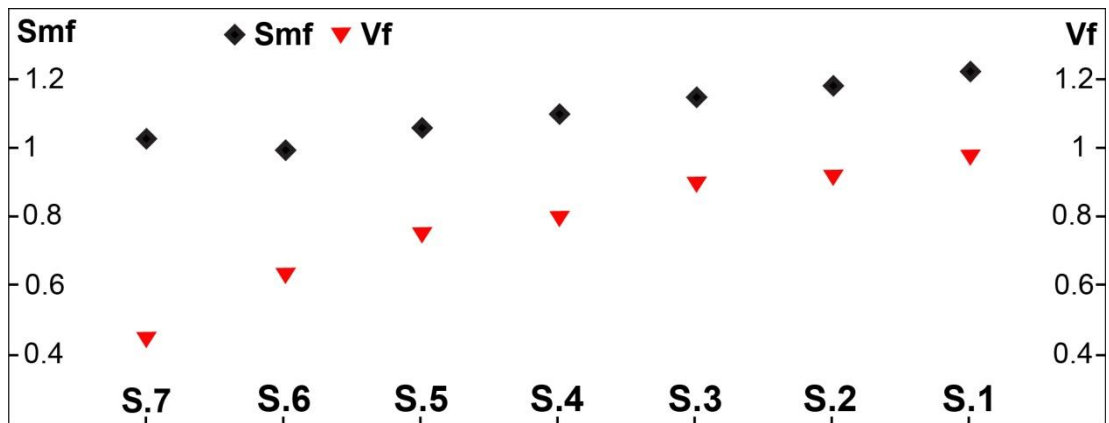
Figure 5.7 : Along-strike variations of the Smf and Vf values. Distribution of both values shows a close relationship with relief. Low Smf and Vf values are compatible with higher relief and topography hence higher displacement. S.1 through S.7 refer to the fault segments.
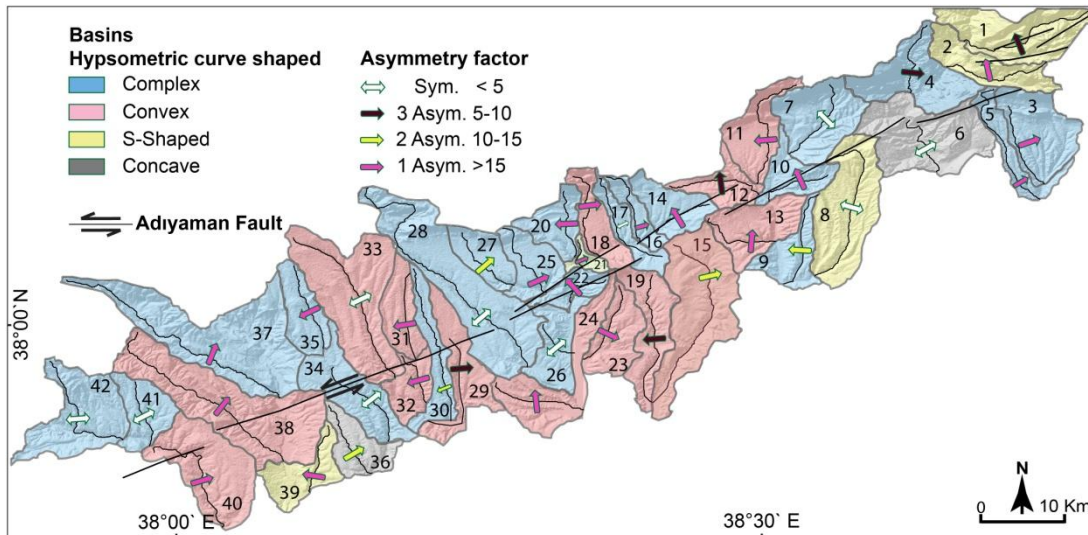
Figure 5.8 : Results of the drainage basins/catchments categorized by hypsometric curves shapes and asymmetry factor (AF) values.

Table 5.3 : Asymmetry factor (AF) values for the catchments within the study area.

Basin No.	AF	AF-50	Class	Basin No.	AF	AF-50	Class
1	44	-6	3	22	21	-29	1
2	34	-16	1	23	76	26	1
3	82	32	1	24	27	-23	1
4	59	9	3	25	59	19	1
5	71	21	1	26	46	-4	-
6	51	1	-	27	60	11	2
7	52	2	-	28	53	3	-
8	51	1	-	29	55	5	3
9	38	-12	2	30	39	-11	2
10	26	-24	1	31	23	-27	1
11	26	-24	1	32	31	-19	1
12	56	6	3	33	47	-3	-
13	77	27	1	34	46	-4	-
14	33	-17	1	35	27	-23	1
15	61	11	2	36	64	14	2
16	66	16	1	37	83	33	1
17	52	2	-	38	69	19	1
18	79	29	1	39	33	-17	1
19	43	-7	3	40	78	28	1
20	27	-23	1	41	49	-1	-
21	73	23	1	42	54	4	-

5.4.4 Hypsometric analysis

Most of the catchments have convex and complex hypsometric curves (Figure 5.9A and D). Only catchments 6 and 36 have concave hypsometric curves (Figure 5.9B). Catchments 1, 2, 8, and 39 have S-shaped hypsometric curves (Figure 5.9C). The catchments with the convex hypsometric curves probably have a high rate of uplifting. The irregular and complex shapes of hypsometric curves could be due to active continuous erosion at the head and foot of the streams and/or stream piracy events, that most probably due to active tectonics in conjunction with lithological control factors (Giaconia et al., 2012). All segments mostly have catchments that have hypsometric curves ranging from convex to irregular shapes, and Hi values that range from low to intermediate (Table 5.4).

5.4.5 Drainage density (D_d)

D_d values range from 2.54 to 4.03km-1 (Table 5.4). The lowest Dd value is for catchment 24 while catchment 29 has the highest Dd value.
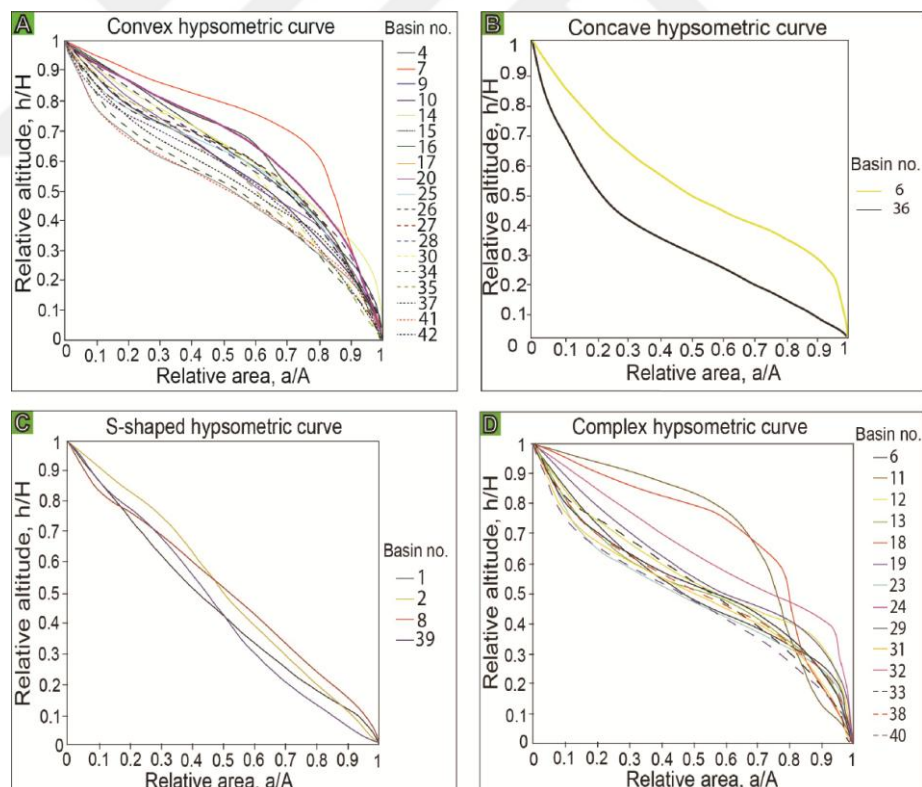
Figure 5.9 : Results of the catchments categorized by hypsometric curves shapes. (A) Hypsometric curves for weakly eroded basins. (B) Hypsometric curves for highly eroded basins. (C) Hypsometric curves for moderately eroded basins. (D) Hypsometric curves for basins with stream rejuvenation processes at the foot or head of the stream.

Table 5.4 : Drainage density values (Dd) and the hypsometric integral of the catchments of the study area.

Basin No.	Dd	Dd Class	Hi	Hi Class	HC Class	Basin No.	Dd	Dd Class	Hi	Hi Class	HC Class
1	3.39	1	0.51	1	2	22	2.97	2	0.24	3	-
2	3.33	1	0.98	1	2	23	2.99	2	0.24	3	-
3	3.29	1	0.28	3	-	24	2.54	2	0.15	3	-
4	3.35	1	0.24	3	1	25	2.87	2	0.36	2	1
5	3.29	1	0.26	3	-	26	3.08	1	0.27	3	1
6	3.29	1	0.31	2	3	27	2.9	2	0.29	3	1
7	3.29	1	0.26	3	1	28	3.21	1	0.28	3	1
8	3.11	1	0.52	1	2	29	4.03	1	0.37	2	-
9	3.11	1	0.34	2	1	30	2.76	2	0.36	2	1
10	3.23	1	0.37	2	1	31	3.04	1	0.45	2	-
11	3.04	1	0.27	3	-	32	2.87	2	0.48	2	-
12	3.04	1	0.38	2	-	33	3.15	1	0.45	2	-
13	3.20	1	0.39	3	-	34	3.22	1	0.57	1	1
14	3.10	1	0.23	3	1	35	2.77	2	0.42	2	1
15	3.16	1	0.40	2	1	36	2.96	2	0.66	1	3
16	3.21	1	0.25	3	1	37	3.23	1	0.36	2	1
17	2.98	2	0.18	3	1	38	3.22	1	0.36	2	-
18	3.22	1	0.28	3	-	39	2.96	2	0.51	1	2
19	3.03	1	0.25	3	-	40	2.95	2	0.40	2	-
20	3.30	1	0.23	3	1	41	2.93	2	0.44	2	1
21	2.99	2	0.31	2	-	42	3.16	1	0.39	2	1

5.4.6 Relative tectonic activity (RTA)

Gav values range from 1.25 to 2.50. RTA with class 1 (high tectonic activity) mainly concentrates in the eastern and western areas of the Adıyaman Fault, while the middle part of the area has a different range of RTA classes from 1 to 2 (intermediate to high tectonic activity). Only catchment 4 in the east and catchment 27 in the middle stretch of the Adıyaman Fault have a RTA class of 3, indicating relatively low tectonic activity (Figure 5.10). RTA values include 36–38 % (by area) for class 1, 57–61 % for class 2, and 4–5 % for class 3 (Figure 6.11A and B). Averaging of the geomorphic indices classes of the active tectonics Gav and values of RTA are summarized in Table 5.5.
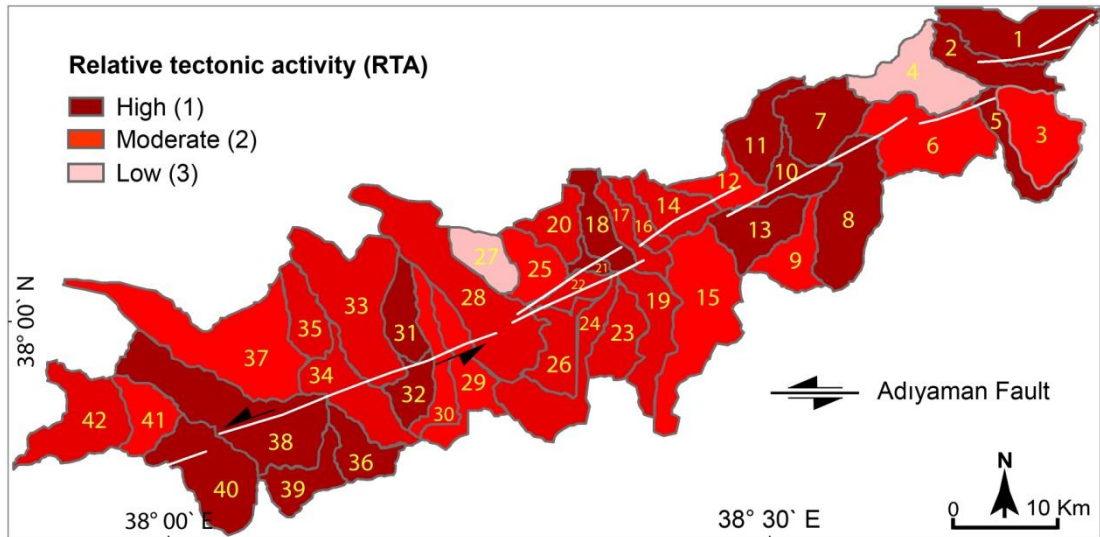
Figure 5.10 : Distribution of the RTA index of relative active tectonics along the study fault.
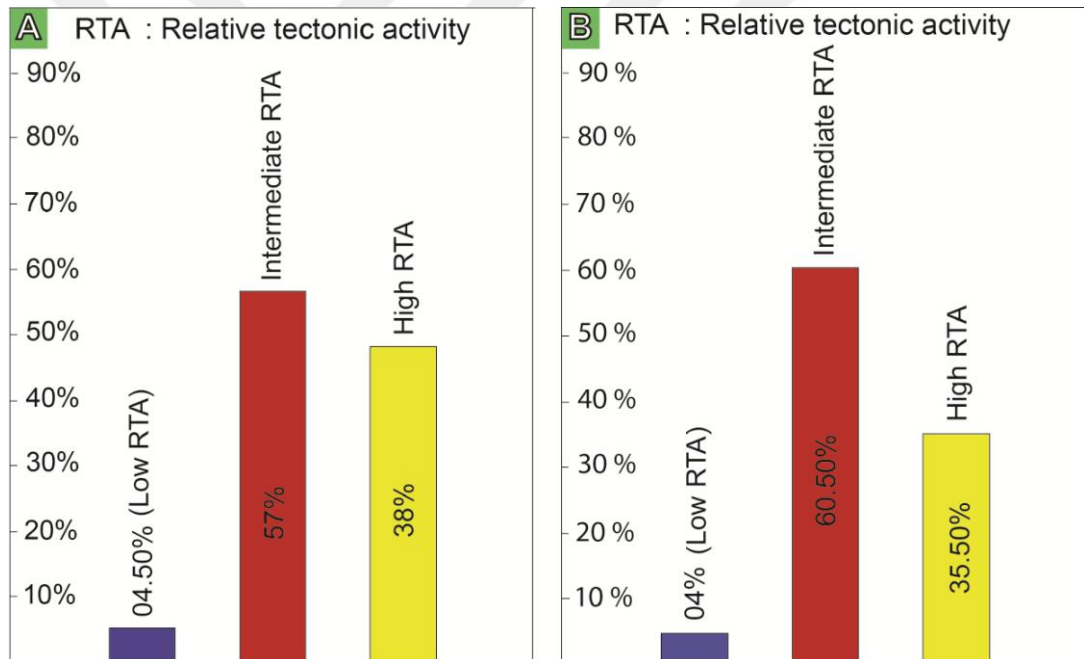
Figure 5.11 : The RTA percentage ratios based on (A) the basins numbers and (B) based on the catchment areas.

Table 5.5 : Classes of relative tectonic activity (RTA) for catchments with the study area (Dd: drainage density; Hi: hypsometric integral; Hc: hypsometric curves; AF: basin asymmetry factor; and Gav: Average of geomorphic indices).

Basin No.	Dd Class	Hi Class	HC Class	AF Class	Gav	RTA Class
1	1	1	2	3	1.75	1
2	1	1	2	1	1.25	1
3	1	3	-	3	2.33	2
4	1	3	3	3	2.50	3
5	1	3	-	1	1.25	1
6	2	2	3	-	2.33	2
7	1	3	1	-	1.66	1
8	2	1	2	-	1.66	1
9	1	2	3	2	2.00	2
10	1	2	3	1	1.85	1
11	1	3	-	1	1.25	1
12	1	2	-	3	2.00	2
13	1	2	-	1	1.25	1
14	1	3	3	1	2.00	2
15	1	2	3	2	2.00	2
16	1	3	3	1	2.00	2
17	2	3	3	1	2.25	2
18	1	3	-	1	1.25	1
19	1	3	-	3	2.33	2
20	1	3	3	1	2.00	2
21	1	2	-	-	1.5	1
22	2	3	-	1	1.25	1
23	2	3	-	1	2.00	2
24	2	3	-	1	2.00	2
25	2	2	3	1	2.00	2
26	1	3	3	-	2.33	2
27	2	3	3	2	2.50	3
28	1	3	3	1	2.00	2
29	1	2	-	3	2.00	2
30	2	2	3	1	2.00	2
31	1	2	-	1	1.33	1
32	2	2	-	1	1.66	1
33	1	2	-	-	1.50	1
34	1	3	3	-	2.33	2
35	2	2	3	1	2.00	2
36	2	3	1	2	2.00	2
37	1	2	3	1	2.00	2
38	2	2	-	3	1.75	1
39	2	3	2	1	2.00	2
40	2	2	-	1	1.66	1
41	2	2	3	-	2.33	2
42	1	2	3	-	2.00	2

5.5 Discussion

The relative plate motion between the northward movement of Arabian and westward moving Anatolian plates occurs along the East Anatolian Fault zone in eastern Turkey with slip rates between 6 and 10 mm/yr and high rate of seismic activity (Aktug et al., 2016). The East Anatolian Fault zone incorporates the Adıyaman Fault that is paralleling to the general trend of EAF trace. Applying the morphotectonic analysis is a good start to examine relative tectonic view of the fault zone because of the few studies on active tectonics along the Adıyaman Fault.

In our study, the S_{mf} and V_f chart confirms that each segment of Adıyaman Fault within the area is of Class 1 (Figure 6.12), which indicates uplift rates < 0.5 mm/yr (e.g. Rockwell et al., 1984; Mayer, 1986; Silva et al., 2003; Bull, 2007). This supports the view that the Adıyaman Fault is an active fault zone. The distribution of the geomorphic indices indicates that the areas which associated with different values of mountain fronts estimate different rates of relative tectonic activity (Table 5.5).
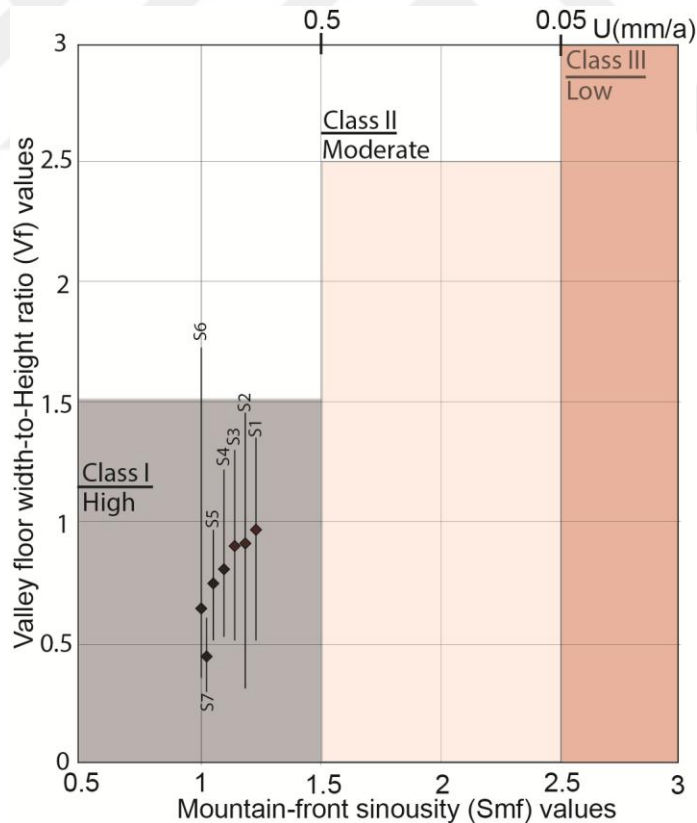
Figure 5.12 : The plot of Smf against Vf for the mountain fronts of each segment and inferred activity classes. Vertical bars show the standard deviation (σn-1) for Vf values. Numbers at the top indicate inferred uplift rates U (mm/yr) from Rockwell et al. (1984).

According to the RTA values in the study area, about 35.5% is classes 1 (High relative tectonic activity); 60.5% suggests a moderate relative tectonic activity (class 2), and 4% shows the lowest value of relative tectonic activity (class3). Thus, more than the half of the study fault is moderately tectonically active in terms of the apparent geomorphic indices response.

In northern and central regions of Turkey, the morphotectonic analysis was applied to define the relative tectonic activity of faults, including the North Anatolian and Tuz Gölü faults (Selim et al., 2013 and Yıldırım, 2014). Selim et al. (2013) examined the morphotectonic indices and confirmed that the southern branch of the North Anatolian Fault has RTA classes 1 and 2. The relative tectonic activity of the Tuz Gölü Fault zone in Central Anatolian was examined by Yıldırım (2014) who showed that each segment of the Tuz Gölü Fault is highly active (class 1).

Compared to geomorphic studies results of North Anatolian and Tuz Gölü faults, our analysis of the geomorphic indices indicates that the Adıyaman Fault suggests it is an intermediate to high activity fault zone (Table 5.5). All fault segments have the highest relative active tectonics (class 1; Table 5.1; and Figure 5.12) and the results from G_{av} and RTA analysis indicate moderate to high (classes 1; 2) relative tectonic activity along the entire study area. Based on our morphometric analysis, the Adıyaman Fault is likely characterized by shorter recurrence intervals and/or the potential for large earthquakes. Yıldırım (2014) highlighted that most of the seismic risk and hazard investigations concentrate on high-strain regions characterized by destructive earthquakes and high slip-rates. Nonetheless, the recently recorded large earthquakes in continental regions that show low-strain and slow slip-rates, e.g., Van in Turkey in 2011 (Fielding et al., 2013) suggest that it is also important to undertake similar studies in less strained regions, such as in Eastern Turkey. Despite the Adıyaman Fault dominantly being of intermediate RTA (class 2), the fault poses a significant seismic hazard in Eastern Anatolian region. The March 2, 2017, Adıyaman-Samsat earthquake (M_w 5.5) is a testament to this view that the Adıyaman fault zone is relative tectonically active.

The geomorphometric analysis does not directly indicate fault slip rates but helps highlight the potentially strong interaction between faults motion, earthquakes and surface processes that create landforms. Thus, the morphometric studies can provide a very good scenario of the relative tectonic activity degrees of the fault segments.

In eastern Turkey, the continuing northward Arabian plate movement with respect to Eurasia plate resulted in the Anatolian plate extrusion along the North and East Anatolian Faults, respectively (Şengör et al., 2005). The sinistral East Anatolian strike-slip Fault zone represents the main transform structure element in eastern Turkey. The EAFZ comprises some pure transform strike-slip faults that are parallel to the motion between Arabian and Anatolian plates, where other faults are oblique to the plate motion (Bozkurt, 2001). The East Anatolian Fault zone structure is very complicated that contains many pull-apart basins (Hempton et al., 1981), folding and thrust component (Arpat and Şaroğlu, 1972). Along the general trend of the EAF, the seismicity was observed along ~20–30-km-wide zone (Bulut et al., 2012). The seismicity of the East Anatolian Fault zone that records large destructive earthquakes, e.g., May 22, 1971, Bingöl earthquake (M_w 6.6) propose a high rate of tectonic activity along the main trace of the fault (Ambraseys, 1988). Bulut et al. (2012) suggest a systematic migration of moderate and micro-size (M_w 2.5 to 5.5) earthquakes from the main East Anatolian Fault into adjacent faults confirming the progressive interaction between the major trend of the EAF zone and its secondary structures. However, the RTA results of Adıyaman Fault that offer a moderate tectonic activity rate, suggest that it is of secondary importance after the East Anatolian Fault zone in the regional deformation of Anatolia. This is consistent with GPS studies (Reilinger et al., 2006; Aktuğ et al., 2016) that show no significant strain accumulation has been taking place across the Adıyaman Fault.

5.6 Conclusions

Quantitative geomorphic indices provide important clues about the effects of active tectonics. They are particularly helpful along the Adıyaman Fault where there are few active tectonics and paleoseismological studies. The relationship between values of S_{mf} with V_f, and the average combination of the other geomorphic indices including Hi, hypsometric curves, A_F, and D_d testify to the activeness of the Adıyaman Fault. The fault is divided into three classes of relative tectonic activity (RTA) based on G_{av} values. The entire fault is moderately to highly active, classes 2 and 3, based on the RTA analysis. The intermediate tectonic areas are concentrated in the middle part of the fault covering segments 2, 4, 5, and 6. Similarly, the western stretches of the fault have a high degree of relative active tectonics, while the eastern part indicates moderate to high degree of tectonics. The higher S_{mf} and V_f with RTA

values in the central and western stretches of the fault likely reflect a higher seismic risk with respect to the eastern parts of the fault zone. This suggests that the central and western stretches of the faults must be examined in more detail to better understand and evaluate the regional seismic hazard. In eastern Turkey, the motion between the Arabian and Anatolian plates resulted in the active East Anatolian strike-slip fault with secondary parallel strike-slip faults such as Adıyaman Fault. The RTA analysis suggests that the Adıyaman Fault is of secondary seismic importance after the East Anatolian Fault that represents the plate boundary between the Arabian and Anatolian plates with records of destructive earthquakes.

6. LITHOLOGIC AND TECTONIC MAPPING ALONG THE ADIYAMAN FAULT ZONE (EASTERN TURKEY) USING LANDSAT 8 (OLI) DATA

6.1 Introduction

Processing of digital images in remote sensing has greatly advanced in lithological discrimination of rock units and deposits, structural lineaments, and other geological features (Abrams et al. 1983; Sabins 1997; Rigol-Sanchez et al. 2003; Gad and Kusky 2007; Mwaniki et al. 2015a). Satellite data such as Landsat Thematic Mapper (TM) and Enhanced Thematic Mapper (ETM+), OLI, and ASTER, imagery provide information that is very useful in lithological recognition of rocks and lineation of tectonic elements. In the eastern desert of Egypt, the lithological maps were created using Landsat Thematic Mapper (TM) data (Gad and Kusky 2006). Landsat Enhanced Thematic Mapper (ETM+) data have been used for lithological and structural mapping in the central Côte D'ivoire, western Africa (Allou et al. 2015). Mwaniki et al. (*2015a*) are using the remote sensing techniques to compare the ability of Landsats ETM$^+$ and OLI in mapping geology and visualizing liniments. ASTER data were processed and evaluated by Lawrence and John (*2003*) to detect the lithological units in the mountain pass, California.

According to the satellite data, every multispectral band carries a specific energy that reflects information from the earth surface, and thus remote sensing images interpretations are based on color, textures, and spectral signatures to discriminate the different elements and contacts forming rocks and deposits (Mwaniki et al. 2015a). Satellite images enhancement processing gives new detailed information images from the highly correlated bands that comprise most of the geological information and take a small part of the electromagnetic spectral range (Abdeen and Abdelghaffar 2008).

Mapping of tectonic elements and trends are important tasks that reflect the architecture of the underlying rock basement (Ramli et al. 2010). Marghany and Hashim (2010) state that structural lineaments extraction may be done by either

manual visualization or automatic extraction using some commercial and open source software.

In this chapter, we explore combinations of the band obtained through the Principle and Independent Component Analysis (PCA and ICA) and Maximum Noise Fraction Analysis (MNFA) of the OLI data for lithological and tectonic mapping. Based on the analyses of the results, we report optimal band combinations for this purpose and update the geological and tectonic map of the Adıyaman Fault zone providing a more detailed map of rock units and morphological features.

6.2 Geological Setting

The study area is located along the Left lateral strike-slip Adıyaman Fault that extends ~ 75 km trending 65°NE south of the East Anatolian Fault zone in Eastern Turkey (Figure 6.1). Şengör et al. (1985) suggested that the Adıyaman Fault could have been initiated at the same time as the East Anatolian Fault, which is Late Miocene-early Pliocene.
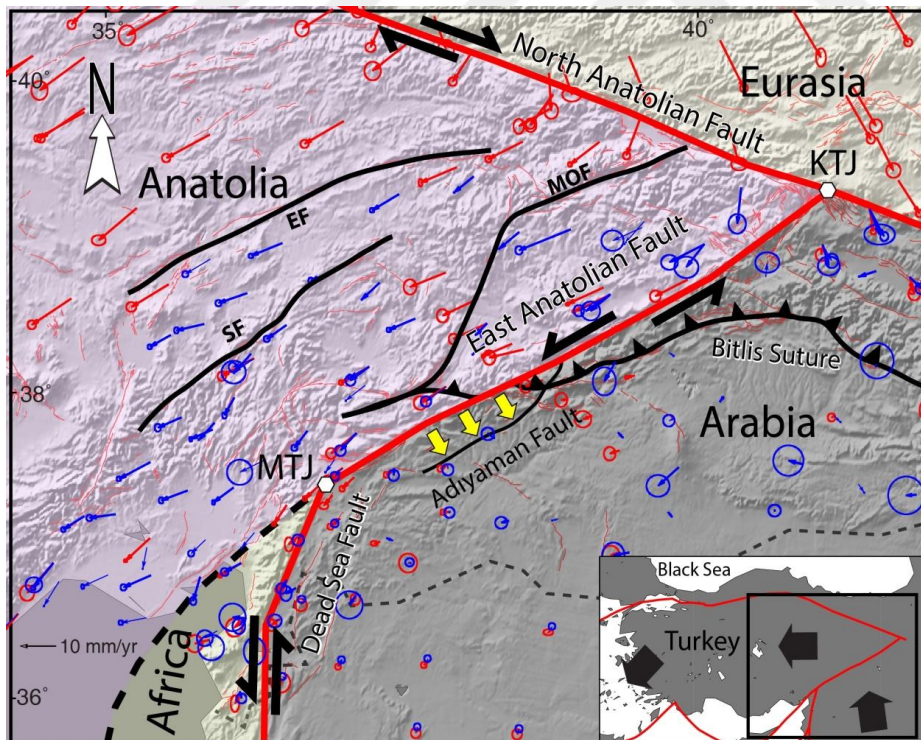
Figure 6.1 : Shaded relief image (data from SRTM-30; Farr et al. 2007) of eastern Turkey showing the African, Arabian, Anatolian and Eurasian lithospheric plates and major active Faults (thick black and red lines). The yellow arrows show the Adıyaman Fault. Abbreviations: MTJ, Maraş triple junction; KTJ, Karliova triple junction; EF, Ecemiş Fault; SF, Savrun Fault; OF, Ovacık Fault.

In the southern part of the Adıyaman Fault, two-thirds of the area, Middle-Upper Miocene, continental clastic rocks, and Plio-Quaternary undifferentiated materials are dominant, where as they cover around one-third of the area of the northern part of the Adıyaman Fault (Figure 6.2a). The Middle Triassic to Cretaceous volcanic and sedimentary rocks are dominant in the northern part of the Adıyaman Fault that covers at least one-third of that part which intruded by elongated body of Upper Cretaceous ophiolitic mélange (Figure 6.2a). The Eocene Neritic Limestone is located in the northern part of the study area and represented by an elongated body parallel to the fault trace. The Eocene Neritic Limestone has located also in the northern east, northern west, southern east, southern west, and middle of the study area (Figure 2a). The Lower Eocene, Continental Clastic rocks with clastic and carbonate rocks of Upper Cretaceous-Paleocene and Upper Senonian respectively are representing by elongated thin bodies in the northern part of the fault, whereas the clastic and carbonate rocks are located in other parts of the study area (Figure 6.2a). The Cretaceous Pelagic Limestone is located in the western part of the studied area (Figure 6.2a). The rest of the rock units are located in small parts all over the study area (Figure 6.2a). Most of these lithologic units can be detected in standard color-infrared images (Figure 6.2a) and in decorrelation stretch image products because of their color and textural characteristics. Maximum lithological information is extracted from OLI data when spectral analysis and image interpretative analysis are used together.

6.3 Data

We use data acquired by the Landsat 8 satellite that measures and records the reflected and emitted Electromagnetic Radiation (EMR) images of the earth with a 16- day repeat cycle, referenced to the worldwide reference system-2. The Landsat 8 has two sensors on board; operational land imager (OLI) and Thermal Infrared sensors (TIRS). OLI data consists of 11 spectral bands 8 multispectral, 1 panchromatic, and 2 thermal bands with 30, 15, and 100 m spatial resolution, respectively. The multispectral and panchromatic wavelength regions offer complementary data for lithological mapping. Here we resample 30-m-resolution OLI bands (1-7, and 9) down to 15 m equivalent to the resolution of the panchromatic band 8. The 15-m resolution panchromatic band 8 and 8 multispectral bands were combined to form 9-band 15 m spatial resolution data set.
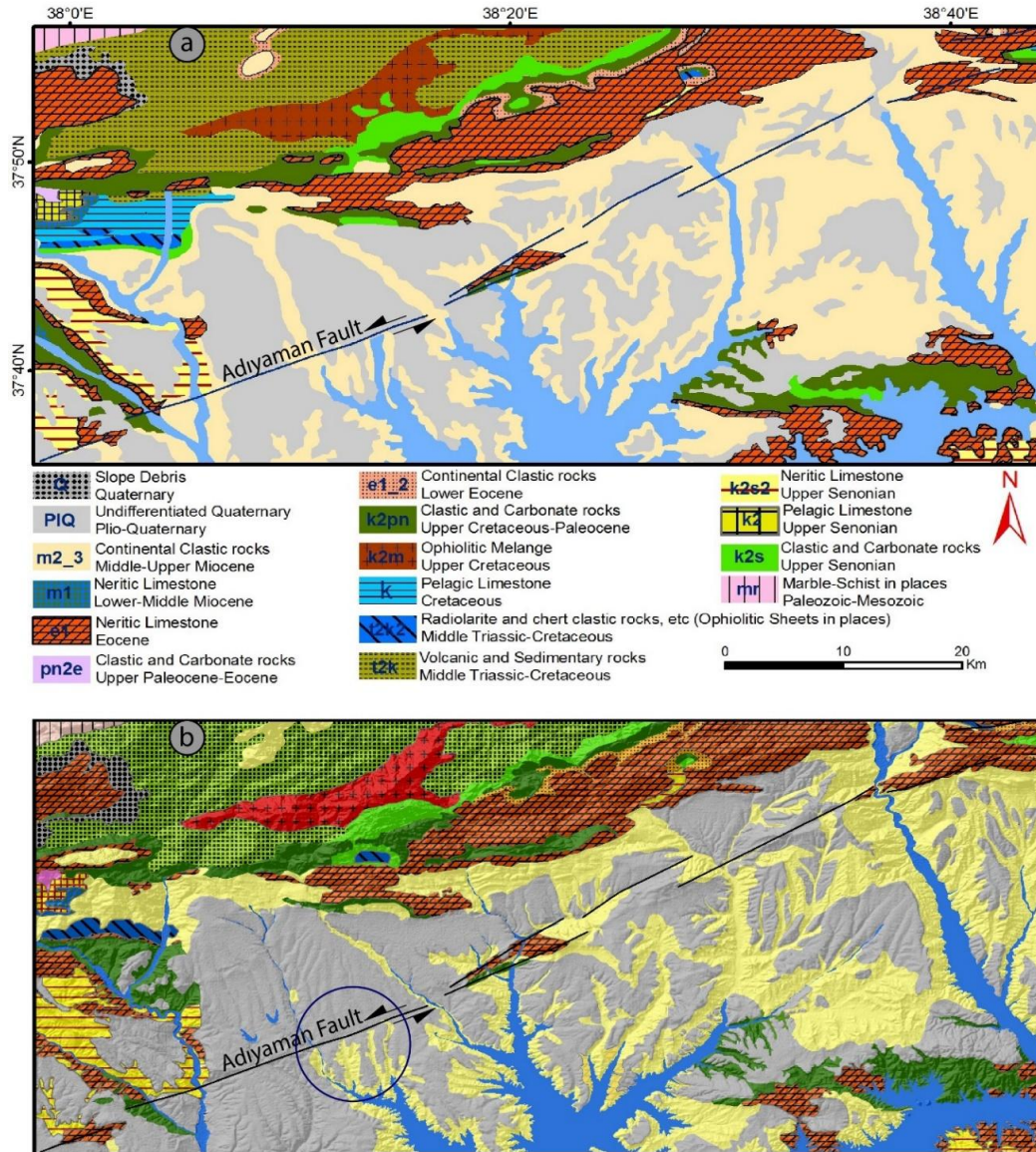
Figure 6.2 : (a) Lithologic map of the Adıyaman Fault zone (from Herece, 2008). (b) Refined lithological map obtained in this study. The blue circle indicates the region where offset river channels are revealed by the new map. Note the difference between the two maps; in the new map, formation contacts are refined and some outcrops are found to be missing in the published geology map.

In this chapter, the cloud-free Landsat 8 scene (path 173 / row 34) recorded on 10 September 2016 is processed. The data were pre-georeferenced to WGS 84 datum with UTM 37 North zone. The metadata file is essential to pre-processing procedures that are using to gain spatially and radiometrically corrected images to be ready for analyzing and comparing spectral data. The Fast Line-of-sight Atmospheric Analysis of Spectral Hypercubes (FLAASH) atmospheric correction model was applied to calibrate the surface reflectance in order to remove the atmospheric attenuations and have reflectance imagery (Zhang et al. 2016). FLAASH technique is a standard

method to compensate the error but the data have some residual errors that affect the geological information products accuracy (Mars and Rowan 2010; Hewson and Cudahy 201).

6.4 Methodology

We use the Principle and Independent Component Analysis (PCA and ICA) techniques to produce enhanced contrast images in a False Color Composite (FCC). PCA and ICA methods are very helpful to identify a smaller number of uncorrelated variables from a large set of data (Amer et al. 2010). It is applied to give uncorrelated output different bands and detect noise components. This is done by detecting a new data set orthogonal axes. This set of data has their origin at the data mean and that is rotated thus the data variance is maximized (Amer et al. 2010). The output of the Principal Component (PCA) bands of the same number could be calculated as input spectral number (Amer et al. 2010). Kumar et al. (2015) applied the Principle and Independent Component Analysis, in addition to Minimum Noise Fraction Analysis techniques in lithological discrimination using ASTER data in western India. They used PCA 213, ICA 231, and MNFA 213 band combinations for lithological mapping. Mwaniki et al. (2015a) used the Principle and Independent Component Analysis (PCA and ICA) to compare between Landsat 8 and Landsat 7 in mapping geology and lineaments visualization in central Kenya. The final conclusions of Mwaniki et al. (2015a) demonstrate that the false color composite (IC1, PC5, saturation band (573)) and band ratio combination (3/2, 5/1, 7/3) of Landsat 7 are the study tools for geological units and lineaments explorations. Gurugnanam et al. (2017) proposed PCA (RGB 213), ICA (RGB 312), and MNFA (RGB 432) as the best ASTER band combinations effectiveness of lithological mapping in Dindigul district, India.

As expected, according to the PCA bands data variance we obtained, PCA band 1 has the largest amount of data variance and the amount of data variance decreases gradually with the PCA bands till the last PCA bands (PCA bands 6 and 7) that appear noisy because they cover very few amounts of data variance, much of which due to noise in the original data. Depending on the ICA bands data, the first ICA band covers the largest amount of geological information while the last ICA bands show noisy images because they carry very little data variance.

The second method we use is the Minimum Noise Fraction Analysis (MNFA) which is a technique for hyperspectral imagery denoising using a linear transformation with two different steps: (1) Use the noise covariance matrix in order to rescale and decorrelate the noise in the processing data (Green et al. 1988; Lee et al. 1990; Bjorgan and Randeberg 2015; Nielsen 2011). In this manner, the noise has unit variance and no and-to-band correlations, and (2) perform a standard PCA transform to the data noise (Luo et al. 2016). The MNFA technique is a variation of the principal component analysis (PCA) steps, created to minimum spatially incoherent noise to higher bands that can be excluded from the next processing analysis (Green et al. 1988; Hubbard and Crowley 2005). In addition to applying MNFA for spectral endmember selection, the dimensionality information of remote sensing data could be examined by MNFA processing as well (Hubbard and Crowley 2005). The largest percentage of the data variance is recorded in the first MNFA band and the second MNFA band has the second largest amount data variance, and so on.

6.5 Results and Discussion

6.5.1 Landsat 8 Principle and Independent Component Analysis

Interpretation of transformed data through techniques such as PCA and ICA, provide detailed band information while separating data along new component can be analyzed by visualizing the new FCC components (Mwaniki et al. 2015b). From the result of PCA 7-bands analysis, we detected two sets of PCA band combination 134 and 231 for best discrimination between Pre-Miocene and Post-Miocene rocks. The geologic interpretations of OLI PCA bands indicate that the different lithologic units and the boundaries between them can be better identified. PCA band combinations show obvious contacts between the different lithologic units.

In PCA RGB-134 image (Figure 6.3), the Eocene Neritic limestone is well detected from the adjacent rocks by light green color, undifferentiated Quaternary units have yellowish green color, volcanic and sedimentary rocks have pale violet color, and ophiolitic mélange has a violet color. In PCA RGB-231 image (Figure 6.4), the Eocene, Neritic limestone is characteristic by blue color, undifferentiated Quaternary units have very obvious light green color, volcanic and sedimentary rocks have greenish blue color, and ophiolitic mélange has a dark pink color. From the

processing ICA 7-bands, we conclude that the RGB-231 band combination gives the best image to differentiate the Miocene rock units.

In PCA RGB-134 image (Figure 6.3), the Eocene Neritic limestone is well detected from the adjacent rocks by light green color, undifferentiated Quaternary units have yellowish green color, volcanic and sedimentary rocks have pale violet color, and ophiolitic mélange has a violet color. In PCA RGB-231 image (Figure 6.4), the Eocene, Neritic limestone is characteristic by blue color, undifferentiated Quaternary units have very obvious light green color, volcanic and sedimentary rocks have greenish blue color, and ophiolitic mélange has a dark pink color. From the processing ICA 7-bands, we conclude that the RGB-231 band combination gives the best image to differentiate the Miocene rock units.

Figure 6.3 : Landsat 8 Principle Component Analysis RGB-134 image. Areas of settlements are defined by yellow polygons.

In the ICA RGB-132 image (Figure 6.5), the Neritic Limestone of Eocene age is characterized by a greenish red color, undifferentiated Quaternary units are well outlined with obvious a yellow color, volcanic and sedimentary rocks have a light green color, and ophiolitic mélange unit is shown by a dark green color.

6.5.2 Landsat 8 Minimum Noise Fraction Analysis

Our analysis of the MNFA bands shows that RGB-521 band combination is the best one for discriminating between the different lithologic units of the study area. MNFA band 1 alone provides the best image to trace the tectonic and structural elements in the study region.
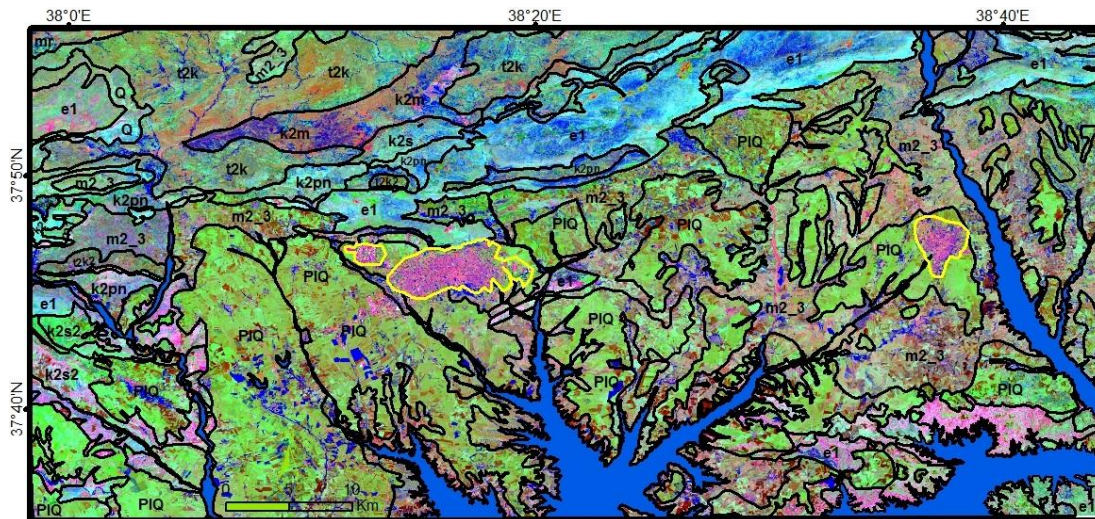
Figure 6.4 : Landsat 8 Principle Component Analysis RGB-231 image.
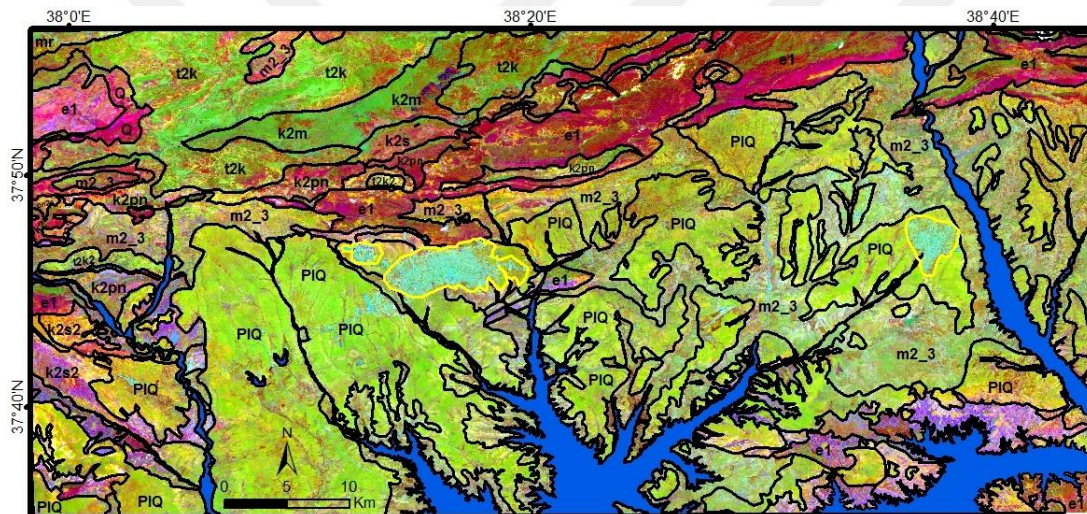
Figure 6.5 : Landsat 8 Independent Component Analysis RGB-132 image.

The geologic interpretation of MNFA RGB-521 image (Figure 6.6), suggests that undifferentiated Quaternary units are detected by sharp pink color with coarse crystalline texture, Middle-upper Miocene continental clastic rocks by light yellowish pink, the volcanic and sedimentary units by greenish pink, and the ophiolitic mélange by light violet color.
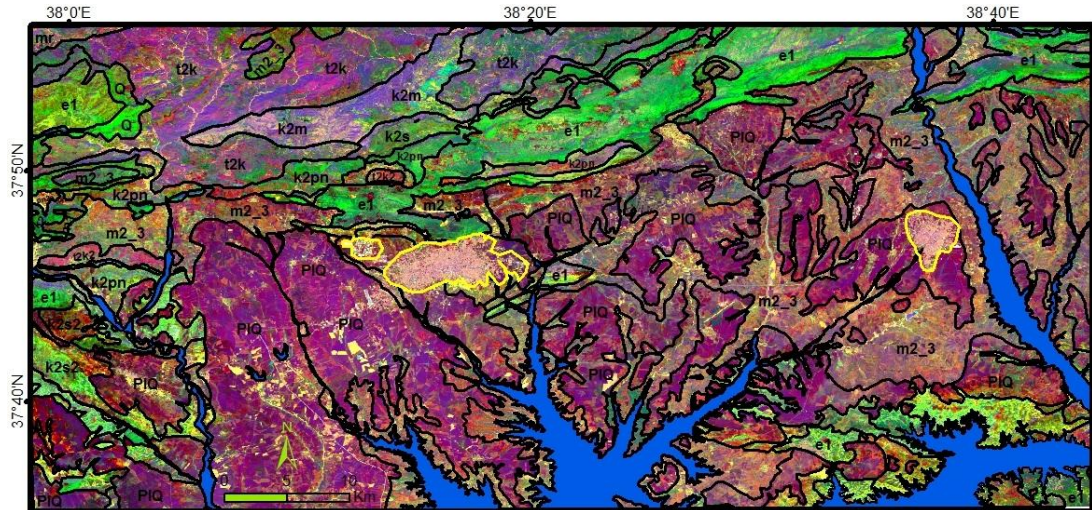
Figure 6.6 : Landsat 8 Minimum Noise Fraction RGB-521 image, settlements areas are defined by yellow polygons.

The results show that the first four high order principles components and minimum noise fraction analysis (1, 2, 3 and 4) have over 99 % of spectral information; so it is generally accepted that these have been widely used for lithological mapping rather than the low order principles components and minimum noise fraction analysis (5, 6, 7, etc.) that usually contain low signal-to-noise ratios. The principal component and minimum noise higher order give good information about the occurrence of rock types that are dominant in the map image. Therefore, sometimes it is worthwhile to apply a combination of certain lower order that covers some of the information with a higher order to detect and highlight some target spectral signatures. In this article, the lowest order MNFA 5 minimum noise in addition to higher order MNFA 1st and 2nd minimum fraction noise give the signal to discriminate the dominant rock types in the study area (Figure 6.6). Totally, PCA, ICA, and MNFA are statistics-based and results may vary in the same area with different geographic sizes.

6.5.3 Improvements of the available geological map

Our new map shows differences in the distribution of some rock units and boundaries between them compared to the published geological map ((Herece 2008; Figures 6.2a and b). The most obvious differences are the discrimination between the Eocene, neritic limestone, Middle-Upper Miocene, Continental clastic rocks, and Undifferentiated Quaternary units. In the southeastern part, the new map defined Pli-Quaternary unit instead of Eocene neritic limestone (Figures. 6.2a and b). In the west, the results replaced the Middle-Upper Miocene continental clastic rocks by

Upper Cretaceous-Paleocene clastic carbonate rocks (Figures 6.2a and b). The resulted images could not detect the contact between the radiolarite with chert clastic and units. The appearance of the pelagic limestone is similar to the Middle-upper Miocene rocks, thus the study mapped them as the same continental clastic unit (Figures 6.2a and b).

6.5.4 Extracted tectonic map

The tectonic elements are extracted manually from MNF first band as it reveals the geological structures the best. The Adıyaman Fault is the main tectonic element along the study region can be precisely traced. Most of structural lineaments and roads over the Adıyaman Fault region were mapped. Referring to Herece (2008) geological map, the traces of reverse and thrust faults located along the northeast, north, and northwest parts of the region, were refined (Figure 6.7). From the MNFA band 1 it is easy to notice and detect some settlements areas along the fault trace.

6.6 Conclusion

In this chapter, the Landsat OLI data are processed using the Principle and Independent Component Analysis and the Minimum Noise Fraction Analysis to map the pre- and post-Miocene rocks along the Adıyaman Fault zone. The results demonstrate that PCA 134 and 231, ICA 132, and MNFA 521 are the band combinations of the Landsat OLI data that provide the best images for mapping lithologic rock units and therefore, can be used as time- and cost-effective approach for mapping in the tectonically active regions elsewhere in the world. Morphology of the Adıyaman Fault is better revealed by the MNFA band 1. The MNFA 521 band combination appears to be the best combination to map alluvial deposits with high accuracy. As can be seen in Fig. 2b, the new map shows in details the contacts and distribution of undifferentiated Quaternary clastic rocks along the Adıyaman Fault compared to the available geological map (Herece, 2008).

The map reveals the presence of offset river channels along the Adıyaman Fault at around 38.15E longitude where there the river channels do not cross the fault to the north but stop right at the fault line, implying that these channels have been recursively offset by the fault and thus the Adıyaman Fault is a Quaternary active fault.
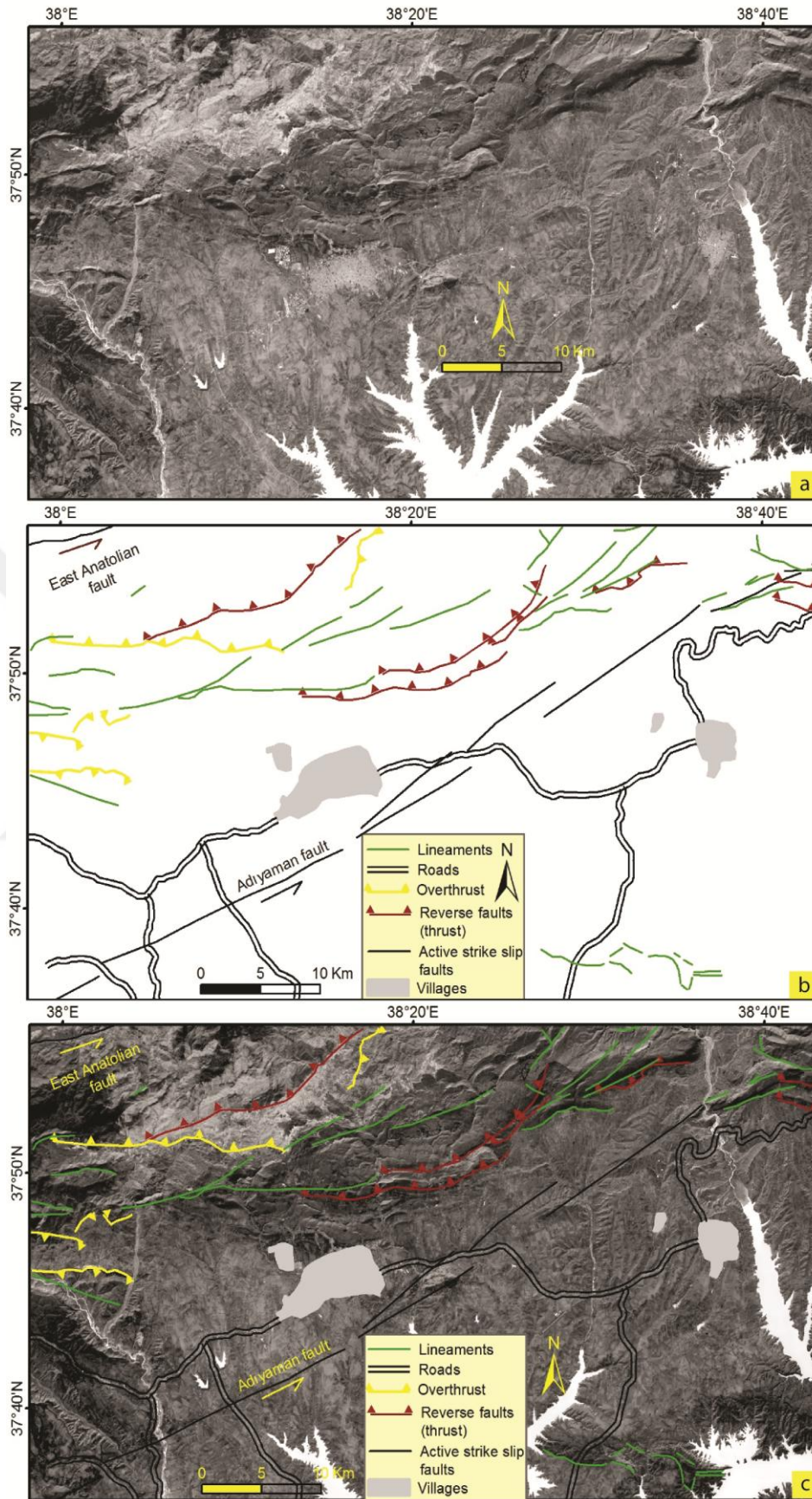
Figure 6.7 : a Landsat 8 Landsat 8 MNFA band 1. **b** Tectonic map of the study region. **c** Tectonic map layer over MNF band 1.

In addition to the refinement of all the boundaries of rock formations, our study reveals various outcrops that are missing in the geological map of Herece (2008), particularly to the southern and western parts of the Adıyaman Fault zone.

7. CONCLUSIONS

Improving our active tectonics understanding and updating the published maps along the fault zones requires precise analysis and processing of deformations related to active fault zones. Applying tectonic geomorphology analysis and remote sensing processing over high-resolution data in active regions is a very useful tool to evaluate the relative tectonic activity, examine and refine the different maps, and give an initial view about the seismic hazards along the active zones. In this thesis, we have used the most important morphotectonic indexes (e.g. mountain front sinuosity (Smf), Valley floor-width to valley-height ratio (Vf), stream length-gradient index (SL), basin asymmetry factor (AF), drainage density (Dd), and hypsometry analysis (Hi and H_{curves}) in addition to analysis the ASTER and Landsat satellite data along major and minor active faults (East Anatolian Fault (EAF) and Adıyaman Fault (AdF) within the Anatolian-Arabian deformation zones. The morphotectonic analysis is very useful to examine the relative tectonic activity and effect of the long-term deformations along the East Anatolian Fault zone. They also help in evaluating the degree of tectonic activity and assessment of seismic hazard along the Adıyaman Fault zone. The remote sensing methods such as band ratio composite and principle and independent component analysis are found to be very helpful to discriminate the different rock units, update the geological offsets, and trace the various structural elements along the EAF and AdF.

In this study, different geomorphic indices are applied for the first time along the EAF to gain deeper insights into morphotectonic evolution and activity of the EAF. According to the results of the various morphotectonic analyses, we suggest that each segment along the fault is presently very active. The nearly uniform range of geomorphic indices along the entire length of the fault suggests that development of the EAF was essentially coeval along its length. Examinations of all catchments geomorphic indexes that are related to the trace of the faults can present valuable data on the tectonic behaviors and landscape evolution. Thus, this can be applied to other major Active faults elsewhere, especially to those whose cumulative offset and slip rates are not well defined.

We extracted clear results from ASTER image processing that are consistent with the published Herece (2008)'s geological map on a large scale. The combining a high-resolution ASTER data with other field information is very positive and appropriate for detailed lithological and tectonic purposes. The newly developed ASTER band ratio methods are a strong tool for lithological mapping and checking the recorded geological offsets along the Erkenek Segment of the EAF. The ASTER band ratios detected the geological offsets as 22 km along the Erkenek Segment. The new band ratio images help us to distinguish between various rock units and formations of pre-Miocene age. Thus, it is recommended for detailed lithological mapping and offsets along other deformation zones. The thesis suggests ASTER image enhancement techniques as time- and cost-effective methods for detailed lithological mapping along the active regions.

The quantitative geomorphic analysis was applied for the first time along the AdF and confirmed that the different results are categorized into three classes of relative tectonic activity (RTA) based on Gav values. According to the RTA results, Adıyaman Fault presents moderately to highly active levels, classes 2 and 3. The thesis recommends more detailed tectonic studies along the central and western parts of the fault to improve our understanding and evaluate the regional seismic hazard. The RTA results suggest that the Adıyaman Fault in secondary seismic importance after the East Anatolian Fault that represents the plate boundary between the Arabian and Anatolian plates.

The Principle and Independent Component Analysis and the Minimum Noise Fraction Analysis are applied to the Landsat 8 data to discriminate the different rock units along the Adıyaman Fault zone. The Landsat OLI results include PCA 134 and 231, ICA 132, and MNFA 521 presents the best images for mapping lithologic rock units and therefore, can be used as time- and cost-effective approach for mapping in the active tectonic regions elsewhere around the world. Morphology along the Adıyaman Fault is better revealed by the MNFA band 1. The MNFA 521 band combination appears to be the best combination to map alluvial deposits with high accuracy. The new lithological map shows in details the distribution of undifferentiated Quaternary clastic rocks along the compared to the available geological map (Herece 2008). The map presents the of offset river channels along the Adıyaman Fault at around 38.15E longitude where there the river channels do not

cut the fault to the north but they stop right at the fault line, implying that these channels have been recursively offset by the fault and thus the Adıyaman Fault is a Quaternary active fault.

This thesis shows once again that tectonic geomorphology and remote sensing applications are remarkably very useful and powerful techniques in evaluating active tectonics and detecting some deformation features, especially along the different active regions. This study shows different tectonic signals and evaluates one geological offset along the East Anatolian Fault. In this work also, we give a very useful preliminary view about the degree of tectonics and rivers displacements along the Adıyaman Fault with the Arabian-Anatolian deformation zone.

The general conclusions are summarized as follow:

1- Examining five segments of the EAF using the morphotectonic analysis confirms its high relative tectonic activity.

2- Uniformity of morphotectonic indices along the EAF supports the opinion that the development along the EAF was coeval along its the entire length.

3- Updated geology of along the Erkenek segment using remote sensing techniques provides better constraints to the total offset of the fault which is found to be about 22 km.

4- Morphotectonic analysis along the AdF shows that the fault reflects activity from medium to high.

5- Analysis of Landsat 8 satellite images using PCA, ICA, and MNF techniques shows that the MNF band 1 is the best technique for extracting and tracing the tectonic elements, PCA, and ICA for geological mapping.

Although the tectonic geomorphology and remote sensing applications give very valuable information, they may not be sufficient to gain a complete view of the tectonic regions. Thus, some of the future works we think are worthwhile to do are as follow:

1- Applying the morphotectonic analysis on one different major strike-slip fault such as North Anatolian Fault to examine and compare the results from the different strike-slip faults.

2- Depending on the primary results along the AdF, more active tectonic measurements and analysis may be necessary for better understanding and evaluating along the AdF.

3- Comparing between the results of the different types of satellite images along the active zones to mark the best satellite data and techniques to study the surface deformations.

REFERENCES

Abdeen, M.M., Allison, T.K., Abdelsalam, M.G., and Stern, R.J. (2001). Application of ASTER band-ratio images for geological mapping in arid regions; the Neoproterozoic Allaqi Suture, Egypt. *Annual meeting of Geological Society of America (Abstract)*, Boston, Massachusetts, November 5–8, p. 289.

Abrams, M. J., Brown, D., Lepley, L., and Sadowski, R. (1983). Remote sensing for porphyry copper deposits in southern Arizona. *Economic Geology*, *78*, 591–604.

Acernese, F., and Ciaramella, A.M.S. (2003). Neural networks for blind-source separation of Stromboli explosion quakes. *IEEE Trans. Neural Netw.* *14* (1), 167–175.

Aksoy E, İnceöz M, and Koçyiğit, A. (2007). Lake Hazar Basin: a negative flower structure on the East Anatolian Fault System (EAFS), SE Turkey. *Turkish Journal of Earth Sciences, 16*: 319-338.

Aktuğ B, Özener H, Dogru A, Sabuncu A, Turgut B, Halicioglu K, Yilmaz O, and Havazli, E. (2016). Slip rates and seismic potential on the East Anatolian Fault System using an improved GPS velocity field. *J Geodynamics 94–95*:1-12.

Alipoor R, Poorkermani M, Zare M, and El Hamdouni, R. (2011). Active tectonic assessment around Rudbar Lorestan dam site, High Zagros Belt (SW of Iran). *Geomorphology, 128*: 1-14.

Allen, C.R. (1969). Active Faulting in Northern Turkey. *Division of Geological Sciences*, California Institute of Technology, USA, 1577.

Allou, G., Ouattara, G., Coulibaly, Y., and Bonin, B. (2015). The Landsat 7 ETM+ remote sensing imagery for lithological and structural mapping in the central Côte D'ivoire (western Africa): case of Dabakala area. *European Scientific Journal*, *11*, 141–163.

Ambraseys, N.N. (1965). The seismic history of Cyprus. Rev. Union Int. Secours, *Geneva, 3*:25-48.

Ambraseys, N.N. 1970. Some characteristic features of the North Anatolian Fault Zone, *Tectonophysics, 9*:143- 165.

Ambraseys, N.N. (1988). Temporary seismic quiescence: SE Turkey. *Geophys J Int*, *96*: 311-331.

Ambraseys, N.N., and Jackson, J.A. (1998). Faulting associated with historical and recent earthquakes in the Eastern Mediterranean region. *Geophys J Int*, *133*: 390-406.

Amer, R., Kusky, T., and Gullam, A. (2010). Lithological mapping in the Central Eastern Desert of Egypt using ASTER data. *Journal of African Earth Sciences, 56*, 75–82.

Arger, J, Milcheli J, and Westaway, R. (1996). Neogene and Quaternary volcanism of eastern Turkey: Potassium-Argon dating and its tectonic implications. Technoscience. Newcastle upon Tyne. UK. *Open-file Science Reports.* 1996/1.

Arger, J., Mitchell J, and Westaway, R. (2000). Neogene and Quaternary volcanism of south-eastern Turkey, in Bozkurt E., Winchester J.A., Piper J.D.A. (Eds.), Tectonics and magmatism in Turkey and the Surrounding Area, *Geological Society Special Publication no. 173, Geological Society,* London, pp. 459- 487.

Armijo, R., Meyer B., Barka A.A., and Hubert, A. (1999). Propagation of the North Anatolian fault into the Northern Aegean: timing and kinematics, *Geology 27*: 267- 270.

Arpat, A.E. (1971). 22 Mayıs, 1971 Bingöl Depremi-Ön Rapor. *Institute of Mineral Research and Exploration Report 4697*.

Arpat, E, and Şaroğlu, F. (1972). The East Anatolian Fault System: thoughts on its development. *Bulletin of the Mineral Research and Exploration (MTA) 78*: 33-39.

Arpat, E, and Şaroğlu F (1975) Türkiye'deki bazı önemli genc ̧ tektonik olaylar (Recent tectonic activities in Turkey). *Bulletin of the Geological Society of Turkey 18*: 91-101 (in Turkish with English abstract).

Azañón, J.M., Pérez-Peña1 J.V., Giaconia F., Booth-Rea1 G., Martínez-Martínez J.M., Rodríguez-Peces M.J. (2012). Active tectonics in the central and eastern Betic Cordillera through morphotectonic analysis: the case of Sierra Nevada and Sierra Alhamilla. *J Iber Geol 38 (1)*: 225-238.

Azor, A, Keller, E.A., and Yeats, R.S. (2002). Geomorphic indicators of active fold growth: South Mountain-Oak Ridge anticline, Ventura basin, southern California. *Geol Soc Am Bull 114*: 745-753.

Bandel K. and Khouri H., (1981). Lithostratigraphy of the Triassic of Jordan, *Facies, 4*, 1–23.

Barka, A.A. (1992). The North Anatolian Fault zone, *Annales Tecton. 6*, 164-195.

Barka, A.A., and Eyidoğan H. (1993). The March 13, 1992, Erzincan earthquake, *Terra Nova 5*: 190- 194.

Barka, A.A., and Kadinsky-Cade, K. (1988). Strike-slip fault geometry in Turkey and its influence on earthquake activity. *Tectonics 7*: 663-684.

Barka A.A., Toksöz M.N., Gülen L., and Kadinsky-Cade K. (1987). Segmentation, seismicity and earthquake potential of the eastern

section of the North Anatolian Fault Zone, Hacettepe Univ. *Earth Sci. 14*: 337- 352 (in Turkish with English abstract).

Barka, A.A., Şaroğlu, F., and Güner, Y. (1983). Horasan- Narman depremi ve bu depremin Dogu Anadolu neotektonigindeki yeri, *Yeryuvan ve insan, 8*, 16-20 (in Turkish with English abstract).

Barka A.A., and Reilinger R. (1997). Active tectonics of the Mediterranean region: deduced from GPS, neotectonic and seismicity data, *Annali di Geophis. XI*, 587–610.

Bedell, R.L. (2001). Geological mapping with ASTER satellite: new global satellite data that is a significant leap in remote sensing geologic and alteration mapping. Special Publications, *Geological Society of Nevada, 33*, 329–334.

Bjorgan, A., and Randeberg, L.L. (2015). Real-time noise removal for line-scanning hyperspectral devices using a minimum noise fraction–based approach. *Sensors, 15*, 3362–3378.

Boardman, J.W., and Kruse, F.A., (1994). Automated spectral analysis: A geological example using AVIRIS data, northern Grapevine Mountains, Nevada: in Proceedings, Tenth Thematic Conference, Geologic Remote Sensing, 9-12 May 1994, San Antonio, Texas, p. I-407 - I-418

Bozkurt, E. (2001). Neotectonics of Turkey – a synthesis. *Geodinamica Acta, 14*, 3-30.

Bozkurt, E., and Koçyiğit, A. (1996). The Kazova basin: an active negati ve flower structure on the Almus Fault Zone, a splay fault system of the North Anatolian Fault Zone, Turkey, *Tectonophysics 265*:239- 254.

Bull, W.B., (1977). The alluvial fan environment. *Prog Phys Geog 1*:22-270.

Bull, W.B., and McFadden, L.D. (1977). Tectonic geomorphology north and south of the Garlock fault, California. In: Doehering O, editor. Geomorphology in Arid Regions. *The 8th Annual Geomorphology Symposium Proceedings.* State University of New York, Binghamton NY, pp. 115-138.

Bull, W.B. (2007). *Tectonic Geomorphology of Mountains: A New Approach to Paleoseismology.* USA, Wiley - Blackwell, 328pp.

Bulut, F., Bohnhoff, M., Eken, T., Janssen C., Kiliç T., and Dresen, G. (2012). The East Anatolian Fault Zone: Seismotectonic setting and spatiotemporal characteristics of seismicity based on precise earthquake locations. *J Geophys Res 117*: 1-16.

Canıtez, N., and Üçer, B. (1967). A catalog of focal mechanism diagrams for Turkey and adjoining areas, *Publication no. 25, Istanbul Technical University*, Istanbul.

Cardoso, J. (1998). Blind signal separation: statistical principles. Proc. *IEEE 86 (10)*, 2009–2025.

Castelltort, S., Goren, l., Willett, S., Champagnac, J., Herman, F., Braun, J. (2012). River drainage patterns in the New Zealand Alps primarily controlled by plate tectonic strain. *Nat Geosci 16*: 1-5.

Chavez, P.S., Berlin, G.L., and Sowers, L.B. (1982). Statistical methods for selecting of Landsat MSS ratios. *Journal of Applied Photographic Engineering, 8*, 30–32.

Chen, Y., Sung, Q., and Cheng, K. (2003). Along-strike variations of morpho-tectonics features in the Western Foothills of Taiwan: tectonic implications based on stream-gradient and hypsometric analysis. *Geomorphology, 56*: 109-137.

Chen, C., and Zhang, X. (1999). Independent component analysis for remote sensing study. *Remote Sens. 3871*: 150–158.

Chorowicz, J., Luxey, P., Lyreris, N., Carvalho, J., Pakroi, J.F., Yurur, T., and Gindodi, N. (1994). The Maraş triple junction (southern Turkey) based on digital elevation model and satellite Imagery interpretation. *J Geophys Res, 99*: 20225-20242.

Çetin, H., Güneyli, H., Mayer, L. (2003). Paleoseismology of the Palu-Lake Hazar segment of the East Anatolian Fault Zone, Turkey. *Tectonophysics, 374*: 163-197.

Comon, P. (1994). Independent component analysis, a new concept. *Signal Process. 24*, 287–314.

Crampin, S., Evans, R. (1986). Neotectonics of the Marmara Sea region of Turkey, *J. Geol. Soc., London, 143*: 343-346.

D'Alessandro, L., Del Monte, M., Fredi, P., Lupia-Palmeri, E., and Peppoloni, S. (1999). Hypsometric analysis in the study of Italian drainage basin morph evolution. *Transactions, Japanese Geomorphological Union, 20*: 187-202.

Davis, J.C. (2002). *Statistics and Data Analysis in Geology*, third ed. New York, John Wiley, and Sons, 656pp.

Dewey, J.F., Hempton, M.R., Kidd, W.S.F., Şaroglu, F., Şengör, A.M.C. (1986). Shortening of continental lithosphere: the neotectonics of Eastern Anatolia - a young collision zone. In: Coward MP, Ries AC, editors. Collision Tectonics. *Geol Soc London Spec Pub.,l 19*: 3-36.

Dewey, J.F., Pitman W.C., Ryan W.B .F., and Bonnin J. (1973). Plate tectonics and evolution of the Alpine system, *Geol. Soc. Am. Bull.* 3137-3180.

Dewey, J.F., and Şengör A.M.C. (1979) Aegean and surrounding regions: complex multiple and continuum tectonics in a convergent zone, *Geol. Soc. Am. Bull. 90*: 84-92.

Dubertet, L. (1966). Syrie et Bordure des pays voisins. Extrait des notes et mémoires sur le Moyen-Orient, tome VIII, *Museum National d'Histoire Naturelle,* Paris, 251–358.

Duman, **T.Y., and Emre, Ö.** (2013). The East Anatolian Fault: geometry segmentation and jog characteristics. *Geol Soc London Spec Publ 372*: 495-529.

Dumont, J.F., Santana, E., and Vilema, W. (2005). Morphologic evidence of active motion of the Zambapala fault, gulf of Guayaquil (Ecuador). *Geomorphology, 6:* 223–239.

El Hamdouni, R., Irigaray, C., Fernandez, T., Chacón, J., Keller, E.A. (2008). Assessment of relative active tectonics, southwest border of Sierra Nevada (southern Spain). *Geomorphology, 96*: 150-173.

Emre, Ö., Duman, T.Y., Özalp, S., Elmaci, H., Olgun, Ş., and Şaroğlu, F. (2013). Active fault map of Turkey with an explanatory text. *General Directorate of Mineral Research and Exploration (MTA)*, ISBN: 978-605-5310-56-1.

Eyal M., Eyal Y., Bartov Y., Steinitz G. (1981). The tectonic development of the western margin of the Gulf of Elat (Aqaba) rift, *Tectonophysics, 80*: 135–146.

Eyidoğan, H., Nalbant, S.S., Barka, A.A., and King, G.C.P. (1999). Static stress changes induced by the 1924 Pasinler (M=6.8) and 1983 Horasan-Narrnan (M=6.8) earthquakes, Northeastern Turkey. *Terra Nova,* 38-44.

Farr, T.G., Rosen, P.A., Caro, E., Crippen, R., Duren, R., Hensley, S., Kobrick, M., Paller, M., Rodrigue, Z.E., Roth, L., et al. (2007). The shuttle radar topography mission. *Rev Geophys, 45*: 1-33.

Fielding, E.J., Lundgren, P.R., Taymaz, T., Yolsal-Çevikbilen, S., and Owen, S.E. (2013). Fault-slip source models for the 2011 M7.1 Van earthquake in Turkey from SAR interferometry, pixel offset tracking, GPS and seismic waveform analysis. *Seismological Research Letters, 84 (4)*, 579-593.

Frank, P., Claudio B., Ryan M., Kellen, G., and Alese, K. (2011). Tectonic geomorphology and EarthScope in Eastern North America. Abstract, *GSA Annual meeting in Minneapolis*, 9-12 October, *43*, 5, 363.

Freund R., Garfunfel Z., Zak I., Goldberg M., Weissbrod T., Berin B. (1970). The shear along the Dead Sea rift, *Philosophical Transactions of The Royal Society A Mathematical Physical and Engineering Sciences,* London, Series *A 267*, 107–130.

Fujisada, H. (1995). Design and performance of ASTER instrument. *Proceedings of SPIE, the International Society for Optical Engineering, 2583*, 16– 25.

Gad, S. and Kusky, T.M. (2006). Lithological mapping in the Eastern Desert of Egypt, the Barramiya area, using Landsat thematic mapper (TM). *Journal of African Earth Sciences, 44*: 196–202.

Gad, S., and Kusky, T.M. (2007). ASTER spectral ratioing for lithological mapping in the Arabian-Nubian shield, the Neoproterozoic Wadi Kid area, Sinai, Egypt. *Gondwana Research, 11 (3)*: 326–335.

Garcia, M.D., Hubert-Ferrari, A, Moernaut, J., Fraser, J.G., Boes, X., Van Daele, M., Avsar, U., Çağatay, N., and De Batist, M. (2010). Structure and recent evolution of the Hazar Basin: a strike-slip basin on the East Anatolian Fault, Eastern Turkey. *Basin Res 23:* 191-207.

Garfunkel Z., Zak I., Freund R. (1981). Active faulting in the Dead Sea rift, *Tectonophysics 8:,* 1–26.

Garfunkel Z. and Ben-Avraham Z. (1996). The structure of the Dead Sea basin, *Tectonophysics 255*: 155–176.

Giaconia, F., Booth-Rea, G., Martínez-Martínez, J.M., Azañón, J.M., and Pérez-Peña, J.V. (2012). Geomorphic analysis of the Sierra Cabrera, an active tectonicapop-up in the construction domain of conjugate strike-slip faults: The Palomares and Polopos fault zones (eastern Betics, SE Spain). *Tectonophysics, 580*: 27–42.

Giamboni, M., Wetzel, A., and Schneider, B. (2005). Geomorphic response of alluvial rivers to active tectonics: example from the southern Rhine Graben. *Australian Journal of Earth Sciences, 97*: 24-37.

Ghahramani, Z. (2004). Unsupervised learning. *Adv. Lect. Mach. Learn.* 72–112.

Glover, C., and Robertson, A.H.F. (1998). Neotectonic intersection of the Aegean and Cyprus tectonic arcs: extensional and strike-slip faulting in the Isparta Angle, SW Turkey, *Tectonophysics 298:*103-132

Gordon, R.G. (1998). The plate tectonic approximation: plate nonrigidity, diffuse plate boundaries, and global plate reconstructions. *Annual review of earth and planetary sciences, 26*: 615-642.

Görür, N., Cağatay, M.N., Sakınç, M., Sümengen, M., Şentürk, K., Yaltırak, C., and Tchapalyga, A. (1997). Origin of Sea of Marmara as deduced from Neogene to Quaternary paleogeographic evolution of its frame, *Inter. Geol. Rev. 39*: 342-352.

Green, A.A., Berman, M., Switzer, P., and Craig, M. D. (1988). A trans-formation for ordering multispectral data in terms of image quality with implications for noise removal. *IEEE Transactions on Geo-science and Remote Sensing, 26:* 65–74.

Gurugnanam, B., Arulbalaji, P., Midhuna, V., and Kumaravel, S. (2017). Lithological discrimination of Anorthosite using ASTER data in Oddancehatram area, Dindigul district, tamil Nadu, India. *International Journal of Advanced Engineering, Management and Science, 3*: 316–324.

Gülen, L., Barka, A.A. and Toksöz, M.N. (1987). Continental Collision and Related Complex Deformation; Maraş Triple Junction and Surrounding Structures in SE Turkey. *Hacettepe University, Special Publication*, Ankara

Gürsoy, Ö., Kaya, Ş., Çakır, Z., Tatar, O., and Canbaz, O. (2017). Determining lateral offsets of rocks along the eastern part of the North Anatolian Fault Zone (Turkey) using spectral classification of satellite images and field measurements. *Geomatics, natural, hazard, and risk, 8:* 13–25.

Hack, J.T. (1973). Stream profile analysis and stream-gradient index. *J Res US Geol Surv 1*: 421-429.

Hare, P.W., and Gardner, T.W. (1985). Geomorphic indicators of vertical neotectonism along converging plate margins, Nicoya Peninsula, Costa Rica. In: Morisawa, M., Hack, J.T. (Eds.), *Tectonic Geomorphology. Proceedings of the 15th Annual Binghamton Geomorphology Symposium.* Allen and Unwin, Boston, MA, pp. 123-134.

Hempton, M.R. (1985). Structure and deformation history of Bitlis suture near lake Hazar, southeastern Turkey. *Bull Geo Soc Am 96*: 233-243.

Hempton, M.R. (1987). Constraints on Arabian plate motion and extensional history of the Red Sea. Tectonics 6: 687-705.

Hempton, M.R., Dewey J.F., and Şaroğlu, F. (1981). The East Anatolian transform fault: along-strike variations in geometry and behavior. *Transactions, American Geophysical Union*, EOS 62, 393.

Herece, E. (2008). Atlas of the East Anatolian Fault, General Directorate of Mineral Research and Exploration (MTA), *Special Publication Series*, *13*: Ankara, Turkey.

Herece, E., and Akay, E. (1992). Karlıova-Çelikhan arasında Doğu Anadolu Fayı, Turkiye. Petrol Kongresi Bildirileri, (East Anatolian Fault between Karlıova and Çelikhane. *The 9th Petroleum Congress of Turkey Proceedings,* 17-21 February 1992, Ankara, Turkey, pp. 361-372.

Hewson, R. and Cudahy, T. (2010). *Issues Affecting Geological Mapping with ASTER Data: A Case Study of the Mt Fitton Area, South Australia*. In: Ramachandran, B., Justice, C.O., (eds.), Land Remote Sensing and Global Environmental Change, Vol. *11*: Series Remote Sensing and Digital Image Processing Springer, New York, 13, P. 273–300.

Hewson, R.D., Cudahy, T.J., and Huntington, J.F. (2001). Geologic and alteration mapping at Mt Fitton, South Australia, using ASTER satellite-borne data. *International Geosciences and Remote Sensing Symposium (Conference Paper)*, February, *2:* 724–726.

Horton, R.E. (1932). Drainage basin characteristics. *AGU publication*, *13*: 350 – 361.

Hubbard, B.E. and Crowley, J.K. (2005) Mineral mapping on the Chilean-Bolivian Altiplano using co-orbital ALI, ASTER and Hyperion imagery: Data dimensionality issues and solutions. *Remote Sensing of Environment*, *99:* 173–186.

Hubert-Ferrari, A., Barka, A.A., Jacques, E., Nalbant, S., Meyer, B., Armijo, R., Tapponier, P., King, J. (2000). Seismic hazard in the Marmara Sea region following the 17 August 1999 İzmit earthquake, in: Barka A.A., Kozact O., Akyüz S.H., Altunel E. (Eds.), 1999 İzmit and Düzce earthquakes: preliminary results, *Istanbul Technical University Pub.*, Istanbul, pp. 311 - 316.

Hubert-Ferrari A, King G, Vander Woerd J, Villa I, Altunel E, Armijo R (2009). Long-term evolution of the North Anatolian Fault: new constrains from its eastern termination. In: Van Hinsbergen DJJ, Edwards MA, Govers R, editors. Collision and Collapse at the Africa-Arabia-Eurasia Subduction Zone. *Geol Soc London Spec Publ 311*: 133-154.

Jackson, J., and Mckenzie, D.P. (1984). Active tectonics of the Alpine-Himalayan belt between western Turkey and Pakistan. *Geophys J Roy Astr S 77*: 185-264.

Jensen, J. (1996). *Introductory digital image processing: a remote sensing prospective* (2nd edition). Prentice-Hall, Englewood Cliffs, New Jersey, 316 p.

Jongsma, D. (1977). Bathymetry and shallow structure of the Pliny and Strabo trenches, south of the Aegean Arc, *Geol. Soc. Am. Bull. 88*: 797-805.

Jutten, C., Herault, J. (1986). Space or time adaptive signal processing by neural network models. *Am. Inst. Phys. Conf. Proc. 151*: 206–211.

Karabacak, V., Altunel, E., Meghraoui, M. and Akyüz, H.S. (2010). Field evidences from northern Dead Sea Fault Zone (South Turkey): New Findings for the Initiation age and Slip Rate. *Tectonophysics, 480*: 172–182.

Karabacak, V., Önderö, Y., Altunel, E., Yalçiner, C.C., Akyüz H.S., and Kiyak, N.G. (2011). Doğu Anadolu Fay Zonunun güney batı uzanımının paleosismolojisi ve ilk kayma hızı. *The aktif tektonik Araştırma Grubu Onbeşinci Çalıştayı Proceceedings (ATAG-15), Ekim*, 19-22, Çukurova Üniversitesi, Karataş-Adana.

Karig, D.E., and Kozlu, H. (1990). Late Paleogene– Neogene evolution of the triple junction region near Maras¸, south-central Turkey. *Journal of the Geological Society, London, 147:* 1023–1034.

Kaymakci, N., Inceöz, M., and Ertepinar, P. (2006). 3D-Architecture and Neogene Evolution of the Malatya Basin: Inferences for the kinematics of the Malatya and Ovacık Fault zones. *Turkish J Earth Sci 15:*123-154.

Keller, E.A., DeVecchio, D.E. (2013). Tectonic geomorphology of active folding and development of transverse drainage. In: Shroder, J, Owen LA, editors. Treatise on Geomorphology. 5th ed. San Diago, CA: Academic Press, pp. 129-147.

Keller, E.A., Pinter, N. (editors) (2002). *Active Tectonics: Earthquakes, Uplift and Landscapes*. 2nd ed. New Jersey, Prentice Hall, 338 pp.

Ketin, İ. (1968). Relations between general tectonic features and the main earthquake regions of Turkey, *Min. Res. Explor. Inst. Bull*. *71*:63-67.

Ketin, İ. (1969). About the North Anatolian Fault, *Min. Res. Explor. lnst. Bull. 72* (1969) 1- 25 (in Turkish with English abstract).

Khalifa, A., Çakir, Z., Owen, L.A., Kaya, Ş. (2017). Evaluation of the relative tectonic activity of the Adiyaman Fault in Eastern Turkey. *Conference abstract, International Symposium on GIS applications in Geography and Geosciences (ISGGG), Çanakkale, Turkey*, October, 18-21, 24, pp. 293.

Khalifa, A., Çakir, Z., Owen, L.A., Kaya, Ş. (2018). Morphotectonic analysis of the East Anatolian Fault, Turkey, *Turkish Journal of Earth Sciences*, *2*:110-126.

Koçyigit, A., (1989). Suşehri basin: an active fault-wedge basin on the North Anatolian Fault Zone, Turkey, *Tectonophysics 167*:13-29.

Koçyigit, A., (1990). Tectonic setting of the Golova basin, the total offset of the North Anatolian Fault Zone, Eastern Pontide, Turkey, *Annates Tecton. 4*: 155- 170.

Kiratzi, A. (1993). A study on the active crustal deformation of the North and East Anatolian Fault Zones. *Tectonophysics 225*: 191-203.

Koçyigit, A., Beyhan, A., (1998). A new intracontinental transcurrent structure: the Central Anatolian Fault Zone, Turkey. *Tectonophysics 284*: 317-336.

Kumar, C., Shetty, A., Raval, S., Sharma, R., and Champati, R. (2015) Lithological discrimination and mapping using ASTER SWIR data in the Udaipur area of Rajasthan, India. *Procedia Earth and Planetary Science,11:* 180–188.

Langbein, W.B. (1947). Topographic characteristics of drainage basins. U.S. *Geological Survey Water-Supply 968 (C)*:125-157.

Lawrence, C., and John, C. (2003). Lithologic mapping in the mountain pass, California area using advanced spaceborne thermal emission and reflection radiometer (ASTER) data. *Remote Sensing of Environment, 84:* 350–366.

Lee, J.B., Woodyatt, A.S., and Berman, M. (1990). Enhancement of high spectral resolution remote sensing data by a noise-adjusted principal components transform. *IEEE Transactions on Geoscience and Remote Sensing, 28:* 295–304.

Lee, T., and Lewicki, M., (2002). Unsupervised image classification, segmentation, andenhancement using ICA mixture models. *Image Proc. 11 (3)*: 270–279.

Le Pichon, X., Angelier, J., (1992). The Aegean arc and trench system: a key to the neotectonic evolution of the eastern Mediterranean area, *Tectonophysics 60*:1-42.

Le Pichon, X., Angelier, J., Aubouin, J., Lyberis, N., Monti, S., Renard, V., Got H., Hsli, K., Marty, Y., Mascle, J., Mathews, D., Mitropoulos, D., Tsotlies, P., Chronis, G. (1979). From subduction to transform motion: a seabeam survey of the Aegean trench system, *Earth Planet. Sci. Lett. 44:* 441-450.

Le Pichon, X., Taymaz, T., Şengör, A.M.C., (1999). *The Marmara Fault and the future İstanbul earthquake,* in: Karaca M., Ural D.N. (Eds.), Proceedings of the International Conference on the Kocaeli Earthquake, 17 August, İstanbul University Press House, İstanbul, pp. 41-54.

Lybéris N., (1988). Tectonic evolution of the Gulf of Suez and the Gulf of Aqaba, *Tectonophysics 153:* 209–220.

Lybéris N., Yürür, T., Chorowicz, J., Kasapoglu, E., Gündoğtu, N. (1992). The East Anatolian fault: an oblique collisional belt, *Tectonophysics 204:*1- 15.

Lifton, N.A., and Chase, C.G. (1992). Tectonic, climatic and lithologic influences on landscape fractal dimension and hypsometry: implications for landscape evolution in the San Gabriel Mountains, California. *Geomorphology, 5:* 77-114.

Luo, G., Chen, G., Tian, L., Qin, k., and Qian, E. (2016). Minimum noise fraction versus principle component analysis as a preprocessing step for hyperspectral imagery denoising. *Canadian Journal of Remte Sensing, 42:* 106–116.

Mahmood, S.A. and Gloaguen, R., (2012). Appraisal of active tectonics in Hindu Kush: Insights from DEM derived geomorphic indices and drainage analysis. *Geoscience Frontiers, 3:* 407-428.

Mahmoud, Y., Masson, F., Meghraoui, M., Cakir, Z., Alchalbi, A., Yavasoglu, H., Yönlü, Ö., Daoud, M., Ergintav, S., Inan, S. (2013). Kinematic study at the junction of the East Anatolian fault and the Dead Sea fault from GPS measurements. *J Geodyn 67:* 30-39.

Marghany, M., and Hashim, M. (2010). Lineament mapping using multispectral remote sensing satellite data. *International Journal of the Physical Sciences, 5:* 1501–507.

Mars, J.C. and Rowan, L.C. (2010). Spectral assessment of new ASTER SWIR surface reflectance data products for spectroscopic mapping of rocks and minerals. *Remote Sensing of Environment, 114:* 2011–

2025.Mayer L (editor) (1990). Introduction to Quantitative Geomorphology: an exercise manual. Englewood, Cliffs, NJ, Prentice Hall.

Man, Y., Woodside J., (1994). Preface: Tectonics of the Eastern Mediterranean, *Tectonophysics, 234:* 1-3.

Mayer, L., (1986). Tectonic geomorphology of scarpments and mountain fronts. *Active Tectonics, 7:* 125-135.

McClusky, S., Balassanian, S., Barka A., et al., (2000). GPS constraints on crustal movements and deformations for plate dynamics. *J. Geophy. Res. 105:* 5695-5720

McKenzie, D.P. (1970). Plate tectonics of the Mediterranean region, *Nature, 220:* 239–343.

McKenzie, D.P. (1972). Active tectonics of the Mediterranean region. *Geophys J Int 30:* 109-85.

McKenzie, D.P. (1976). The East Anatolian fault: a major structure in eastern Turkey. *Earth Planet Sc Lett 29:* 189-193.

McKenzie, D.P. (1978). Active tectonics of the Alpine- Himalayan belt: The Aegean Sea and surrounding regions (tectonic of Aegean region). *Geophys J Roy Astr S 55:* 217-254.

Meghraoui, M., Bertrand, S., Karabacak, V., Ferry, M., Çakir, Z., Altunel, E. (2006). Surface ruptures along the Maras segment of the East Anatolian Fault (SE Turkey) and kinematic modelling from Tectonic and GPS data. *Geophysical Research Abstracts*, EGU, *8*, 10006.

Melosh, B., Keller, E.A. (2013). Effects of active folding and reverse faulting on stream channel evolution, Santa Barbara Fold Belt, California. *Geomorphology 186*: 119-135.

Mercier, J.L. (1981). Extensional--compressional tectonics associated with the Aegean arc: comparison with the Andean Cordillera south of Peru-north Boli via, Philos. *Trans. R. Soc. London Ser. A 300*: 337-355.

Merritts, D., and Vincent, K.R., (1989). Geomorphic response of coastal streams to low, intermediate, and high rates of uplift, Mendocino Triple Junction region, Northern California. *Geol. Soc. Amer. Bull. 110*, 1373 – 1388

Meulenkarnp, J.E., Wonel, W.J.R., Van, Warmel, W.A., Spakman W., Hoogerduyn, Strating, E., (1988). On the Hellenic subduction zone and geodynamic evolution of Crete in the late middle Miocene, *Tectonophysics, 146*: 203-215.

Michael, K, and Frank, L. (2013). Geomorphology of the Tsetseg Nuur basin, Mongolian Altai-lake development, fluvial sedimentation and aeolian transport in a semi-arid environment. *J Maps 9 (3)*: 361-366.

Molin, P., Pazzaglia, F.J., and Dramis, F., (2004). Geomorphic expression of active tectonics in a rapidly-deforming forearc, sila massif, Calabria, southern Italy. *American Journal of Science, 304*: 559-589.

Muehlberger, R.W., and Gordon, M.B. (1987). Observations on the complexity of the East Anatolian Fault, Turkey. *J Struct Geol 9*: 899-903.

Mustard, J.F., and Sunshine, M.J. (1998). Spectral analysis for earth science: investigations using remote sensing data, In: Rencz, A.N. (ed.), Remote Sensing for the Earth Sciences: *Manual for Remote Sensing, 3*, p. 251–306.

Mwaniki, M.W., Moeller, M.S., and Schellmann, G. (2015a). A comparison of Landsat 8 (OLI) and Landsat 7 (ETM+) in mapping geology and visualizing lineaments: A case study of central region Kenya. *International Archives of the Photogrammetry, Remote Sensing and Spatial Information Sciences, 11*: 897–903.

Mwaniki, M.W., Moeller, M.S., and Schellmann, G. (2015b). Application of remote sensing technologies to map the structural geology of central region of Kenya. *IEEE Journal of Selected Topics in Applied Earth Observations and Remote Sensing, 8*: 1855–1867.

Nalbant, S.S., McCloskey, J., Steacy, S. and Barka A.A. (2002), Stress accumulation and increased seismic risk in eastern Turkey. *Earth Planet. Sci. Lett., 195:* 291–298, doi:10.1016/S0012-821X(01)00592-1.

Nascimento, J., and Dias, J. (2005). Does independent component analysis play a role in unmixing hyperspectral data. *Geosci. Remote Sens. 43 (1),* 175–187.

Necea, D., Fielitz, W., and Matenco, L. (2005). Late Pliocene-Quaternary tectonics in the frontal part of the SE Carpathians: insights from tectonic geomorphology. *Tectonophysics, 410*: 137–156.

Nielsen, A.A. (2011). Kernel maximum autocorrelation factor and minimum noise fraction transformations. *IEEE Transactions on Image Processing, 2:* 612–24.

Ninomiya, Y., Fu, B., and Cudahy, T.J. (2005). Detecting lithology with Advanced Spaceborne Thermal Emission and Reflection Radiometer (ASTER) multispectral thermal infrared ''radiance-at-sensor'' data. *Remote Sensing of Environmental, 99:* 127–139.

Nur, A., and Ben-Avraham, Z. (1978). The eastern Mediterranean and the Levant: tectonics of continental collision, Tectonophysics 4678) 297- 311.

Ohmori, H. (1993). Changes in the hypsometric curve through mountain building resulting from concurrent tectonics and denudation. *Geomorphology, 8:* 263–277.

Okada, K., and Ishii, M. (1993). Mineral and lithological mapping using thermal infrared remotely sensed data from ASTER simulator. *International*

Geosciences and Remote Sensing Symposium "Better Understanding of Earth Environment", (Abstract), Tokyo, Japan, August, *93*, p. 126–128.

Okay, A. İ., Demirbağ E., Kurt H., Okay N., and Kuşçu İ. (1999). An active, deep marine strike-slip basin along the North Anatolian Fault in Turkey. *Tectonics, 18*:129-148.

Okay, A.İ., Kashlar-Özcan, A., İmren, C., Boztepe-Güney, A., Demirbağ, E., and Kuşçu, İ. (2000). Active faults and evolving strike-slip basms in the Marmara Sea, northwest Turkey: a multichannel seismic reflection study. *Tectonophysics, 321*:189- 218.

Owen, L.A., Cunningham, W.D., Brian, F.W., Badamgarov, J., Dorjnamjaa, D. (1999). The landscape evolution of Nemegt Uul: a late Cenozoic transpressional uplift in the Gobi Altai, southern Mongolia. *Geol Soc London Spec Publ 162:* 201-218.

Oral, M.B., Reilinger, R.E., Toksöz, M.N., Kong, R.W., Barka, A.A., Kınık, İ., and Lenk, O., (1995) Global positioning system offers evidence of plate motions in eastern Mediterranean, *EOS Transac. 76* (9).

Özkaymak, Ç., and Sözbilir, H. (2012). Tectonic Geomorphology of the Spreader High Ranges, Western Anatolia. *Geomorphology. 173-174*: 128-140.

Papazachos, B.C., and Comninakis, P.E. (1971). Geophysical and tectonic features of the Aegean arc, *J. Geophys. Res. 76*: 8517-8533.

Pérez-Peña, J.V., Azor, A., Azañón, J.M., and Keller, E.A. (2010). Active tectonics in the Sierra Nevada (Betic Cordillera, SE Spain): Insights from geomorphic indexes and drainage pattern analysis. *Geomorphology, 119*: 74-87.

Perinçek, D., and Çemen, İ. (1990). The structural relationship between the East Anatolian and Dead Sea fault zones in Southeastern Turkey, *Tectonophysics, 172*: 331-340.

Pike, R.J., Wilson, S.E. (1971). Elevation-relief ratio, hypsometric integral and geomorphic area-altitude analysis. *Geol Soc Am Bull 82:* 1079-1084.

Rajendran, S., Nasir, S., Kusky, T. M., Ghulam, A., Gabr, S., and El-Ghali, M.A. (2013). Detection of hydrothermal mineralized zones associated with listwaenites in Central Oman using ASTER data. *Ore Geology Reviews, 53:* 470–488.

Ramli, M.F., Yusof, N., Yusoff, M.K., Juahir, H., & Shafri, H. (2010). Lineament mapping and its application in landslide hazard assessment: a review. *Bulletin of Engineering Geology and the Environment, 69*: 215–233.

Reilinger, R., McClusky, S., Oral, M.B., King, W., Toksoz, M., (1997). Global Positioning, System measurements of present-day crustal movement in the Arabian-Africa-Eurasia plate collision zone, *J. Geophy. Res. 102:* 9983- 9999

Reilinger, R., McClusky, S., Vernant, P., Lawrence, S., Ergintav, S., Cakmak, R., Ozener H., Kadirov, F., Guliev, I., Stepanyan, R., et al. (2006). GPS constraints on continental deformation in the Africa-Arabia–Eurasia continental collision zone and implications for dynamics of plate interactions. *J Geophys Res 111*: 1-26.

Rigol-Sanchez, J.P., Chica-Olmo, M., and Abarca-Hernandez, F. (2003) Artificial neural networks as a tool for mineral potential mapping with GIS. *International Journal of Remote Sensing, 24:* 1151–1156.

Rockwell, T.K., Keller E.A., and Johnson, D.L. (1984). *Tectonic geomorphology of alluvial fans and mountain fronts near Ventura*, California. In: Morisawa M, Hack JT editors. Tectonic Geomorphology. The 15th Annual Geomorphology Symposium Proceedings., Boston, MA: Allen and Unwin, pp.183-207.

Robertson, A.H.F., and Grasso, M. (1995). Overview of the late Triassic-Recent tectonic and palaeo-environmental development of the edtterranean region, *Terra Nova 7:*114-127.

Rotstein Y., and Kafka L.A., (1982). Seismotectonics of the southern boundary of Anatolia, eastern Mediterranean region: subduction, collision and arc jumping, *Journal of Geophysical. Research, 87*: 7694–7706.

Rowan, L.C., and Mars, J.C. (2003). Lithologic mapping in the Mountain Pass, California area using Advanced Spaceborne Thermal Emission and Reflection Radiometer (ASTER) data. *Remote Sensing of Environment, 84:* 350–366.

Rowan, L., Hook, S.J., Abrams, M.J., and Mars, J.C. (2003). Mapping hydrothermally altered rocks at Cuprite, Nevada, using the Advanced Spaceborne thermal emission and reflection radiometer (ASTER), a new satellite-imaging system. *Economic Geology, 98 (5):* 1019–1027.

Sabine, C. (1999). *Remote sensing strategies for mineral exploration*, In: Rencz, A.N. (ed.), Remote Sensing for the Earth Sciences, Manual of Remote Sensing, 3, p. 375–447.

Sabins, F. (1997). *Remote Sensing Principles and Interpretation* (3th edition). Freeman, New York, 494 p.

Salamon, A., Hofstetter A., Garfunkel Z., .Ron H., (1996). Seismicity in the eastern Mediterranean region: perspective from the Sinai subplate, *Tectonophysics 263*: 293-305.

Schumm, S.A., Dumont, J.F., and Holbrook, J.M. (2002). *Active Tectonics and Alluvial Rivers*. Cambridge, Cambridge University Press, 292pp.

Selby, M.J. (1980). A rock strength classification for geomorphic purposes: with tests from Antarctica and New Zealand. *Z. Geomorphology, 24*: 31-51.

Selçuk, A.S. (2016). Evaluation of the relative tectonic activity in the eastern Lake Van basin, East Turkey. *Geomorphology, 270*: 9-21.

Selim, H.H., Tüysüz, O., Karakaş, A., Taş, and K.Ö. (2013). Morphotectonic evidence from the southern branch of the North Anatolian Fault (NAF) and basins of the south Marmara Sub-region, NW Turkey. *Quaternary International, 292*: 176-192.

Seymen, I., and Aydin, A. (1972). The Bingöl earthquake fault and its relation to the North Anatolian Fault Zone. *General Directorate of Mineral Research and Exploration (MTA) Bulletin 79*: 1-8 (in Turkish with English abstract).

Silva, P.G., Goy, J.L., Zazo, C., Bardaji, T. (2003). Fault-generated mountain fronts in southeast Spain: geomorphologic assessment of tectonic and seismic activity. *Geomorphology 50*: 203-225.

Smith, A.G. (1971) Alpine deformation and the oceanic areas of the Tethys, Mediterranean and Atlantic, *Geol. Soc. Am. Bull. 82*: 2039-2070

Steckler M.S., Berthelot F., Lybéris N., and Le Pichon X. (1988). Subsidence in the Gulf of Suez: implications for rifting and plate kinematics, *Tectonophysics 153*: 249–270.

Steinz G. and Bartov Y. (1991). The Miocene-Pliocene history of the Dead Sea segment of the Rift in the light of K–Ar ages of basalts, *Israel Journal of Earth Science, 40:* 199–208.

Strahler, A.N. (1952). Hypsometric (area-altitude curve) analysis of erosional topography. *Geol Soc Am Bull 63*: 1117-1141.

Straub, C., Kahle, H.G. (1995) Active crustal deformation in the Marmara Sea region, NW Anatolia, inferred from GPS measurements, *Geophys. Res. Lett. 22:* 2533-2536.

Straub, C., Kahle, H.G., and Schinder, C. (1997). GPS and geologic estimates of the tectonic activity in the Marmara region, NW Anatolia, *J. Geophys. Res. 102:* 27587-27601.

Şaroğlu, F. (1988) The age and offset on the North Anatolian Fault, METU J. Pure *Appl. Sci. 21*: 65- 79.

Şaroğlu, F., Emre, Ö., and Boray, A. (1987). Turkiye'nin Diri Fayları ve DepremsellikJeri. Min. Res. Expl. Inst. Turkey Report No. 8174, 87 (in Turkish).

Şaroğlu, F., Emre, Ö., and Kuşçu, I. (1992a). Active fault map of Turkey. *General Directorate of Mineral and Research Exploration of Turkey Publication (MTA)*, Ankara, Turkey.

Şaroğlu, F., Emre, Ö., Kuşçu, I. (1992b). The East Anatolian fault zone of Turkey. *Annals Tectonics, 6*: 99-125.

Şengör, A.M.C. (1979). The North Anatolian Transform Fault: its age, offset and tectonic significance. *Geol Soc London Spec Publ., 136*: 269-82.

Şengör, A.M.C. and Yilmaz, Y. (1981). Tethyan evolution of Turkey: a plate tectonic approach, *Tectonophysics, 75*: 181 -241.

Şengör, A.M.C., Görür, N., and Şaroğlu, F. (1985). Strike-slip faulting and related basin formation in zones of tectonic escape: Turkey as a case study. In: Biddle KT, Christie-Blick N editors. Strike-slip deformation, basin formation and sedimentation. *Soc Econ Pa., 37*: 227-264.

Şengör, A.M.C., Grall, C., Imren, C., Le Pichon, X., Görür, N., Henery, P., Karabulut, H., Siyako, S. (2014). The geometry of the North Anatolian transform fault in the Sea of Marmara and its temporal evolution: implications for the development of intracontinental transform faults. *Can J Earth Sci., 51*: 222-242.

Tari, U., and Tüysüz, O. (2015). The effects of the North Anatolian Fault on the geomorphology in the Eastern Marmara Region, Northwestern Turkey. *Geodin Acta : 28 (3)*: 139-159.

Taymaz, T., Eyidoğan, H., and Jackson, J. (1991). Source parameters of large earthquakes in the East Anatolian Fault Zone (Turkey). *Geophys J Int 106:* 537-50.

Tepe, Ç., Sözbilir, H. (2017). Tectonic geomorphology of the Kemalpaşa Basin and surrounding horsts, southwestern part of the Gediz Graben, Western Anatolia, *Geodin Acta 29 (1):* 70-90.

Toksöz, M.N., Guenette, M., Gülen, L., Keough, G., Pulli, J.J., Sav, H., and Olguner, A., (1983). Source mechanism of Narman-Horasan earthquake, *Yeryuvan ve insan 8*, 47- 52 (in Turkish with English abstract).

Toksöz, M.N., Reilinger, R.E., Doll, C.G., Barka, A.A., Yalçın, N. (1999). İzmit (Turkey) earthquake of 17 August 1999: first report, *Seismol. Res. Lett. 70:* 669-679.

Topal, S., Keller, E., Bufe, A., Kocyiğit, A. (2016). Tectonic geomorphology of a large normal fault: Akşehir fault, SW Turkey. *Geomorphology, 259*: 55-69.

Tsodoulos, I.M., Koukouvelas, I.K., and Pavlides, S. (2008). Tectonic geomorphology of the easternmost extension of the Gulf of Corinth (Beotia, Central Greece). *Tectonophysics, 453:* 211-232.

Tüysüz, O., Barka, A.A., and Yiğitbaş E. (1998). Geology of the Saros Graben: its implications on the evolution of the North Anatolian Fault in the Ganos-Saros region, NW Turkey, *Tectonophysics, 29*: 105-126.

Ul-Hadi, S, Shuhab, D.K., Owen, L.A., and Khan, A.S. (2013). Geomorphic response to an active transpressive regime: a case study along the Chaman strike-slip fault, western Pakistan. *Earth Surf Proc Land 38*: 250-264.

Velosky, J.C., Stern, R.J., and Johnson, P.R. (2003). Geological control of massive sulfide mineralization in the Neoproterozoic Wadi Bidah

shear zone, southwestern Saudi Arabia, inferences from orbital remote sensing and field studies. *Precambrian Research, 123*: 235–247.

Vidal, N., Alvarez-Marrón J., Klaeschen D., (2000). The structure of e Africa-Anatolia plate boundary in the eastern Mediterranean, *Tectonics 19:* 723-739.

Wells, S.G., Bullard, T.F., Menges, T.M., Dark, P.G., Keras, P.A., Kelson, K.I., Ritter, J.B., wesling, J. B., Wesling, J. R., (1988). Regional variations in tectonic geomorphology along segmented convergent plate boundary, Pacific coast of Costa Rica. *Geomorphology, 1:* 239-265.

Westaway, R. (1994). Present-day kinematics of the Middle East and eastern Mediterranean. *J Geophys Res 99:* 12071-12090.

Westaway, R. 2003. Kinematics of the Middle East and Eastern Mediterranean updated. *Turkish Journal of Earth Sciences, 12*: 5–46.

Westaway, R. 2004. Kinematic consistency between the Dead Sea Fault Zone and the Neogene and Quaternary left-lateral faulting in SE Turkey. *Tectonophysics, 391:* 203–237.

Westaway, R., and Arger, J. (1996). The Gölbaşı basin, southeastern Turkey: a complex discontinuity in a major strike-slip fault zone. *Geol Soc London Spec Publ., 153:* 729-743.

Westaway, R., and Arger, J. (2001). Kinematics of the Malatya-Ovacık Fault Zone. *Geodin Acta 14:* 103-131.

Westaway, R., Demir, T., Seyrek, A., and Beck, A. (2006). Kinematics of active left-lateral faulting in SE Turkey from offset Pleistocene river gorges: improved constraint on the rate and history of relative motion between the Turkish and Arabian plates. *Geol Soc London Spec Publ 163*: 149-164.

Willgoose, G. (1994). A physical explanation for an observed area– slope–elevation relationship for catchments with declining relief. *Water Resources Research, 30:* 151-159.

Willgoose, G. and Hancock, G. (1998). Revisiting the hypsometric curve as an indicator of form and process in transport-limited catchment. *Earth Surface Processes and Landforms, 23:* 611-623.

Wong, H.K., Ludmann, T., Uluğ, T.A., and Görür, N. (1995). The Sea of Marmara: a plate boundary sea in an escape tectonic regime, *Tectonophysics 244:* 231 - 250.

Woodside, J.M. (1977) Tectonic elements and crust of the eastern e Iterranean Sea, *J. Geophys. Res. 99:* 12071-12090.

Yalçın, M.N. (1979). Dogu Anadolu yarılımının Türkoğlu-Karaağaç (k. Maraş) arasındaki kesiminin özellikleri ve bölgedeki yerleşim alanları. Türkiye Jeologi kurumu Altınlı Simpozyumu, Özel Sayı: 49-55.

Yaltırak, C., Alpar, B., Sakınç, M., and Yüce, H. (2000). Origin of the strait of Çanakkale (Dardanelles): regional tectonics and the Mediterranean-Marmara incursion, *Marine Geol., 16*: 139-156.

Yamaguchi, Y., and Naito, C., (2003). Spectral indices for lithologic discrimination and mapping by using the ASTER SWIR bands. *International Journal of Remote Sensing, 24 (22):* 4311–4323

Yamaguchi, Y., Kahle, A.B., Kawakami, T., and Paniel, M., (1998). Overview of the advanced spaceborne thermal emission and reflection radiometer (ASTER). *IEEE Transaction on Geoscience and Remote Sensing, 36 (4):* 1062–1071.

Yang, J., Cheng Q., (2015). A comparative study of independent component analysis with principal component analysis in geological objects identification, Part I: Simulations, *Journal of Geochemical Exploration, 149*: 127–135.

Yiltırak, C. (1996). Tectonic history of the Ganos fault System, *Turkish Assoc. Petrol. Geol. Bull. 8:* 137- 156 (in Turkish with English abstract).

Yiltırak, C., Sakıç, M., Oktay, F.Y. (2000). Kinematics and evolution of the northern segment of the North Anatolian Fault Zone (Gabos Fault) in the area between Marmara and Gulf of Saroz, in: Tatar O., Kavak K.S., Özden S. (Eds.), *Tektonik Araştırma Grubu 3*. Toplantısı, ATAG-3 Proceedings, Pp. 77-89 (in Turkish with English abstract).

Yıldırım, C. (2014). Relative tectonic activity assessment of the Tuz Gölü Fault Zone; Central Anatolia, Turkey. *Tectonophysics, 630*: 183-192.

Yönlü, Ö., Altunel, E., Karabacak, V., and Akyüz, H.S. (2013). Evolution of the Gölbaşı basin and its implications for the long-term offset on the East Anatolian Fault Zone, Turkey. *J Geodyn 65*: 272-281.

Yönlü, Ö., Altunel, E., Karabacak, V. (2017). Geological and geomorphological evidence for the southwestern extension of the East Anatolian Fault Zone, Turkey. *Earth Planet Sc Lett 469*:1-14.

Yönlü, Ö., Karabacak, V., Altunel, E., and Akyüz, H.S. (2012). Paleoseismological slip rate on the East Anatolian fault zone around Türkoğlu. Conference abstract, *International Earth Science Colloquium on the Aegean Region* (IESCA), Izmir, Turkey, October, 1-5, pp. 104.

Yürür, M.T., and Chorowicz, J. (1998). Recent volcanism, tectonics and plate kinematics near the junction of the African, Arabian and Anatolian plates in the Eastern Mediterranean. *J. Volcanol Geotherm Res 85*: 1-15.

Zhang, T., Yi, G., Li, H., Wang, Z., Tang, J., Zhong, K., Li, Y., Wang, Q., and Bie, X. (2016). Integrating Data of ASTER and Landsat-8 OLI (AO) for Hydrothermal Alteration Mineral Mapping in Duolong Porphyry

Cu-Au Deposit, Tibetan Plateau, China. *Remote sensing, 8 (890)*: 1–23.

CURRICULUM VITAE

Name Surname	: Abdelrahman KHALIFA
Place and Date of Birth	: Egypt, Cairo, 02/13/1981
E-Mail	: akhalifa@itu.edu.tr

EDUCATION :

- **B.Sc.** : 2003, Al-Azhar University, Faculty of Science, Department of Geology.
- **M.Sc. (If exists)** : 2009, Al-Azhar University, Faculty of Science, Department of Geology.

PROFESSIONAL EXPERIENCE AND REWARDS:

- 2004-2005: Geologist at Australian Centamine Company for gold exploration, Gabal Al-Sukari, Marsa Alam, Eastern Desert, Egypt.
- 2006-2009: Demonstrator, Department of Geology, Faculty of Science, Al-Azhar University.
- 2009-currently: Teaching Assistant, Department of Geology, Faculty of Science, Al-Azhar University.
- December 2014- December 2015: Visiting student at Department of Geology, University of Cincinnati, Cincinnati, OH 45221, USA.

PUBLICATIONS, PRESENTATIONS AND PATENTS ON THE THESIS:

- **Khalifa, A.,** Ziyadin Çakır, Lewis A. Owen, Şinasi Kaya, **2018:** Morphotectonic analysis of the East Anatolian Fault (Turkey). *Turkish Journal of Earth Sciences,2:*110-126*.*

- **Khalifa, A.,** Ziyadin Çakır, Lewis A. Owen, Şinasi Kaya, **2018:** Evaluation of the relative tectonic activity of the Adıyaman Fault within the Arabian-Anatolian plate boundary (Eastern Turkey)**.** *Geologica Acta.*In press.

- **Khalifa, A.,** Çakir, Z., Owen, L.A., Kaya, Ş., **2017**: Evaluation of the relative tectonic activity of the Adiyaman Fault in Eastern Turkey. Conference abstract, International Symposium on GIS applications in Geography and Geosciences (ISGGG), Çanakkale, Turkey, October, 18-21, 24, pp. 293.

- **Khalifa, A.,** *Çakir, Z., Owen, L.A., Kaya, Ş.,* **2016:** Relative tectonic activity assessment along the East Anatolian strike-slip fault, Eastern Turkey, Poster presentation, EGU General assembly, V: *2*, 2333.